CHAPTER 3

In-Plane Microwave Response of High-T_c Single Crystals: Experiment and Theory

M.R. Trunin and A.A. Golubov

We present an overview of measurements of the surface impedance $Z_s(T) = R_s(T) + iX_s(T)$ and complex conductivity $\sigma_s(T) = \sigma_1(T) - i\sigma_2(T)$ in the ab-plane of high-quality high-T_c single crystals YBCO, BSCCO, TBCCO, and TBCO and their theoretical interpretation. Electrodynamic principles of the experimental 'hot finger' technique, most frequently used in high-precision measurements of the surface impedance, are analyzed. A systematic description of the results of measurements obtained by means of this technique are presented. The conventional theory of the local electrodynamics of superconductors is discussed, and it is argued that traditional models do not describe adequately the microwave response of high-T_c superconductors. The comparison is performed of experimental curves of the surface impedance and complex conductivity to calculations based on the modified two-fluid model, which includes quasiparticle scattering and characteristic change in the density of superconducting carriers as a function of temperature. Further, the existing microscopic models are reviewed, which are based on unconventional symmetry types of the order parameter and on novel mechanisms of quasiparticle relaxation. The relevance of these models to the experimental data is discussed. The prospects for further research of the high-frequency response of high-temperature superconductors are outlined.

3.1 INTRODUCTION

Measurements of the surface impedance of high-T_c superconductors (HTS) as a function of temperature, $Z_s(T) = R_s(T) + iX_s(T)$, yield information about the nature of quasiparticles in the superconducting state, their scattering, density of states, and, if a more sophisticated analysis is undertaken, about the superconducting pairing mechanism in these materials.

In this review we will consider measurements of stoichiometrically perfect single crystals of $YBa_2Cu_3O_{6.95}$ (YBCO), $Bi_2Sr_2CaCu_2O_8$ (BSCCO), $Tl_2Ba_2CaCu_2O_{8-\delta}$ (TBCCO), and $Tl_2Ba_2CuO_{6+\delta}$ (TBCO) whose doping level corresponds to the highest critical temperature T_c, the superconducting transition width ΔT derived from the measurements of $R_s(T)$ is small, $\Delta T \lesssim 1$ K, and the residual surface

resistance in the ab-plane $R_{\rm res} \equiv R_s(T \to 0)$ at frequency of ~ 10 GHz is less than one milliohm. There is good reason to suppose that electrodynamic parameters of these samples adequately characterize intrinsic microscopic properties of superconductors. We will review available phenomenological and microscopic models of the high frequency response of HTS and discuss the existing achievements as well as difficulties in explanation of common and distinctive features of the data. As a whole the experimental and theoretical investigation of electromagnetic response of HTS should permit the determination of the dominant mechanism for electronic relaxation in the normal state and its interrelation with superconducting pairing of HTS, provide information on the order parameter symmetry, and elucidate the role of defects in these materials.

There are several common features of the microwave response in the ab-plane of HTS crystals. First, high-precision measurements of the in-plane penetration depth $\lambda_{ab}(T) \propto X_s(T)$ of YBCO single crystals at microwave frequencies revealed a linear temperature dependence [78, 7, 216, 32, 104, 134, 98, 180, 193, 185, 217, 186, 195, 103, 91] for temperatures below 25 K. Such linear variation of $\lambda(T)$ at low T has by now been observed not only in orthorhombic YBCO single crystals and films [203, 84, 55, 43], but also in tetragonal BSCCO [180, 97, 179, 122, 175], TBCO [35, 209], and TBCCO [217] single crystals. This temperature dependence is incompatible with a nearly isotropic gap of superconductor and it is now considered to provide strong evidence for d-wave pairing in these materials [145, 147, 148, 23, 87, 36, 212, 88, 89, 172, 17, 132], even though the quantity measured is not sensitive to the phase of the superconducting order parameter. Later research has shown that $\Delta\lambda_{ab}(T)$ could be linear at low T for the models invoking the proximity effect between normal and superconducting layers [115] or assuming anisotropic s-wave pairing [119, 69, 9]. However, none of these theories can explain substantially different slopes of the $\Delta\lambda_{ab}(T)$ curves in YBCO samples grown by different methods [196] or features (a bump [185, 186, 84, 112] or plateau [193, 217, 195]) observed in the intermediate temperature range $0.3T_c < T < 0.8T_c$. Models containing a mixed $(d+s)$-symmetry of the order parameter [123, 53, 114, 28, 41, 46, 108, 24, 160, 150, 168, 178, 127, 156, 25, 174, 149, 49, 152] hold some promise for a successful description of these experimental features, but checking this requires additional theoretical investigations.

Another common feature of the electromagnetic response of HTS crystals is the linear variation with temperature of the surface resistance $R_s(T)$ in the ab-plane at low temperatures. At frequencies below 30 GHz the T-dependence of $R_s(T)$ in BSCCO, TBCO, and TBCCO single crystals is linear in the range $0 < T \lesssim T_c/2$ [180, 97, 179, 122, 175, 35, 196]. For YBCO crystals $\Delta R_s(T) \propto T$ for $T \lesssim T_c/4$ and $R_s(T)$ displays a broad peak at higher temperatures [32, 104, 134, 98, 180, 193, 185, 217, 186, 195, 103, 91, 30, 182, 33, 110, 190]. This peak can be understood in terms of a competition between an increase in the quasiparticle lifetime and a decrease in the quasiparticle density. The fairly slow decrease in the quasiparticle density is indicative of a highly anisotropic or unconventional order parameter resulting in a very small or vanishing energy gap, whereas the increase in the quasiparticle lifetime must be attributed to the presence of inelastic scattering, which can be (i)

due to the exchange of antiferromagnetic spin fluctuations, which would naturally lead to d-wave pairing [145, 147, 148], (ii) due to strong electron-phonon interaction with a pronounced momentum dependence, which should lead to an anisotropic s-wave pairing when the repulsive Coulomb interaction is sufficiently small [29]. Moreover, there have been suggestions of some unconventional states for the charge carriers in the CuO planes like the marginal Fermi liquid [200, 1] and the Luttinger liquid [12]. However, to fit the data on YBCO, the inelastic scattering rate has to drop with temperature much faster than any of these microscopic models would predict. Further, the d-wave model with point scatterers does predict a finite low temperature and low frequency limit, which is independent of the concentration and the strength of the scattering centers. So, this model does not explain the sample dependence of the residual surface resistance $R_{\rm res}$ and the value of this universal surface resistance is much lower than the values deduced from experiments. There is no microscopic theory explaining the linear temperature dependence of $\Delta R_s(T)$ up to $T_c/2$ in the crystals with non-orthorhombic structure and the shoulder of $R_s(T)$ at $T > 40$ K in YBCO [185, 186]. Only in high quality YBCO films and single crystals does a d-wave theory come close to the experimental results obtained at a certain finite frequency, when the scattering phase shift is used as fitting parameter [84].

In the absence of a microscopic theory, a modified two-fluid model has been suggested [194, 56] which adequately describes the temperature dependence of $Z_s(T)$ for different HTS single crystals. The success of the two-fluid model could be taken as an indication that the order parameter is indeed highly anisotropic, so that there are no contributions to the response function from the density of states that would diverge in the zero frequency limit.

The elucidation of the issues stated above including establishment of the basic carrier scattering mechanisms and order parameter symmetry, as well as modification of these properties through various types of defects and/or oxygen deficiency, requires substantial extensions of the existing theoretical framework with a view to describing the electromagnetic response of high temperature superconductors. If successful, it would represent a significant step towards understanding the nature of high temperature superconductivity and will assist in future applications of HTS in high-frequency electronics.

The structure of this review is as follows. The next section describes the conventional theory of the electrodynamics of superconductors. Section 3.3 is dedicated to the analysis of measurements that can be performed using the 'hot finger' technique and its limitations, since this method is used in high-precision measurements of the HTS surface impedance versus temperature in the microwave band more frequently than others. Section 3.4 describes systematized measurements obtained by means of this technique. Section 3.5 compares experimental curves of $Z_s(T)$ and $\sigma_s(T)$ to calculations based on the modified two-fluid model. In Section 3.6 we will discuss microscopic models that have been developed to this day and are based on possible symmetry types of the order parameter and mechanisms of quasiparticle relaxation. The concluding section describes prospects of further research in the microwave response of HTS single crystals.

3.2 ELECTRODYNAMICS OF SUPERCONDUCTORS

3.2.1 Phenomenological Theory

In order to define the electromagnetic properties of a superconductor, the electrodynamic relations describing magnetic field distribution inside a superconductor should be derived. Such relations are quite different from those in normal metals. Prior to their derivation from microscopic Bardeen–Cooper–Schrieffer (BCS) theory [22] the electrodynamics of superconductors were quite successfully described phenomenologically, first in the framework of London theory [130] and then on the basis of the more general Ginzburg–Landau theory [64]. Both theories operate with phenomenological parameters which can be estimated from experiment, even without specifying a microscopic mechanism of superconductivity. This gives an acceptable description of many practical situations. It is important that the relation between these phenomenological theories and the BCS microscopic theory was established recently, which allowed us to express the parameters of the phenomenological theories through material constants of real superconductors. Below we start from the London theory.

3.2.1.1 Equations of Two-Fluid Electrodynamics

The basic assumption first made by Gorter and Casimir (GC) [73] is that the system exhibiting superconductivity possesses an ordered (condensed) state, the total energy of which is characterized by an order parameter. This parameter varies from zero at $T = T_c$ to unity at $T = 0$ K, and thus indicates the fraction of the total system which is in the condensed state. Another part of the system is in a noncondensed state, and its behavior is taken to be similar to that of the equivalent nonsuperconducting system. This description is called the *two-fluid model*: all current carriers are divided into two subsystems, into the superconducting current carriers of density n_s (the superfluid), and into the normal current carriers of density n_n (the normal fluid).

The total current $\boldsymbol{J}$ is the sum of a normal current $\boldsymbol{J}_n$ and a supercurrent $\boldsymbol{J}_s$

$$\boldsymbol{J} = \boldsymbol{J}_n + \boldsymbol{J}_s \equiv \sigma_n \boldsymbol{E} + \boldsymbol{J}_s, \tag{3.1}$$

where $\boldsymbol{E}$ is an electric field and σ_n is a conductivity associated with normal electrons.

Within the London model, the set of Maxwell's equations in a quasi static case

$$\text{curl}\, \boldsymbol{H} = \sigma_n \boldsymbol{E} + \boldsymbol{J}_s, \quad \text{curl}\, \boldsymbol{E} = -\mu_0 \frac{\partial \boldsymbol{H}}{\partial t} \tag{3.2}$$

($\mu_0 = 4\pi \times 10^{-7}$ H/m) should be completed by the equation of motion of superconducting electrons with the charge e and effective mass m (the first London's equation)

$$\boldsymbol{E} = \frac{m}{n_s e^2} \frac{\partial \boldsymbol{J}_s}{\partial t} \equiv \mu_0 \lambda_L^2 \frac{\partial \boldsymbol{J}_s}{\partial t}, \tag{3.3}$$

which is equivalent to

$$\boldsymbol{J}_s = -\frac{\boldsymbol{A}}{\lambda_L^2}, \tag{3.4}$$

where $\boldsymbol{A}$ is vector potential (curl $\boldsymbol{A} = \boldsymbol{H}$) and λ_L is the London penetration depth

$$\lambda_L = \sqrt{\frac{m}{\mu_0 n_s e^2}}. \tag{3.5}$$

From (3.2) and (3.3) one can easily obtain the second London's equation

$$\Delta \boldsymbol{H} - \frac{\boldsymbol{H}}{\lambda_L^2} = 0. \tag{3.6}$$

According to (3.4), the London description is local, which means that the field is constant over a coherence length ξ_0 dictating the scale of electron pair correction. The local case holds when $\lambda_L \gg \xi_0 = \hbar v_{\mathrm{F}}/\pi\Delta(0)$, where v_{F} is the Fermi velocity and $\Delta(0)$ is the isotropic superconducting gap at $T = 0$. In the opposite regime, $\xi_0 \gg \lambda_L$, the scale of the vector potential variation λ_L is smaller than the coherence volume given by ξ_0, and therefore the local description does not hold. In the presence of impurity scattering the coherence length $\xi(l)$ is assumed to be $1/\xi(l) = 1/\xi_0 + 1/l$ [159], where l is the average mean free path of electrons in the normal state. According to Abrikosov's concept [2], superconductors are classified as pure ($l > \xi_0$) and dirty ($l < \xi_0$) on one hand, and London ($\xi \ll \lambda$) and Pippard ($\xi \gg \lambda$) on the other. As $T \to 0$, $\xi = \xi_0 \ll \lambda = \lambda_L$ in pure London superconductors and $\xi(l) \sim (\xi_0 l)^{1/2} \ll \lambda(l) \sim \lambda_L(\xi_0/l)^{1/2}$ in dirty superconductors. In pure Pippard superconductors $\xi = \xi_0 \gg \lambda \sim \lambda_L(\xi_0/\lambda_L)^{1/3}$, and in dirty superconductors $\xi(l) \gg \lambda(l)$. The relationship between the current and magnetic field in London superconductors is local (the London limit), whereas in Pippard superconductors this relation is essentially nonlocal (the Pippard limit). In accordance with these concepts, high-T_c materials should be classified as London superconductors, pure rather than dirty. In the case when an energy gap is an anisotropic function of the electron quasimomentum, $\Delta(\boldsymbol{p})$, and has a line node on the Fermi surface of a pure superconductor, $\xi(\boldsymbol{p}) > \lambda_L$ in a narrow region about this line in the quasimomentum space. The contribution of this region to the microwave response of the superconductor should be expressed in terms of nonlocal electrodynamics, but theoretical estimates [118] indicate that nonlocal effects in this region are essential only at very low temperatures $T < 3$ K. Therefore we shall not take these corrections into account in the following discussion.

From the London's equations one can derive the distributions of fields and currents in a superconducting specimen under various conditions. The static distribution of a magnetic field and current within a superconductor of an arbitrary shape can be found, as well as the response of a superconductor to an external high-frequency electromagnetic field.

3.2.1.2 Complex Conductivity in the Gorter–Casimir Two-Fluid Model

In the framework of London theory the response of a superconductor to an external electromagnetic field is fully determined by the equations (3.1–3.6) in which a conductivity associated with normal electrons, σ_n, is introduced phenomenologically in order to account for the behavior of the normally conducting electron fluid. The superconductor's response to a weak alternating electromagnetic field of frequency ω, $\boldsymbol{E}\mathrm{e}^{i\omega t}$, is then given by

$$\boldsymbol{J} = \boldsymbol{J}_n + \boldsymbol{J}_s = \sigma_s \boldsymbol{E} = (\sigma_1 - i\sigma_2)\boldsymbol{E}. \tag{3.7}$$

In accordance with GC model [73], at all temperatures $T \leq T_c$ the total carrier concentration is $n = n_s + n_n$, where $n_{s,n}$ are the fractions of superconducting and normal carrier densities (both have the same charge e and effective mass m). The equation of motion for the superconducting carriers is London's first equation (3.3). The normal current carriers are affected by alternating electric field and the averaged 'force of friction' containing the relaxation time τ of normal carriers, the motion of normal carriers being described by Newton's second law. By solving the equations of motion, we obtain expressions for the components of complex conductivity $\sigma_s = \sigma_1 - i\sigma_2$:

$$\sigma_1 = \frac{n_n e^2 \tau}{m}\left[\frac{1}{1+(\omega\tau)^2}\right], \quad \sigma_2 = \frac{n_s e^2}{m\omega} + \frac{n_n e^2}{m\omega}\left[\frac{(\omega\tau)^2}{1+(\omega\tau)^2}\right]. \tag{3.8}$$

The complex conductivity σ_s is a basic property of a superconductor. The real part of conductivity σ_1 is determined purely by the normal component whereas both the components, normal and superconducting, contribute to the imaginary part σ_2.

For sufficiently low frequencies $(\omega\tau)^2 \ll 1$ and temperatures not too close to T_c the expressions for the conductivity components in (3.8) transform to a very simple form:

$$\sigma_1 = \frac{e^2\tau}{m} n_n, \quad \sigma_2 = \frac{e^2}{m\omega} n_s = \frac{1}{\mu_0 \omega \lambda_L^2}. \tag{3.9}$$

Penetration of alternating field in a superconductor is then given by frequency-dependent skin depth. Based on the result for the complex conductivity, one can obtain the skin depth δ_s by the generalization of the corresponding expression for a normal conductor

$$\delta_s = \frac{\sqrt{2}\lambda_L}{\sqrt{\omega\tau(n_n/n_s) - i}}. \tag{3.10}$$

With the increase of frequency ω the skin depth δ_s decreases, and therefore the London penetration depth of a static field, λ_L, gives the upper bound for the penetration of electromagnetic field into a superconductor.

3.2.1.3 Surface Impedance

A dissipationless current can flow through a superconductor only in a static case, whereas at finite frequencies energy dissipation is present. Losses in a metallic sample are generally characterized by the surface impedance [120] which is given in the local regime by the simple formula

$$Z_s = R_s + iX_s = \left(\frac{i\omega\mu_0}{\sigma_1 - i\sigma_2}\right)^{1/2}. \tag{3.11}$$

The impedance components in terms of the conductivity components

$$R_s = \sqrt{\frac{\omega\mu_0(\varphi^{1/2}-1)}{2\sigma_2\varphi}}, \tag{3.12}$$

$$X_s = \sqrt{\frac{\omega\mu_0(\varphi^{1/2}+1)}{2\sigma_2\varphi}}, \tag{3.13}$$

where $\varphi = 1 + (\sigma_1/\sigma_2)^2$. It is obvious that $R_s < X_s$ at $T < T_c$.

The components of the surface impedance are measurable quantities. The real part of the surface impedance, i.e., the surface resistance R_s, is proportional to the loss of the microwave power and caused by the presence of normal carriers. The imaginary part of the surface impedance, i.e., the reactance X_s, is largely determined by the response of superconducting carriers and characterizes the nondissipating energy stored in the superconductor surface layer.

Equations (3.11–3.13) allow us to express the real and imaginary parts of the conductivity in terms of R_s and X_s:

$$\sigma_1 = \frac{2\omega\mu_0 R_s X_s}{(R_s^2 + X_s^2)^2}, \quad \sigma_2 = \frac{\omega\mu_0(X_s^2 - R_s^2)}{(R_s^2 + X_s^2)^2}. \tag{3.14}$$

Above the superconducting transition temperature, the mean free path l of current carriers is shorter than the skin depth δ_n in the normal state (at $T \geq T_c$), $l \ll \delta_n$, which corresponds to the conditions of the normal skin effect. Equations (3.11–3.14) also apply to the normal state of HTS, when $R_n(T) = X_n(T) = \sqrt{\omega\mu_0/2\sigma_n(T)}$ and $\sigma_n \equiv \sigma_1(T \geq T_c)$, $\sigma_2 \approx 0$.

It is straightforward to get the analogues of (3.11–3.14) for normalized quantities, relating the real and imaginary parts of the impedance to the components of complex conductivity and vice versa:

$$\frac{R_s(T)}{R_s(T_c)} = \sqrt{\frac{\sigma(T_c)(\varphi^{1/2}-1)}{\sigma_2\varphi}}, \frac{X_s(T)}{X_s(T_c)} = \sqrt{\frac{\sigma(T_c)(\varphi^{1/2}+1)}{\sigma_2\varphi}}, \tag{3.15}$$

$$\frac{\sigma_1(T)}{\sigma(T_c)} = \frac{4R_s^2(T_c)R_sX_s}{(R_s^2+X_s^2)^2}, \qquad \frac{\sigma_2(T)}{\sigma_2(0)} = \frac{\lambda^2(0)}{\lambda^2(T)} = \frac{X_s^2(0)(X_s^2-R_s^2)}{(R_s^2+X_s^2)^2}. \tag{3.16}$$

Here $R_s(T_c) = X_s(T_c)$ and $\sigma(T_c) = \sigma_1(T_c)$ are the impedance and conductivity at $T = T_c$, $X_s(0)$ and $\sigma_2(0)$ are the values at $T = 0$, and $\lambda = \sqrt{1/\omega\mu_0\sigma_2}$.

With a decrease of temperature $T < T_c$, when $\sigma_1 \ll \sigma_2$, according to (3.12) and (3.13)

$$R_s \approx \frac{(\omega\mu_0)^{1/2}\sigma_1}{2\sigma_2^{3/2}} = \frac{1}{2}\omega^2\mu_0^2\sigma_1\lambda^3, \quad X_s \approx (\omega\mu_0/\sigma_2)^{1/2} = \omega\mu_0\lambda. \tag{3.17}$$

In the opposite limiting case ($\sigma_1 \gg \sigma_2$) in close proximity to the transition temperature T_c, we have $\sigma_1 \to \sigma(T_c)$ and $\sigma_2 \to 0$, and the quantities

$$R_s \approx \sqrt{\frac{\omega\mu_0}{2\sigma_1}}\left(1 - \frac{\sigma_2}{2\sigma_1}\right), \quad X_s \approx \sqrt{\frac{\omega\mu_0}{2\sigma_1}}\left(1 + \frac{\sigma_2}{2\sigma_1}\right) \tag{3.18}$$

become equal at $T = T_c$.

3.2.1.4 *Temperature Dependences of $Z_s(T)$ and $\sigma_s(T)$ in the Gorter–Casimir Model*

An analysis of the temperature dependences $Z_s(T)$ and $\sigma_s(T)$ allows one to check whether a theoretical model provides an adequate description of the electromagnetic properties of a superconductor.

The temperature dependences of various physical quantities below T_c are introduced in the GC model empirically, by postulating that $n_n(t) = nt^4$, $n_s = n(1-t^4)$, where $t \equiv T/T_c$ is reduced temperature. As a result, the London penetration depth (3.5) is given by

$$\lambda_L(T) = \frac{\lambda_L(0)}{\sqrt{1-t^4}}. \tag{3.19}$$

The relaxation time τ in the Gorter–Casimir model is independent of temperature. This is quite natural if we assume that the behaviour of normal carriers in superconductors is similar to that of normal carriers in normal metals. Scattering of electrons at low temperatures (in conventional superconductors $T_c < 10$ K) is due to impurities and independent of the temperature. Therefore the temperature dependence of the conductivity components (3.8), (3.9) in the GC model is determined by the functions $n_n(T)$ and $n_s(T) = n - n_n(T)$ only. These dependences are shown in the inset to Figure 3.1.

The components (3.17) of the surface impedance reduces with help of (3.9) to

$$R_s \approx \omega^2\mu_0^2\lambda_L^3 n_n e^2\tau/2m \propto t^4/(1-t^4)^{3/2}, \quad X_s \approx \omega\mu_0\lambda_L \propto (1-t^4)^{1/2}. \tag{3.20}$$

These expressions describe qualitatively well the temperature dependence of the surface impedance in a temperature range not too close to T_c where the condition $(n_s/n_n)(\omega\tau)^2 \ll 1$ holds. At low temperatures the functions $X_s(T)/X_n$ and

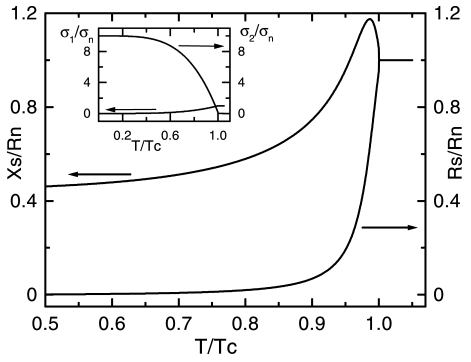

Figure 3.1 Real and imaginary parts of the surface impedance and complex conductivity (insert) in the Gorter–Casimir two-fluid model; the only parameter $\omega\tau = 0.1$.

$\sigma_2(T)/\sigma_n$ saturate rapidly as the temperature drops and achieve their limits $(2\omega\tau)^{1/2}$ and $(\omega\tau)^{-1}$, corresponding to zero temperature, whereas $\sigma_1(T)$ and $R_s(T)$ tend to zero following a power law.

As follows from (3.18) in the immediate vicinity of the transition temperature there is a very narrow peak in the curve $X_s(t)$ at $t_m = (1 - \omega\tau/\sqrt{3})^{1/4}$, whose amplitude $X_s(t_m) \approx 1.16X_s(1)$. Such a peak has been observed in conventional superconductors tantalum and niobium [201, 202]. In accordance with (3.19) the penetration depth diverges near T_c as $\lambda_L(t) = \lambda_L/2\sqrt{1-t}$ and the function $\sigma_2(t)/\sigma_2(0) = 4(1-t)$ tends to zero at $T = T_c$ linearly with a slope equal to -4. At the same time, at $T = T_c$ the skin depth δ_s defined in (3.10) crosses over to the skin depth δ_n for a normal conductor.

The dependences of $R_s(T)/R_n$ and $X_s(T)/X_n$ from (3.15) based on the GC model are shown in Figure 3.1.

3.2.2 BCS Theory

Qualitatively, the London theory provides fairly satisfactory agreement with the experimental data for many real superconductors. For not too low temperatures and frequencies below 10 GHz, it can be used for practical estimates of losses in superconducting resonators and transmission lines. However in most cases this theory is not suitable for a quantitative comparison of temperature and frequency dependences of the surface impedance with experimental data.

The electrodynamics of superconductors in the framework of the BCS theory was first discussed by Mattis and Bardeen [137] and Abrikosov, Gor'kov and Khalatnikov [6]. The general electrodynamic formulas are given in the review of Nam [151].

In the local limit $qv_F \ll \Delta$ complex conductivity $\sigma(\omega)$ of an isotropic superconductor can be written in the form [137, 6, 151]

$$\begin{aligned}\sigma(\omega) = \frac{i\omega_{pl}^2}{\mu_0\omega}\int \mathrm{d}\,\omega' \tanh\left(\frac{\omega+\omega'}{2T}\right)\\ \times\left(\frac{N^*(\omega+\omega')N^*(\omega')+D^*(\omega+\omega')D^*(\omega')-1}{\epsilon^*(\omega+\omega')+\epsilon^*(\omega')+i\gamma_{\text{imp}}}\right)\\ -\tanh\left(\frac{\omega'}{2T}\right)\left(\frac{N(\omega+\omega')N(\omega')+D(\omega+\omega')D(\omega')-1}{\epsilon(\omega+\omega')+\epsilon(\omega')+i\gamma_{\text{imp}}}\right)\\ +\left[\tanh\left(\frac{\omega+\omega'}{2T}\right)--\tanh\left(\frac{\omega'}{2T}\right)\right]\\ \times\left(\frac{N(\omega+\omega')N^*(\omega')+D(\omega+\omega')D^*(\omega')-1}{\epsilon(\omega+\omega')-\epsilon^*(\omega')+i\gamma_{\text{imp}}}\right). \end{aligned} \tag{3.21}$$

Here ω_{pl} is the plasma frequency in a given direction: $\omega_{pl} = 2N(0)e^2v_F^2/3$ for the spherical Fermi surface and $\omega_{pl} = 2N(0)e^2v_F^2$ for the cylindrical one. The values γ_{imp} represent the electron relaxation rate due to impurity scattering treated in the Born approximation, $\epsilon(\omega) = \sqrt{\omega^2-\Delta^2}$ is an excitation energy, $N(\omega) = \omega/\epsilon(\omega)$, $D(\omega) = \Delta/\epsilon(\omega)$. An imaginary part of the conductivity at low frequencies can be expressed in terms of the inverse penetration depth $\mathrm{Im}\,\sigma(0) = 1/\mu_0\omega\lambda_L^2$.

Let us consider the properties of the real part of the conductivity σ_1 in more detail. In the low-frequency limit, $\hbar\omega \ll \Delta$,

$$\begin{aligned}\sigma_1(\omega) = \mathrm{Re}\,\sigma(\omega) \simeq \frac{\omega_{pl}^2}{\mu_0 T}\int_0^\infty \frac{\mathrm{d}\,\omega'}{\cosh^2(\omega'/2T)}\\ \times \mathrm{Re}\left[1+N(\omega+\omega')N^*(\omega')+D(\omega+\omega')D^*(\omega')\right]\\ \times \mathrm{Im}\left(\frac{1}{\epsilon^*(\omega+\omega')-\epsilon(\omega')-i\gamma_{imp}}\right). \end{aligned} \tag{3.22}$$

Equation (3.22) can be further simplified in the dirty limit, $l \ll \xi$, at low frequencies $\omega \ll \Delta(T)$ and temperatures not too close to T_c (i.e., $\Delta(T) \sim T$). In this case

$$\frac{\sigma_1(T)}{\sigma(T_c)} \simeq \frac{\Delta(T)}{2k_BT}\cosh^{-2}\left(\frac{\Delta(T)}{2k_BT}\right)\ln\left(\frac{\Delta(T)}{\hbar\omega}\right). \tag{3.23}$$

As follows from the expression (3.23), the BCS theory [22] predicts two distinctive features in the T-dependence of the superconductor microwave response [22, 137, 6], namely an exponential drop in $\sigma_1(T)$ and $R_s(T) \propto \exp(-\Delta(0)/kT)$ in the range $T < 0.5T_c$, and an increase in the conductivity $\sigma_1(T)$ for $0.7 < T/T_c \leq 1$ with respect to its value σ_n at $T = T_c$. The first feature is due to the thermally activated generation of normal quasiparticles above the gap $\Delta(T)$, while the second one, the so-called 'coherent peak', is due to the logarithmic factor in (3.23), i.e.,

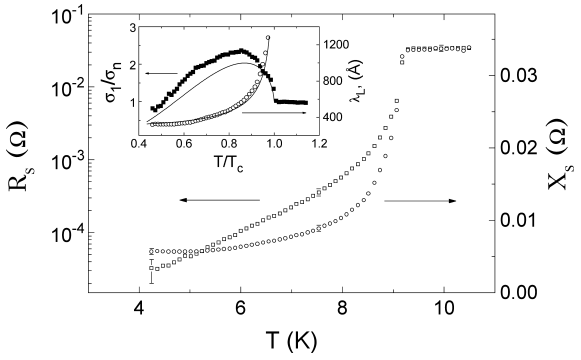

Figure 3.2 Plots of $R_s(T)$ and $X_s(T)$ in Nb. The inset shows the real part of the conductivity, σ_1/σ_n, and Londons' field penetration depth, λ_L, versus temperature derived from measurements of $R_s(T)$ and $X_s(T)$ using (3.12) and (3.13). The solid curves show calculations based on the BCS formula (3.23).

the singularities in the quasiparticle and pair densities of states $N(\omega)$ and $D(\omega)$ at a quasiparticle energy equal to $\Delta(T)$.

The exponential behaviour of $R_s(T)$ in conventional superconductors has been studied in detail (see, for example, [199] and references therein). On the other hand, the coherent peak in $\sigma_1(T)$ in the region $T \sim 0.85T_c$ was detected not so long ago in Nb and Pb at a frequency of 60 GHz [111] and in Nb at 10 GHz [192], when highly accurate concurrent measurements of $R_s(T)$ and $X_s(T)$ had become possible. Figure 3.2 shows as an example measurements of $R_s(T)$ and $X_s(T)$ of a niobium sample, whose critical temperature is $T_c = 9.2$ K. These measurements were obtained using the 'hot finger' technique, which is convenient for studies of HTS crystals whose surface area is usually small ($\sim$ 1 mm^2). The symbols (■) plot the function $\sigma_1(T)/\sigma_n$ derived from measurements of $R_s(T)$ and $X_s(T)$ using (3.16). These data are in qualitative agreement with calculations (solid curve) based on the BCS formula (3.22).

Note that in the BCS model the magnitude of the scattering rate strongly affects the function $\sigma_1(T)/\sigma(T_c)$. To illustrate this we have plotted in Figure 3.3 the conductivities calculated from (3.22) for a number of the l's [71]. It can be seen that the coherent peak disappears as the clean limit is approached, i.e., if the mean free path of electrons in the normal state $l > 10\xi_0$. For HTS single crystals such large l values are irrelevant.

The first measurements of functions $Z_s(T)$ and $\sigma_s(T)$ in HTS crystals did not show the behaviour predicted by the BCS theory. In particular, instead of a broad coherent peak in $\sigma_1(T)$, a narrow peak (it is shown by the dashed line in Figure 3.4) with a width close to that of the superconducting transition, which can been seen in the curve of $R_s(T)$, was observed. In principle, one more possibility of modifying the result for $\sigma_1(T)/\sigma(T_c)$ in the BCS model, is to change the ratio $2\Delta/T_c$. As was shown in [38], for $2\Delta/T_c > 3.52$ the coherent peak for given values of ω and

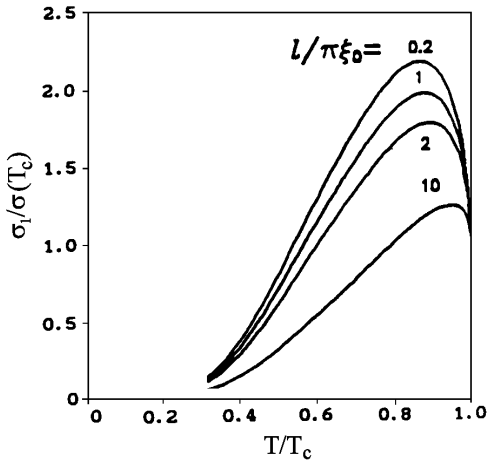

Figure 3.3 Dependence of the coherent peak on the mean free part l; $\omega/\Delta_0 = 0.02$.

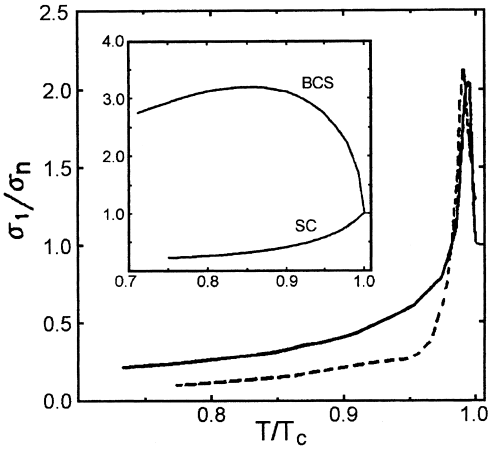

Figure 3.4 Comparison between measurements (dashed line, YBCO crystal) of σ_1/σ_n and calculations based on the SC model taking into account inhomogeneous broadening of the superconducting transition (solid line). The inset shows σ_1/σ_n as a function of temperature calculated using the BCS and SC models [71].

l/ξ_0 becomes narrow; but to fit the experimental data in Figure 3.4 one should take unrealistically large values of $2\Delta/T_c \sim 100$. This disagreement between the BCS model and microwave measurements of HTS is not surprising because there exist many analogous claims in the literature, which give evidence that strong-coupling effects play an important role in superconducting pairing of HTS.

3.2.3 Eliashberg Model

A generalized version of the BCS theory for the case of strong electron–phonon coupling was developed by Eliashberg [50]. According to [151], the complex conductivity $\sigma(\omega)$ in this case is given again by the expression (3.21), in which

$$\epsilon(\omega) = Z(\omega)\sqrt{\omega^2 - \Delta^2(\omega)} \tag{3.24}$$

is the energy of quasiparticles and $Z(\omega)$ is Migdal's renormalization function.

In strong coupling regime functions $\Delta(\omega)$ and $Z(\omega)$ become complex, have an energy dispersion and obey the set of Eliashberg equations

$$[1 - Z(\omega)]\omega + i\gamma_{imp}N(\omega) = \int \mathrm{d}\omega' \times \int \mathrm{d}\Omega\, \alpha^2F(\Omega)I(\omega + i\delta, \Omega, \omega')\,\mathrm{Re}\,N(\omega'), \tag{3.25}$$

$$Z(\omega)\Delta(\omega) + i\gamma_{\mathrm{imp}}D(\omega) = -\int \mathrm{d}\omega' \times \int \mathrm{d}\Omega\, \alpha^2F(\Omega)I(\omega + i\delta, \Omega, \omega')\,\mathrm{Re}\,D(\omega'), \tag{3.26}$$

where

$$I(\omega + i\delta, \Omega, \omega') = \frac{N(\Omega) + 1 - f(\omega')}{\omega + i\delta - \Omega - \omega'} + \frac{N(\Omega) + f(\omega')}{\omega + i\delta + \Omega - \omega'}. \tag{3.27}$$

Here $N(\omega) = \omega/\sqrt{\omega^2 - \Delta^2(\omega)}$, $D(\omega) = \Delta(\omega)/\sqrt{\omega^2 - \Delta^2(\omega)}$, $N(\Omega)$ and $f(\omega)$ are Bose and Fermi distribution functions and $\alpha^2F(\Omega)$ is the spectral function of electron–phonon interaction. The coupling constant g is defined as

$$g = 2\int_0^\infty (\alpha^2F(\Omega)/\Omega)\ \mathrm{d}\Omega.$$

The quasiparticle lifetime is given by $1/\tau(\omega, T) = 2\omega\,\mathrm{Im}\,Z(\omega, T) + \gamma_{\mathrm{imp}}$, where γ_{imp} is the impurity scattering rate in the Born (weak scattering) limit. Note that, according to the strong-coupling (SC) theory for conductivity, the quantities

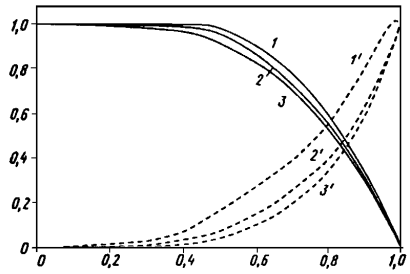

Figure 3.5 Relative-temperature dependences of the functions $\sigma_2(T)/\sigma_2(0)$ (solid lines) and $\sigma_1(T)/\sigma(T_c)$ (dashed lines) for the coupling constants $2(1,1'), 3.5(2,2')$ and $5(3,3')$ (from the top to the bottom, respectively) [102].

$\sigma(\omega)$ and $\tau(\omega)$ are related by an integral equation. As a result, as shown in [44] the simple Drude-type formula

$$\sigma(\omega) = i\frac{\omega_{pl}^2}{\mu_0}\frac{1}{\epsilon(\omega) + i/\tau(\omega)}, \tag{3.28}$$

which is often used for data analysis, is valid only in the weak coupling limit when the energy dispersion of all corresponding quantities is weak.

It follows from the Eliashberg theory that the distinctive feature of superconductors with strong coupling is that the gap in the spectrum of electronic excitations is smeared. Strictly speaking, there is no gap whatever at $T \neq 0$ [51, 101]. This leads to breaking of Cooper pairs, smearing of the peak in the density of states at $\omega = \Delta(T)$ due to inelastic scattering of electrons by thermally excited phonons, and suppression of coherence effects. As a result, the amplitude of the coherent peak decreases and, according to [135, 102], virtually disappears at frequencies around 10 GHz if the electron–phonon coupling constant $g > 2$. This behaviour is shown by dashed lines in Figure 3.5 and in the inset to Figure 3.4. Moreover, the mechanism of quasiparticle generation is radically different from that of the BCS model. They are generated without jumps across the energy gap and can be in states with all energies down to $\hbar\omega = 0$. These states can be classified as gapless, and the quasiparticles can be treated as normal current carriers in the two-fluid model [66, 131]. So it is not surprising that an important consequence of the SC model is the nonexponential behavior of $R_s(T)$ [45] and $\lambda(T)$ [116]. Power-law temperature dependences were also predicted by the two-fluid GC model (see (3.19, 3.20)), and near T_c they proved to be quite close to calculations by the SC model [144]. However, whereas the agreement between experimental curves on the one hand and calculations by the SC and GC models [144, 40, 167, 14] on the other, in the neighbourhood of T_c, could be deemed satisfactory, deviations in the low-temperature range were enormous. As

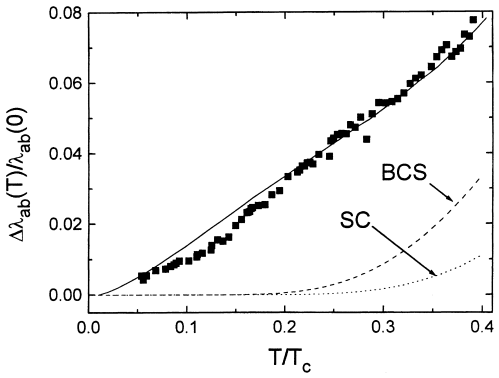

Figure 3.6 Curves of $\Delta\lambda_{ab}(T)$ in the low-temperature range. The squares plot the data from [154]. The solid line shows calculations by the two-band model [69] (see Section 3.5). The dotted line is a calculation by the BCS model, the dashed line by the isotropic SC model [71].

an example, measurements of $\Delta\lambda_{ab}(T)$ in the ab-plane of YBCO given in [154] are compared with BCS and SC curves [69] in Figure 3.6. A curve predicted by the GC phenomenological theory would be an almost horizontal straight line in this graph.

The first high-quality YBCO crystals were manufactured at the University of British Columbia (UBC group) by Liang *et al.* [125]. A broad peak in the surface resistance versus temperature, $R_s(T)$, centred at $T \approx 35$ K in those crystals was first reported by Bonn *et al.* [30], and a linear dependence $\Delta\lambda_{ab}(T) \propto T$ in the range $4 < T < 25$ K by Hardy *et al.* [78]. These results, which seemed very unusual from the viewpoint of traditional models of the microwave response of superconductors, generated an intense discussion of the symmetry of the order parameter in HTS and the role of quasiparticle scattering, and stimulated development of theoretical models of the high-frequency response. By the present time, the first experimental data concerning YBCO single crystals [78, 30] have been confirmed by experimenters from other laboratories. When high-quality BSCCO, TBCCO, and TBCO single crystals had become available, it was possible to discuss common and distinctive features in the impedance and conductivity as functions of temperature of various HTS crystals. This discussion will be presented below.

3.3 EXPERIMENTAL PROCEDURE

3.3.1 Principles of the 'Hot Finger' Technique

The most convenient technique for measurements of the surface impedance of small HTS samples in the X–W microwave frequency bands is the so-called 'hot finger' method. Measurements using this method in the centimetre wavelength band have

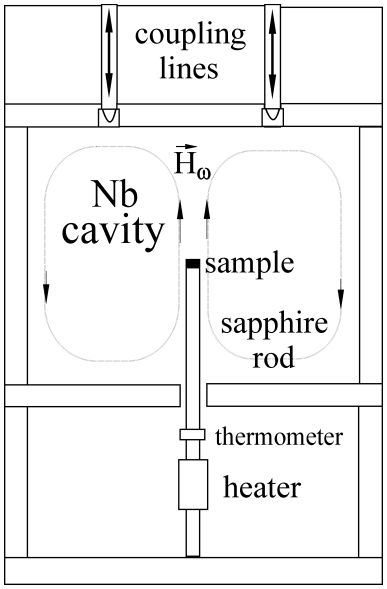

Figure 3.7 Diagram of the microwave cavity used in the 'hot-finger' technique.

been conducted at Northeastern University (NEU) [184], UBC [32], Maryland University [133], University of Tokyo [182], Cambridge University, University of California [113], and at the Institute of Solid State Physics (ISSP) [196]. The underlying idea of the method is that a sample is set on a sapphire rod at the centre of a superconducting cylindrical cavity resonating at the H_{011} mode, i.e., at the antinode of a quasihomogeneous microwave magnetic field (Figure 3.7). By varying the rod temperature, measuring the Q-factor and frequency shift Δf of the cylindrical cavity, and comparing them with the parameters of the empty cavity, Q_0 and Δf_0, one can determine the sample surface resistance R_s and reactance X_s as functions of temperature.

Electromagnetic modes driven by an external source are characterized in a lossy cavity by a complex frequency [11]

$$\hat{\omega}_i = \omega_i + \frac{i\omega_i}{2Q_{iL}}, \tag{3.29}$$

where $\omega_i = 2\pi f_i$ and Q_{iL} are the inherent frequency and Q-factor of the loaded cavity. For a cavity operated in the transmission mode

$$\frac{1}{Q_{iL}} = \frac{1}{Q_i} + \frac{1}{Q_1} + \frac{1}{Q_2}. \tag{3.30}$$

Here Q_i is the inherent Q of the unloaded cavity, Q_1 and Q_2 are the input and output Q's, which characterize the coupling between the cavity and external microwave

circuits. In (3.29) and (3.30) $Q_{iL} = Q_L$, $Q_i = Q$, and $f_i = f$ if there is a sample in the cavity; $Q_{iL} = Q_{0L}$, $Q_i = Q_0$, and $f_i = f_0$ for the cavity without a sample but with a sapphire rod inside.

The difference between the averaged microwave powers absorbed in the cavity with a sample and the empty cavity is the power P directly absorbed in the sample:

$$P = \frac{1}{2} \int\limits_S R_s H_s^2 \, \mathrm{d}S, \tag{3.31}$$

where H_s is the tangential component of the microwave magnetic field on the sample surface, and integration is performed over the area S of the entire sample surface. The energy stored in the cavity is

$$W = \frac{\mu_0}{2} \int\limits_V H^2 \, \mathrm{d}V, \tag{3.32}$$

where V is the inside volume of the cavity, and H^2 is the magnetic field squared generated in the cavity with the sample inside. The difference between the reciprocal Q-factors of the cavity is determined by the relation

$$\frac{1}{Q} - \frac{1}{Q_0} = \frac{P}{\omega W} = \frac{R_s \int_S H_s^2 \, \mathrm{d}S}{\omega \mu_0 \int_V H^2 \, \mathrm{d}V} = \frac{R_s}{\Gamma_s}, \tag{3.33}$$

where

$$\Gamma_s = \frac{\omega \mu_0 \int_V H^2 \, \mathrm{d}V}{\int_S H_s^2 \, \mathrm{d}S} \tag{3.34}$$

is the sample geometrical factor.

Let the complex resonant frequency of the loaded cavity be $\hat{\omega}$ and the frequency of the cavity without a sample $\hat{\omega}_0$. The frequency difference $\hat{\omega} - \hat{\omega}_0$ is the frequency shift caused by the sample, $\hat{\omega}_s$. Provided that the coupling Q-factors Q_1 and Q_2 are constant, we derive from (3.29), (3.30), and (3.33) the value of $\hat{\omega}_s$:

$$\hat{\omega}_s = \omega_s + \frac{i\omega R_s}{2\Gamma_s}. \tag{3.35}$$

A change in the sample temperature leading to a change in its impedance, $\Delta Z_s(T) = \Delta R_s(T) + i\Delta X_s(T)$, can be treated as a small perturbation resulting in the shift $\Delta\hat{\omega}_s(T)$ in the complex frequency $\hat{\omega} = \hat{\omega}(Z_s)$:

$$\Delta\hat{\omega}_s(T) = \frac{\partial\hat{\omega}}{\partial Z_s}\Delta Z_s = \frac{\partial\hat{\omega}}{\partial Z_s}(\Delta R_s + i\Delta X_s). \tag{3.36}$$

On the other hand, as follows from (3.35),

$$\Delta\hat{\omega}_s(T) = \frac{i\omega}{2\Gamma_s}\left(\Delta R_s - \frac{2i\Gamma_s\Delta\omega_s(T)}{\omega}\right), \tag{3.37}$$

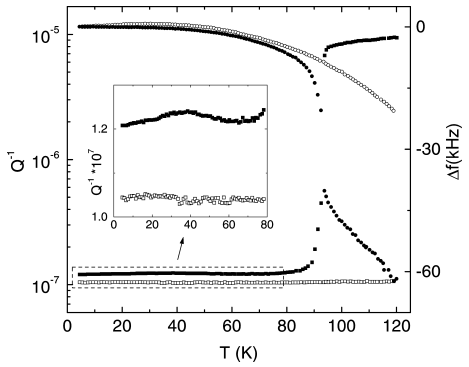

Figure 3.8 Temperature dependences of $1/Q$ and Δf measured in a YBCO single crystal. The full symbols correspond to the cavity with sample inside, the open symbols depict data from the empty cavity.

hence, by comparing this to (3.36), we obtain the change in the sample surface reactance

$$\Delta X_s(T) = -\frac{2\Gamma_s \Delta\omega_s(T)}{\omega}, \tag{3.38}$$

where $\Delta\omega_s(T) = \Delta\omega(T) - \Delta\omega_0(T)$.

Thus, measurements of the real $R_s(T)$ and imaginary $X_s(T)$ parts of the surface impedance are derived from experimental curves of $Q_i(T)$ and $\Delta f_i(T)$ using the relations

$$\begin{aligned} R_s(T) &= \Gamma_s[Q^{-1}(T) - Q_0^{-1}(T)], \\ X_s(T) &= -\frac{2\Gamma_s}{f_0}[\Delta f(T) - \Delta f_0(T)] + X_0, \end{aligned} \tag{3.39}$$

where Γ_s is the sample geometrical factor given by (3.34) and X_0 is an additive constant.

Figure 3.8 shows the recorded temperature dependences of the $Q_0(T)$-factor and resonance frequency shift $\Delta f_0(T)$ for an empty cavity as well as for the cavity containing a YBCO single crystal ($Q, \Delta f$). The Q_0-factor (open squares) is practically independent of temperature, while the pronounced monotone change in Δf_0 (open circles) is due to the temperature dependence of the dielectric constant and thermal expansion of the sapphire rod. The data depicted in Figure 3.8 correspond to the measurements carried out on a thick rod of diameter 3.5 mm. The use of a thin rod (1.5 mm in diameter) leads to a decrease in the shift $\Delta f_0(T)$ by an order of magnitude over the temperature range $4.2 \leq T \leq 130$ K.

As follows from (3.39), measurements of two quantities are needed to determine $R_s(T)$ and $X_s(T)$ in absolute units, namely X_0 and Γ_s. In measuring these quantities, one should take into account the strong anisotropy of layered HTS single

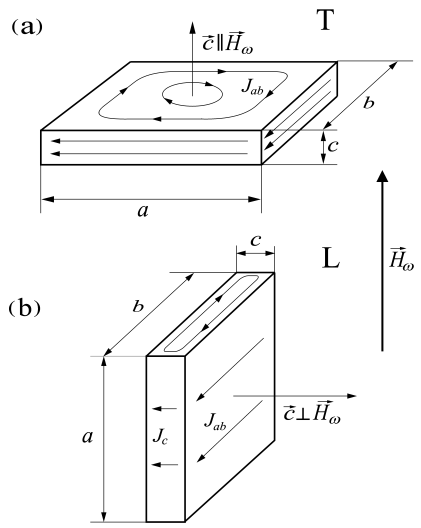

Figure 3.9 (a) Transverse orientation of a sample with respect to microwave magnetic field, $\boldsymbol{H}_\omega \| \boldsymbol{c}$; arrows on the surfaces show directions of microwave currents; (b) longitudinal orientation, $\boldsymbol{H}_\omega \perp \boldsymbol{c}$.

crystals, which manifests in the notable difference between transport parameters in the ab-plane and along the c-axis. Therefore values of Γ_s and X_0, and the technique of their determination depend on the crystal alignment (Figure 3.9) with respect to the microwave magnetic field $\boldsymbol{H}_\omega$, which points along the cavity axis.

3.3.2 Samples and Their Geometrical Factors

The ways of determination of the values of Γ_s and X_0 in the transverse ($\boldsymbol{H}_\omega \| \boldsymbol{c}$, Figure 3.9a) and longitudinal ($\boldsymbol{H}_\omega \perp \boldsymbol{c}$, Figure 3.9b) orientations of the crystal were discussed in review [190]. Measurements of the surface impedance $Z_s^{\boldsymbol{H}_\omega \perp \boldsymbol{c}}(T)$ in the longitudinal orientation [134, 97, 179, 175, 110, 181, 110, 31, 188, 92, 191] are interesting primarily because they yield information about anisotropic properties of HTS crystals. This paper is mainly dedicated to the analysis of the ab-microwave response in the transverse orientation (Figure 3.9a) of high-T_c single crystals, which usually have the shape of a plate with dimensions $a \sim b \sim 1$ mm, $c \sim 0.1$ mm. In this case a sample is set on the end of a sapphire rod so that the crystal c-axis is aligned with the microwave magnetic field, $\boldsymbol{H}_\omega \| \boldsymbol{c}$, and high-frequency currents, which determine the sample microwave response in both normal and superconduct-

ing states, circulate in the ab-planes. At $T < 0.9T_c$ the field $\boldsymbol{H}_\omega$ penetrates into the sample to a depth $\lambda_{ab} \sim 10^{-4}$ mm, at $T \geq T_c$ to the skin depth $\delta_{ab} = \sqrt{2\rho_{ab}/\omega\mu_0}$, which is $\delta_{ab} \sim 5 \times 10^{-3}$ mm at a frequency of ~ 10 GHz and the resistivity $\rho_{ab}(T_c) \sim 100$ $\mu\Omega$ cm typical of HTS crystals. Since $\lambda_{ab} \ll c$ and $\delta_{ab} \ll c$, then, neglecting the anisotropy in the ab-plane, it is possible: (i) to treat the impedance Z_s^{ab} as a parameter defined similarly to the case of a semi-infinite isotropic sample at all temperatures; (ii) to consider the distribution of field H_s, hence the parameter Γ_s in (3.34), to be approximately constant with temperature.

For all HTS single crystals the inequality $\delta \gg l$, which is equivalent to the criterion of the normal skin effect, holds. For this reason, the constant X_0 in (3.39) for $\boldsymbol{H}_\omega \| \boldsymbol{c}$ is derived from the condition of equality between the real and imaginary parts of the normal state impedance, and the identity of the temperature dependences $R_s^{ab}(T)$ and $X_s^{ab}(T)$ in the range $T \geq T_c$ provides a simple test of the measuring technique.

Statements (i) and (ii) give a clue to how the sample geometrical factor Γ_s^{ab} can be determined in the transverse orientation. Firstly, one can use a metallic simulator of the tested sample of the same shape and dimensions, provided that the conditions of the normal skin effect hold. Given the simulator resistivity as a function of temperature, $\rho(T)$, and having measured $Q_i(T)$ and $\Delta f_i(T)$ of the cavity containing the simulator, one can use the relation

$$\rho(T) = \frac{2R_s^2(T)}{\omega\mu_0} \tag{3.40}$$

and derive from (3.39) the value of Γ_s, assuming that it equals the geometrical factor Γ_s^{ab} of the HTS crystal. Secondly, having measured $Q_i(T)$ and $\Delta f_i(T)$ of the empty cavity and of the cavity loaded with the HTS crystal, one can directly measure $\rho_{ab}(T)$ of the sample and derive Γ_s^{ab} using (3.39) and (3.40). This procedure, however, leads to degradation of a sample, because electric contacts should be attached to its surface. Nonetheless, we employed this technique in determination of Γ_s^{ab} of two TBCCO and YBCO single crystals grown at ISSP using the techniques described in [117] and [193], respectively. Their dimensions were about $a \times b \times c \approx 1 \times 1 \times 0.1$ mm^3 (TBCCO) and $1.7 \times 1.7 \times 0.1$ mm^3 (YBCO). In particular, the geometrical factor of the YBCO crystal proved to be $\Gamma_s^{ab} \approx 1.8 \times 10^4$ Ω.

We attempted to develop a method for estimating numerically the geometrical factor based on (3.34), assuming that a sample has the shape of a square plate with dimensions $a \times a \times c$, $c \ll a$, and the magnetic field amplitude at the centre of the unperturbed cavity is H_0 [190]. The calculation procedure considers the sample as a thin plate with slightly rounded edges [26]. This approach yields the well-known geometrical barrier to penetration of flux lines from the sample edges [26, 215, 94]. In this case, the field distribution on the edges of a plate in the Meissner state is given by the formula [26] $H_s(x) = H_0 x/\sqrt{(a/2)^2 - x^2}$, $-a/2 + c/4 \leq x \leq a/2 - c/4$, with the exception of a very narrow region ($\approx c/4$) near the edge, where the integral $\int_S H_s^2 \, \mathrm{d}S$ is logarithmically divergent. On the edges of the sample, the field is assumed to be homogeneous and equal to $H_{\mathrm{edge}} \approx H_0\sqrt{a/c}$. As a result, we obtain

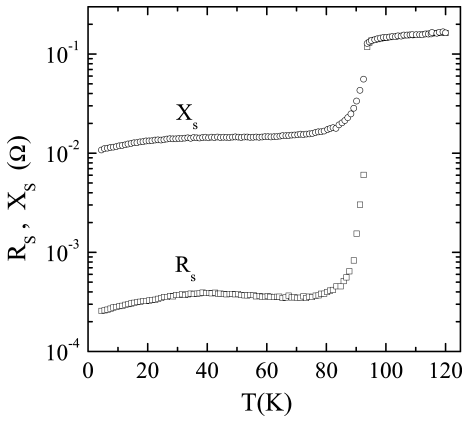

Figure 3.10 Surface resistance R_s and reactance X_s of a YBCO single crystal as functions of temperature.

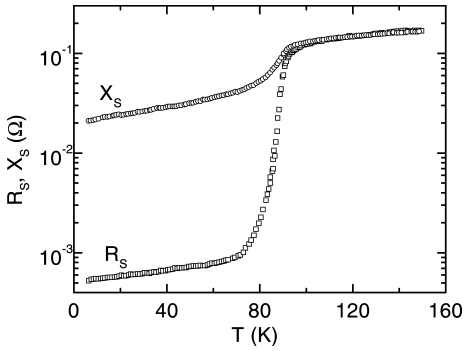

Figure 3.11 Surface resistance R_s and reactance X_s of a BSCCO single crystal versus temperature.

the geometrical factor of HTS crystals for the case of their transverse alignment with respect to the microwave field $\boldsymbol{H}_\omega$ in the cavity:

$$\Gamma_s = \frac{\omega\mu_0 V}{4\gamma_0 A}\left(\ln\left(\frac{a}{c}\right)+1\right)^{-1}, \quad \gamma_0 = \frac{V{H_0}^2}{2\int_V H^2\,\mathrm{d}V}, \tag{3.41}$$

where A is the area of the ab-face of the crystal, γ_0 is a constant determined by the known [164] field configuration of the resonant mode H_{011}. In the cavity used in our experiments, whose diameter and height were 42 mm ($f = 9.4$ GHz), this constant $\gamma_0 = 5.3$. The calculations of Γ_s by (3.41) for thin single crystals were in satisfactory agreement with experimental data. Figures 3.10 and 3.11 show the measurements of $R_s(T)$ and $X_s(T)$ in YBCO ($\Gamma_s \approx 1.8\times10^4$ Ω) [193] and BSCCO

($a \times b \times c \approx 1.5 \times 1.5 \times 0.1$ mm^3, $\Gamma_s \approx 2.4 \cdot 10^4$ Ω) [175] samples respectively. They demonstrate the behaviour typical of the HTS single crystal impedance for $\boldsymbol{H}_\omega \| \boldsymbol{c}$.

3.3.3 Accuracy of Measurements

The uncertainty δR_s in measurements of the surface resistance, $\delta R_s = \Gamma_s \delta(Q^{-1} - Q_0^{-1}) = \Gamma_s \delta Q / Q^2$, is determined by the uncertainty $\delta Q/Q$, which was within 1% at $Q \sim 10^7$ in our experiments. If $\Gamma_s = 10$ kΩ, then we have $\delta R_s \approx 10$ μΩ. As the temperature drops several degrees below T_c, the increment $\Delta X_s(T) = \omega \mu_0 \Delta\lambda(T)$, and, given $X_s(T)$ expressed in absolute units, one can determine the magnetic field penetration depth $\lambda(T) = X_s(T)/\omega\mu_0$. The uncertainty in the relative value of the penetration depth is $\Delta\lambda(T)$, $\delta(\Delta\lambda) = (2\Gamma_s/\omega\mu_0)(\delta(\Delta\omega)/\omega)$, which equals several ångström. The error in $\lambda(T)$ can be up to 30% of the actual value $\lambda(0)$ and is largely determined by the measurement accuracy of the constant X_0.

The source of possible errors in measurements of $\lambda(T)$ is thermal expansion of the sample. Since the resonant frequency is determined by the volume where the microwave field is confined, the thermal expansion of the sample is equivalent to a smaller penetration depth of the microwave field, and this leads to an additional frequency shift Δf_l in the brackets on the right of (3.39). Changes Δl_i (Δa and Δc) in the sample dimensions $a \times a \times c$, where $c \ll a$, due to thermocycling lead to a change in its volume by $(\Delta c \cdot a^2 + 2\Delta a \cdot ac)$ and an additional shift of the cavity resonant frequency

$$\Delta f_l(T) = \frac{f_0 \mu_0}{4W} \int\limits_S \Delta l_i(T) H_s^2 \, \mathrm{d}S, \tag{3.42}$$

where W is given by (3.32). The comparison of this contribution with the resonant frequency shift $\Delta f_\lambda(T)$ due to the change in the field penetration depth $\Delta\lambda_{ab}(T)$ show that [196, 190]

$$\frac{\Delta f_l}{\Delta f_\lambda} = \frac{\Delta c/2(\ln(\,a/c) - 1) + \Delta a}{\Delta\lambda_{ab}(\ln(a/c) + 1)}. \tag{3.43}$$

In YBCO and BSCCO single crystals with $T_c \simeq 90$ K, λ_{ab} increases by about one thousand ångströms as the temperature grows from 4.2 K to 80 K, and at $T > 80$ K the growth rate is considerably higher. Experimental data indicate that at $T < 30$ K the relative change in dimensions of YBCO [214, 141, 142] and BSCCO [107, 143] crystals, $\varepsilon = \Delta l_i / l_i$, is very small, $\varepsilon_i < 10^{-5}$. In the temperature range $30 < T < 100$ K the thermal expansion coefficient $\alpha_i = \mathrm{d}\varepsilon_i / \mathrm{d}T$ is an almost linear function of temperature T: moreover, in the ab-plane of YBCO crystals $\alpha_{ab} \approx 0.3 \times 10^{-7} T$, and in the direction of the c-axis $\alpha_c \approx 10^{-7} T$. Hence we have $\varepsilon_{ab} \approx 10^{-4}$ and $\varepsilon_c \approx 3 \times 10^{-4}$, and for typical crystal dimensions $a \approx b \approx 1$ mm and $c \approx 0.1$ mm they increase by $\Delta a \approx \Delta b \approx 1000$ Å and $\Delta c \approx 300$ Å when the temperature grows from 30 to 100 K. In BSCCO single crystals ε_{ab} is twice as large,

and ε_c is approximately the same as in YBCO. We are unacquainted with data on thermal expansion of TBCO and TBCCO at temperatures $T \leq T_c$.

Thus, the contribution of $\Delta f_l(T)$ to the total frequency shift of the cavity with a sample inside is negligible in the range of low temperatures $T < 40$ K. However, at higher temperatures it may be quite considerable, especially for BSCCO single crystals. This circumstance should be taken into account when using (3.39) in determination of $\lambda_{ab}(T) = X_s(T)/\omega\mu_0$. In particular, the curve of $X_s(T)$ in Figure 3.11 was plotted with due account of the thermal expansion of the BSCCO sample. Otherwise, i.e., when the thermal shift Δf_l in (3.39) is negligible, the curve of reactance, which follows that plotted in Figure 3.11 up to $T \approx T_c$, has a smaller slope at $T > T_c$, and the discrepancy is 25 mΩ at $T = 150$ K. Since the thermal expansion of samples is not measured in microwave experiments, the only criterion of the authenticity of experimental curves of $\lambda_{ab}(T)$ is their reproducibility for crystals of various sizes.

3.4 EXPERIMENTAL RESULTS

3.4.1 Surface Impedance of YBCO, BSCCO, TBCCO, and TBCO Single Crystals: Their Common and Distinctive Features

First measurements of the surface impedance of HTS materials in the microwave band date back to the time of their discovery in 1986–1987. The first microwave experiments with ceramic samples, as well as thin films and single crystals, which were produced soon after the discovery of HTS, were rare and produced only rough estimates of HTS parameters since the quality of those samples left much to be desired. An important parameter of HTS crystals characterizing their quality is the residual surface resistance $R_{\rm res} = R_s(T \to 0)$, which is the loan-term taken from the terminology of conventional superconductors. There is, however, a marked difference between these two cases: whereas $R_{\rm res}$ in conventional superconductors is clearly defined as the level of the plateau on the $R_s(T)$ curve in the region $T < T_c/4$, no plateau has been detected on the characteristic curves of the $R_s(T)$ in HTS (see below), and $R_{\rm res}$ is set to the value $R_s(T = 0)$, which is obtained by extrapolating to the zero temperature the linear section of the $R_s(T)$ curve in the region $T \ll T_c$. It was found in experiments with conventional superconductors [199] that the parameter $R_{\rm res} \propto \omega^2$ and is determined by various defects in the surface layers of samples, therefore, it is generally accepted that the sample quality is the higher, the lower $R_{\rm res}$. The residual surface resistance of HTS materials is also approximately proportional to the microwave frequency squared, but its value was several orders of magnitude higher than $R_{\rm res}$ in conventional superconductors like Nb or Pb. It was clear to everyone that high-frequency properties of HTS materials were largely determined by irregularities in their structures, namely their inhomogeneity, the presence of weak links, twins and other defects in their surface layers.

The situation changed radically in 1992–1993, when first high-quality YBCO single crystals [78, 30, 125] and thin films [112] with considerably smaller $R_{\rm res}$

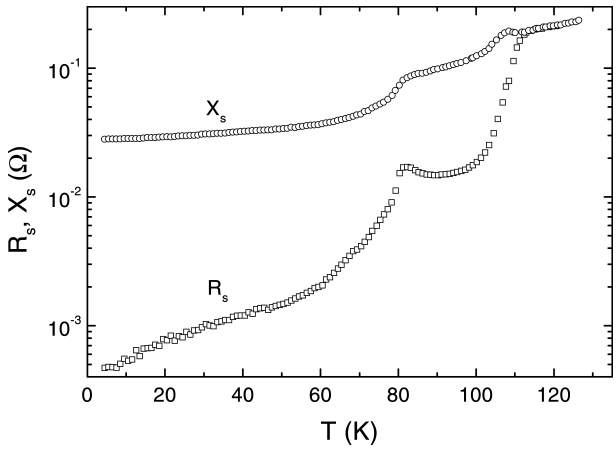

Figure 3.12 Surface resistance R_s and reactance X_s of a TBCCO single crystal versus temperature.

had been manufactured. Measurements of those samples revealed a temperature dependence of the surface impedance, $Z_s(T)$, which could not have been detected in earlier experiments against the background of high residual losses. The UBC group detected for the first time

(a) linear dependences $\lambda_{ab}(T)$ and $R_s(T)$ in the range $4 < T \lesssim 25$ K and
(b) a broad peak in $R_s(T)$ centred at about 40 K.

These features of $Z_s(T)$ in YBCO single crystals were confirmed by experiments performed by other groups [134, 98, 180, 193] and have been generally recognized by this time. Notice that features (a) and (b) can be observed only in YBCO crystals of the highest quality. Doping of initially perfect single crystals with Zn [7, 216, 32] changes the linear function $\lambda_{ab}(T)$ to quadratic and spreads the peak in $R_s(T)$. The dependence $\Delta\lambda_{ab}(T) \propto T^2$ is typical of YBCO thin films [18, 139, 161], in which impurities and weak links occur more frequently than in single crystals. Therefore it is generally accepted that the quadratic dependence $\lambda(T)$ is largely due to the presence of defects in samples (extrinsic origin), unlike the features (a) and (b), which are due to intrinsic microscopic properties of HTS materials. This conjecture was later confirmed by systematic research of YBCO thin films [203]: as their quality improved, the quadratic dependence $\lambda(T)$ in the low-temperature range was replaced by a linear function. A detailed analysis of the results mentioned above and concerning microwave studies of YBCO crystals and films before 1996 is given in the review by Bonn and Hardy [34].

Given the apparent difference between the temperature dependencies in YBCO and conventional superconductors, the natural question arose about the applicability of properties (a) and (b) to other HTS materials which, unlike YBCO, have a tetragonal structure and contain no Cu–O chains. The progress in the fabrication technol-

ogy of HTS samples has allowed the researchers to investigate microwave properties of BSCCO [180, 97, 179, 122, 175], TBCCO [217], and TBCO [35, 209] single crystals of high quality. In addition, the notable reduction in the homogenization time of growth solutions and in the time of crystal growth by the conventional technique [125] of YBCO manufacture in standard zirconium dioxide (ZrO_2) crucibles stabilized with yttrium, alongside the utilization of $BaZrO_3$ crucibles [54, 124], has allowed the production of high-purity YBCO crystals with resistivity $\rho(T_c) \approx 40\ \mu\Omega$ cm and residual surface resistance $R_{\rm res} \approx 100\ \mu\Omega$ cm at 10 GHz, i.e., lower than in previously reported experiments. Microwave measurements of such crystals produced using the accelerated growth technique in ZrO_2 and $BaZrO_3$ crucibles have been performed recently by the ISSP [193, 217], NEU [185, 186], and UBC [103, 91] groups. These measurements have demonstrated features (a) and (b) in the curves of $\lambda_{ab}(T)$ and $R_s(T)$, as well as new features of $Z_s(T)$ in the range of higher temperatures.

3.4.1.1 Surface Impedance in the Normal State

Examples of experimental curves $R_s(T)$ and $X_s(T)$ recorded in the transverse orientation, $\boldsymbol{H}_\omega \parallel \boldsymbol{c}$ (Figure 3.9a), are given in Figure 3.10 for an YBCO single crystal, in Figure 3.11 for a BSCCO crystal, and in Figure 3.12 for a TBCCO crystal. In all these graphs, $R_s(T) = X_s(T)$ for $T \geq T_c$, which indicates that the experiments were performed under the normal skin-effect conditions. The values of $X_s(T)$ were obtained using (3.39), in which the additive constant X_0 was determined by fitting measurements of $\Delta X_s(T)$ to $R_s(T)$ in the range $T \geq T_c$. The quantity $X_s(T)$ expressed in absolute units, in its turn, determines $\lambda(0) = X_s(0)/\omega\mu_0$. In the centimetre band of electromagnetic waves, typical values of the surface resistance in the ab-plane of high-T_c single crystals in the normal state near the critical temperature T_c are about 0.1 Ω. From the measurement of $R_s(T_c) = \sqrt{\omega\mu_0\rho(T_c)/2} \approx 0.12\ \Omega$ in the YBCO single crystal (Figure 3.10), we derive $\rho(T_c) \approx 38\ \mu\Omega$ cm [193]. All the functions of temperature $R_s(T) = X_s(T)$ plotted in Figsures 3.10–3.12 in the region $T \geq T_c$ are adequately described by the formula $2R_s^2(T)/\omega\mu_0 = \rho(T) = \rho_0 + bT$. For example, in the BSCCO crystal (Figure 3.11) $\rho_0 \approx 13\ \mu\Omega$ cm, $b \approx 0.3\ \mu\Omega$ cm/K [175].

The normal skin-effect condition, $R_s(T) = X_s(T)$ at $T \geq T_c$, was also proved by measurements of the surface impedance in the ab-plane of different YBCO [7, 180, 193, 182, 110] and BSCCO [180, 97, 175, 182] single crystals. The issue of the temperature dependence of the impedance of TBCO [209, 75] crystals raises controversy. The problem is that, even if curves of $R_s(T)$ are matched to curves of $\Delta X_s(T)$ in the range $T \geq T_c$, the change in the reactance $\Delta X_s(T)$ in the superconducting region is larger than the change $\Delta R_s(T)$, so that we obtain negative values of $X_s(0)$. It is also complicated by the circumstance that the coefficients of thermal expansion for TBCO cannot be found in literature. If we assume that the thermal expansion coefficient of TBCO in the range $T > T_c$ equals that of BSCCO [143] or TBCCO [80] and take into account the frequency shift $\Delta f_l(T)$ in (3.39), the curves

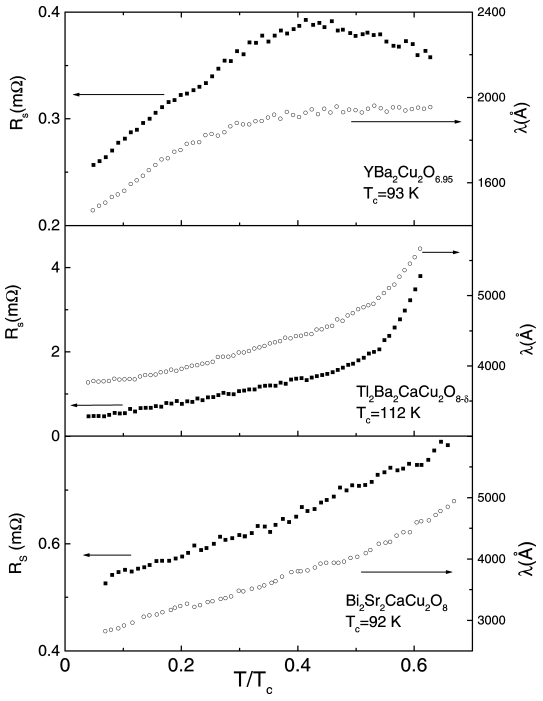

Figure 3.13 Surface resistance R_s and penetration depth λ_{ab} in YBCO, TBCCO, and BSCCO single crystals as functions of temperature for $T < 0.7T_c$.

of $R_s(T)$ and $X_s(T)$ for TBCO are parallel to one another in the normal state. But the attempt to bring these curves to coincidence so as to satisfy the condition of normal skin effect leads to the value $X_s(0) = \omega\mu_0\lambda_{ab}(0) < 0$. Thus, the problem can be solved by either discovering the cause of the negative contribution $dX_s < 0$ in the range $T < T_c$, which should be subtracted from the measurements of $\Delta X_s(T)$ to obtain true values of the reactance, $X_s(T) > 0$, which equals $R_s(T)$ at $T > T_c$, or explaining the positive difference $X_s(T) - R_s(T)$ in the normal state of TBCO at which a reasonable value of $X_s(0)$ is obtained [191].

3.4.1.2 Surface Impedance in the Superconducting State

It is more convenient to compare the surface impedance versus temperature, $Z_s(T)$, in the superconducting state in different HTS single crystals by dividing the entire temperature interval into three sections, namely the ranges of low ($T < T_c/3$), intermediate ($T \sim T_c/2$), and subcritical ($T \sim T_c$) temperatures.

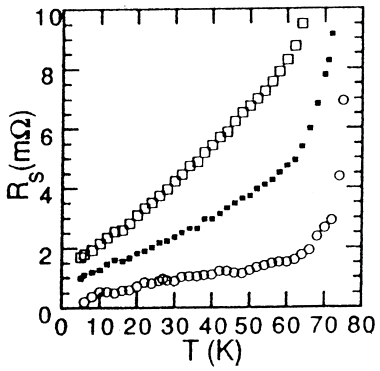

Figure 3.14 Surface resistance R_s of a TBCO single crystal ($T_c \approx 78$ K) versus temperature [35] at several frequencies: circles correspond to 14.4 GHz, black squares to 24.8 GHz, open squares to 35.9 GHz.

Low Temperatures, $T < T_c/3$

Figure 3.13 shows a set of typical $R_s(T)$ and $\lambda(T)$ curves in the range $T < 0.7T_c$ measured at ISSP in YBCO [193], BSCCO [175], and TBCCO [217] crystals. These curves correspond to the low-temperature sections of the graphs in Figures 3.10–3.12 with the ordinate plotted using a linear scale.

In the low-temperature range, changes in the surface resistance $\Delta R_s(T) \propto T$ for all crystals whose data are plotted in Figure 3.13. A similar linear dependences $\Delta R_s(T)$ are observed in YBCO [32, 104, 134, 98, 180, 193, 185, 217, 186, 195, 103, 91], BSCCO [180, 97, 122, 175], and TBCO [35] (Figure 3.14) single crystals, when the microwave frequencies do not exceed about 30 GHz. For vanishing temperature, $R_s(T)$ extrapolates to a finite residual surface resistance $R_{\rm res}$. Its magnitude, even in samples of the highest quality, is a factor of several tens higher than $R_{\rm res}$ of conventional superconductors. At present, extremely low values of $R_{\rm res} \sim 50$ $\mu\Omega$ at frequencies ~ 10 GHz have been observed in YBCO single crystals [180, 185, 91].

The functions $\Delta\lambda(T) = \Delta X_s(T)/\omega\mu_0$ in YBCO, BSCCO (Figure 3.13), and TBCO (Figure 3.15) crystals in the range $T < T_c/3$ are also linear. The curve of $\lambda(T)$ for TBCCO at $T > 12$ K shown in Figure 3.13 has clearly rectilinear shape. It is important to notice the different slopes of the $\Delta\lambda(T) \propto T$ curves for $T \ll T_c$. In particular, in YBCO crystals fabricated by different techniques the slopes can differ almost an order of magnitude [180, 193, 185, 103]. The reasons for such discrepancy is still unclear.

The extrapolation of low-temperature sections of $\lambda(T)$ curves to $T = 0$ K in Figure 3.13 yields the following estimates of $\lambda_{ab}(0)$ in several single crystals of different materials: 1400 Å (YBCO), 3700 Å (TBCCO), and 2600 Å (BSCCO).

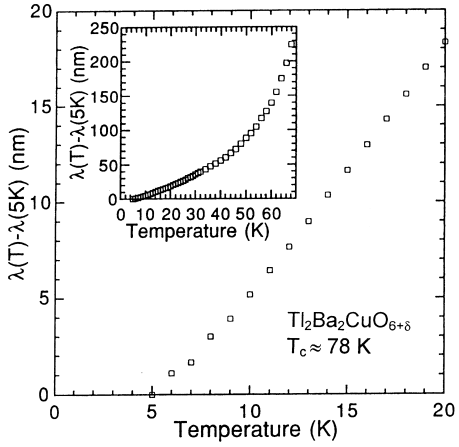

Figure 3.15 Linear section of the curve of field penetration depth λ_{ab} versus temperature in a TBCO single crystal [35]. The inset shows the curve of $\Delta\lambda(T)$ over a wider temperature range.

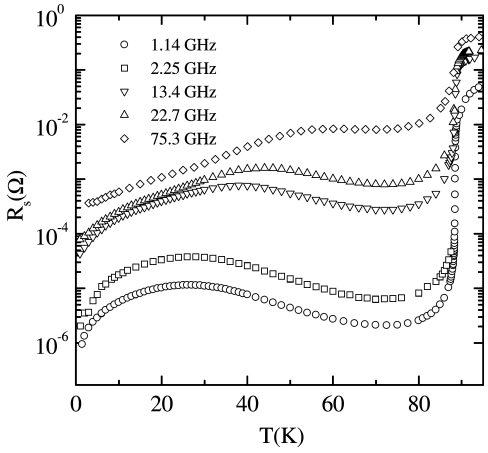

Figure 3.16 Surface resistance $R_s(T)$ in a high purity YBCO single crystal at different frequencies from [91].

Intermediate Temperatures, $T \sim T_c/2$

At frequencies of about 10 GHz, the linear dependence $\Delta R_s(T) \propto T$ in BSCCO, TBCCO (Figure 3.13), and TBCO (Figure 3.14) single crystals extends to temperatures $\sim T_c/2$. The magnetic field penetration depth $\lambda(T)$ monotonically increases with the temperature.

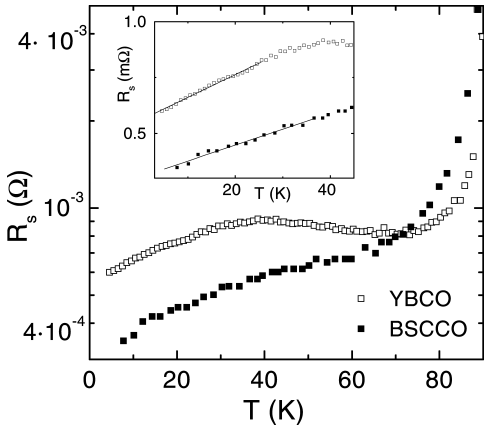

Figure 3.17 Comparison of the temperature dependences of the surface resistance $R_s(T)$ of BSCCO and YBCO single crystals at 14.4 GHz. Experimental data are taken from [122] (BSCCO at 14.4 GHz) and [193] (YBCO at 9.4 GHz, scaled by ω^2 to 14.4 GHz). The inset shows the linear T-dependences of R_s at low T for both materials and a broad peak of $R_s(T)$ for YBCO.

This property of the surface impedance, common for all HTS single crystals with the tetragonal structure, is not characteristic of YBCO. As was noted previously, all microwave measurements of high-quality YBCO crystals show a broad peak in the $R_s(T)$ curve centred at about 30–40 K at frequencies ~ 10 GHz. The peak shifts up in temperature and diminishes in size as the measurement frequency is increased (Figure 3.16). In YBCO single crystals of higher quality the amplitude of the peak rises and $R_s(T)$ reaches its maximum at a lower temperature [91].

The underlying cause of this YBCO feature, which distinguishes it from other HTS materials, has remained unclear. The simplest idea that the absence of this peak in crystals with the tetragonal structure might be caused by their poor quality, as is the case in YBCO doped with Zn [7, 216, 32], looks unlikely because, firstly, there is a sufficiently large set of experimental data indicating that $R_s(T)$ is a linear function in BSCCO, TBCO, and TBCCO, and secondly, the peak in $R_s(T)$ was also detected in such YBCO crystals [98, 217, 110] whose parameters $R_{\rm res}$ and $\rho(T_c)$, characterizing their quality, were inferior compared to those of, e.g., BSCCO [122]. Results for the latter crystals are shown in Figure 3.17. The more probable cause of the peak is the presence of an additional component in the YBCO orthorhombic structure, namely Cu–O chains, which leads to a mixed $(d + s)$-symmetry of the order parameter in YBCO. The electrons of the chains form an additional band, contributing to the observed dependence $Z_s(T)$. This contribution seems to result in another distinctive feature of YBCO, namely the plateau (Figure 3.13) or bump (Figure 3.18) on the curve of $\lambda_{ab}(T)$.

This feature has been observed in the purest YBCO single crystals [193, 185, 217, 186, 195] and films [84, 112]. Curve 1 in Figure 3.18 refers to an YBCO

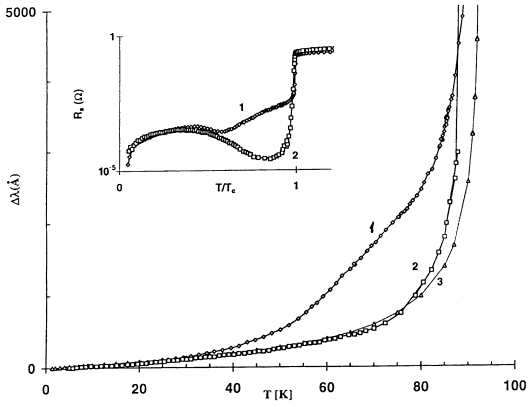

Figure 3.18 Magnetic field penetration depth $\Delta\lambda_{ab}$ as a function of temperature for YBCO single crystals [185] manufactured using different techniques: (1) in $BaZrO_3$ crucibles; (2) in ZrO_2 yttrium stabilized crucibles; (3) data from [78]. The inset shows curves of surface resistance $R_s(T/T_c)$ for samples 1 and 2.

crystal with notably smaller values of $\rho(T_c)$ and $R_{\rm res}$ than in samples 2 and 3, whose $\Delta\lambda_{ab}(T)$ curves have a standard shape. In Figsures 3.10 and 3.13 the quantities X_s and λ_{ab} in a YBCO single crystal are almost constant with the temperature in the intermediate range.

However, the recent measurements of $\Delta\lambda_{ab}(T)$ in a high purity $BaZrO_3$-grown YBCO crystal [103] show no such features in the intermediate temperature range. The authors of [103] argue that the disagreement with the results of [185] arises from some sort of problems with the surfaces of the crystals. However that may be, the problem is still open.

In discussing features of the imaginary part $X_s(T)$ of the surface impedance in the intermediate temperature range, one should be careful, taking into account the possibility of the crystal thermal expansion distorting curves of $\lambda(T)$. As was shown in the previous section, this process has little effect on the shapes of $\lambda(T)$ curves at $T < 40$ K. The observed in [193, 217] plateaux on the $\lambda_{ab}(T)$ curves have approximately the same width of about 20 K, but their positions with respect to $T_c/2$ vary in several YBCO single crystals manufactured by the same technique [193]. Measurements on one of these crystals were performed at the laboratory under Sridhar's direction (NEU), and they confirmed the existence of a plateau. Hence, we can assert that the plateaux on the curves of $\lambda(T)$ [193, 217] are real features of the surface reactance $X_s(T)$, characteristic of YBCO single crystals fabricated at ISSP. On the other hand, the curves of surface resistance $R_s(T)$ obtained in the same experiments [193, 217] have the usual shape (Figure 3.10).

Finally, another feature in the impedance of high-quality YBCO crystals, namely a notable increase in $R_s(T)$ with temperature beyond the peak at $T \sim 40$ K, was detected in the experiments of NEU-group [185, 186]. The corresponding curve

of $R_s(T)$ [185] is shown in the inset to Figure 3.18 (curve 1). The surface resistance as a function of temperature is easily derived from measurements of the cavity Q using (3.39). This function is not affected by the sample thermal expansion. The gradual increase in $R_s(T)$ in the interval $T_c/2 < T < T_c$ can be hardly attributed to coexistence of different phases in the sample. The emergence of a superconducting phase with a certain T_c is indicated in microwave experiments by a jump (an abrupt drop) in $R_s(T)$ at the critical temperature, which was observed, for example in a TBCCO crystal (Figure 3.12), which has two superconducting phases [183], namely 2212 ($T_{c1} \simeq 112$ K) and 1212 ($T_{c2} \simeq 81$ K). YBCO single crystals grown using $BaZrO_3$ crucibles and measured at a frequency of 10 GHz [185, 186] are samples of high purity and curve 1 in the inset to Figure 3.18 proved to be reproducible [186, 188].

Temperatures Close to T_c, $T \to T_c$

In all HTS single crystals, the surface resistance $R_s(T)$ drops abruptly at the point of transition from the normal to superconducting state. At frequencies of about 10 GHz, $R_s(T)$ of high-quality YBCO crystals falls off by a factor of one hundred or more as the temperature drops to one degree below T_c. The quantity $X_s(T)$ also jumps at the transition point, but by a smaller factor. Opinions differ about the temperature dependence of the magnetic field penetration depth $\lambda_{ab}(T)$ around the critical point, which has been investigated in YBCO crystals of high quality fabricated by different techniques. Some authors [104, 103, 16] measured the function $\lambda_{ab}(T) \propto (1-T/T_c)^{-0.33}$, corresponding to the so-called 3D XY fluctuation model [128, 60, 170]. Others [186] detected in the neighbourhood of T_c the dependence $\lambda_{ab}(T) \propto (1-T/T_c)^{-0.5}$, in agreement with the BCS theory. The exponent measured in the crystals fabricated at ISSP proved to have an intermediate value between -0.33 and -0.5.

The main peculiarities of the temperature dependences of the surface impedance in different HTS single crystals are summarized in Table 3.1.

3.4.2 Complex Conductivity

Now let us discuss the temperature dependence of the complex conductivity $\sigma_s = \sigma_1 - i\sigma_2$. The components $\sigma_1(T)$ and $\sigma_2(T)$ are not measured directly but derived from measurements of $R_s(T)$ and $X_s(T)$ using (3.14).

At temperatures not very close to T_c and in HTS crystals of high quality $R_s(T) \ll X_s(T)$, and (3.14) can be simplified:

$$\sigma_1(T) = \frac{2\omega\mu_0 R_s(T)}{X_s^3(T)}, \quad \sigma_2(T) = \frac{\omega\mu_0}{X_s^2(T)}. \tag{3.44}$$

Table 3.1 Surface impedance $Z_s(T) = R_s(T) + iX_s(T)$ in the ab-plane of high-T_c single crystals at frequencies ~ 10 GHz.

HTS	Superconducting state, $T < T_c$			Normal state $1.5T_c > T \geq T_c$
	Low temperatures 4 K$< T \ll T_c$	Intermediate temperatures $T \sim T_c/2$	$T \to T_c$	
Orthorhombic structure YBCO $T_c \approx 92\ K$	$\Delta R_s(T) \propto T$, $\Delta X_s(T) \propto T$ at $T \lesssim T_c/4$; Essentially different slopes of $\Delta\lambda(T) \propto T$ [78, 7, 216, 32, 104, 134, 98, 180, 193, 185, 217, 186, 195, 103, 91]	Broad peak in $R_s(T)$ at $25 < T < 45$ K [32, 104, 134, 98, 180, 193, 185, 217, 186, 195, 103, 91, 30, 182, 33, 110] Peculiarities: 1. Shoulder [185, 186, 31] in $R_s(T)$ at $T > 40$ K; 2. Bump [185, 188] or plateau [193, 217, 195] on the curves of $X_s(T)$ at $50 < T < 80$ K	Different slopes of $\lambda(T)$ [216, 32, 104, 134, 98, 180, 193, 185, 217, 186, 195, 103, 91]	Normal skin-effect
Tetragonal structure BSCCO $T_c \approx 90$ K [180, 97, 179, 122, 175]	$\Delta R_s(T) \propto T, T \lesssim T_c/2$		Rapid growth of $R_s(T)$ and $X_s(T)$	$R_s(T) = X_s(T) = \sqrt{\omega\mu_0\rho(T)/2}$ $\Delta\rho(T) \propto T$
TBCCO $T_c \approx 110$ K [217, 195]	$\Delta X_s(T) = \omega\mu_0\Delta\lambda(T) \propto T, T \lesssim T_c/3$			
TBCO $T_c \approx 80$ K [35, 209]				$X_s(T) > R_s(T)$?

It follows from (3.44) that in the ranges of low and intermediate temperatures $\sigma_1/\sigma_2 = 2R_s/X_s \ll 1$. The increments $\Delta\sigma_1(T)$ and $\Delta\sigma_2(T)$ depend on relative changes $\Delta R_s(T)$ and $\Delta X_s(T)$:

$$\Delta\sigma_1 \propto \left(\frac{\Delta R_s}{R_s} - 3\frac{\Delta X_s}{X_s}\right), \quad \Delta\sigma_2 \propto -\frac{\Delta X_s}{X_s}. \tag{3.45}$$

Hence, the curves of $\sigma_2(T)$ are determined only by the function $X_s(T) = \omega\mu_0\lambda(T)$ and reflect the basic properties of the field penetration depth versus temperature, namely its rectilinear shape at low temperatures in all high-quality HTS crystals and the features detected in YBCO in the intermediate temperature range.

The behaviour of the real part $\sigma_1(T)$ of the conductivity, as follows from (3.45), is determined by the competition between relative increments $\Delta R_s/R_s$ and $\Delta X_s/X_s$.

In conventional superconductors like Nb, $X_s(T)$ ($\gg R_s$) is a very weak function of temperature in the temperature range $T \leq T_c/2$ ($\Delta X_s \approx 0$), and $R_s(T)$ drops exponentially with decreasing temperature, approaching the constant level of the residual surface resistance $R_{\rm res}$ as $T \to 0$. By subtracting $R_{\rm res}$ from the measurements of $R_s(T)$, we derive, using (3.44), the temperature dependence $\sigma_1(T)$ predicted by the BCS model: $\sigma_1 = 0$ at $T = 0$ and shows an exponentially slow growth with temperature for $T \leq T_c/2$ (Figures 3.2, 3.3). The extremely small $R_{\rm res}$ and R_s in (3.45) indicate that the increment $\Delta\sigma_1(T)$ in classical superconductors is always positive, $\Delta\sigma_1(T) > 0$, at least in the temperature interval $T < 0.8T_c$, before the maximum of the BCS coherent peak is reached.

For HTS single crystals the dependences $\sigma_1(T)$ are radically different from those predicted by conventional theories (BCS, SC, GC) of the microwave response of superconductors. In the range $T < T_c$ the increments $\Delta R_s(T)$ and $\Delta X_s(T)$ in HTS are not small, and in addition, $\Delta X_s(T) \gg \Delta R_s(T)$. Although $R_s(T) < X_s(T)$, $\Delta R_s/R_s$ is not necessarily greater than $3\Delta X_s/X_s$ in (3.45) or positive at all temperatures. When that occurs, $\sigma_1(T)$ increases with decreasing temperature. The function $\sigma_1(T)$ is maximum at some $T = T_{\rm max}$, and then $\sigma_1(T)$ becomes smaller with decreasing temperature. $\sigma_1(T)$ has a peak if the value of $R_{\rm res}$ is sufficiently small as $T \to 0$,

$$R_{\rm res} < \frac{X_s(0)}{3}\frac{\Delta R_s(T)}{\Delta X_s(T)}\bigg|_{T\to 0}. \tag{3.46}$$

If the right-hand side of (3.46) is deemed constant, the peak position $T_{\rm max}$ should shift to the low side down to $T = 0$ with the increase in $R_{\rm res}$. If inequality (3.46) fails, the function $\sigma_1(T)$ in HTS materials, unlike conventional superconductors, should not rise but drop monotonically as the temperature rises from $T = 0$.

Thus, the shape of the $\sigma_1(T)$ curve for $T \ll T_c$ depends on the choice of the residual surface resistance $R_{\rm res}$, whose origin and accurate value are unknown. For this reason, the shapes of $\sigma_1(T)$ curves are not determined unambiguously for $T \leq T_c/2$, unlike the functions $R_s(T)$ and $X_s(T)$, which are directly measured in experiments.

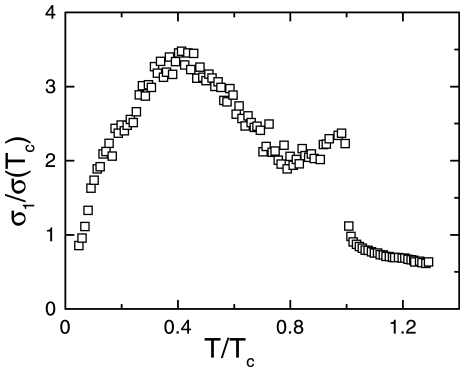

Figure 3.19 Real part of the conductivity $\sigma_1(T)/\sigma(T_c)$ of a YBCO single crystal calculated by (3.16). Values of $R_s(T)$ substituted in this equation were derived from curves of Figure 3.10 (or 3.13) by subtracting the residual resistance $R_{\rm res} \simeq 230\ \mu\Omega$.

If we linearly extrapolate $R_s(T)$ to the region $T \ll T_c$ down to $T = 0$ and attribute the resulting $R_s(0)$ to the residual surface resistance, $R_s(0) = R_{\rm res}$ (by analogy with conventional superconductors), and then substitute the temperature dependent difference $R_s(T) - R_{\rm res}$ in the numerator of the first formula in (3.44), all resulting $\sigma_1(T)$ curves for HTS materials have shapes of broad peaks. Starting with a steep linear section in the neighborhood of $\sigma_1(0) = 0$, the curve of $\sigma_1(T)$ rapidly arrives at its peak value $\sigma_1(T_{\rm max})$, which is always higher than the normal state conductivity $\sigma(T_c)$: $\sigma_1(T_{\rm max}) > \sigma(T_c)$. An example of a $\sigma_1(T)/\sigma(T_c)$ curve for a YBCO single crystal derived from measurements of $Z_s(T)$ plotted in Figure 3.10 by using (3.14) and subtracting $R_{\rm res} \simeq 230\ \mu\Omega$ is given in Figure 3.19. This procedure, however, completely ignores the possibility of intrinsic residual losses. Therefore, some authors (see, e.g., Refs. [91, 122, 33, 81]) associate residual losses in HTS single crystals with a residual normal electron fluid. This implies that the source of the residual loss is in the bulk of the sample, although it is probably not intrinsic. If this contribution is excluded from the complex conductivity, one obtains $\sigma_1(T = 0) \to 0$, as can be seen in Figure 3.20 for the measurements taken at 13, 23, and 75 GHz [91]. The peak of $\sigma_1(T)$ shifts to higher temperatures and diminishes in size as the experimental frequency is increased. In YBCO single crystals, the temperature $T_{\rm max}$ of the maximum of $\sigma_1(T)$ occurs close to the temperature at which the peak of $R_s(T)$ occurs.

Finally, one can directly derive function $\sigma_1(T)$ from measurements of $R_s(T)$ and $X_s(T)$ without any concern about $R_{\rm res}$. In this case, $\sigma_1(0)$ is not determined uniquely, and whether $\sigma_1(T)$ has a peak depends on the validity of condition (3.46). Curves of $\sigma_1(T)$ obtained using (3.14) without subtracting any residual losses are plotted in the following graphs: two upper curves in Figure 3.20 shows data obtained at 1.14 and 2.25 GHz [91]; Figure 3.21 plots curves $\sigma_1(T)$ for YBCO crystals characterized by the experimental curves 1 and 2 shown in Figure 3.18 [185]; Figure 3.22

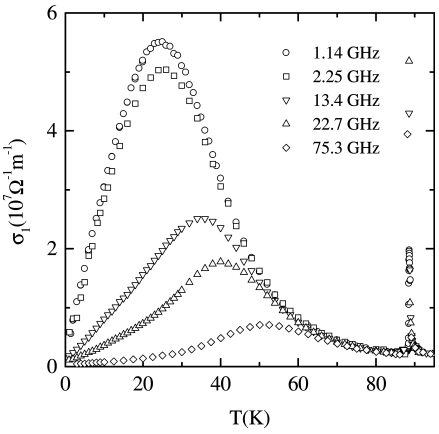

Figure 3.20 Real part of the conductivity $\sigma_1(T)$ of YBCO single crystal extracted from the surface resistance measurements of Figure 3.16 at different frequencies [91].

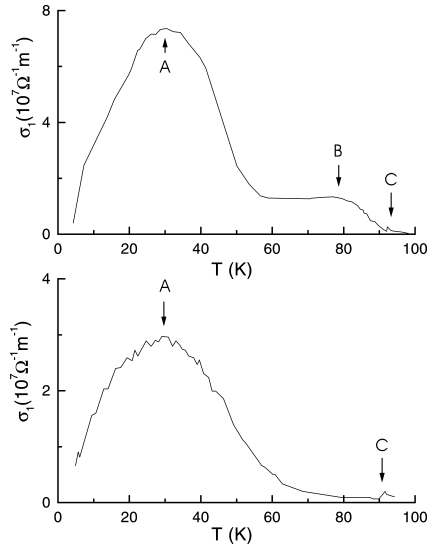

Figure 3.21 Temperature dependences of the conductivity σ_1 of optimally doped YBCO single crystals grown in $BaZrO_3$ (top) and yttria-stabilized zirconica (bottom) crucibles. The data are extracted from the measurements of Figure 3.18. The sharp peak C present in both cases. Note the appearance of a new peak B in YBCO $BaZrO_3$ grown crystal [185].

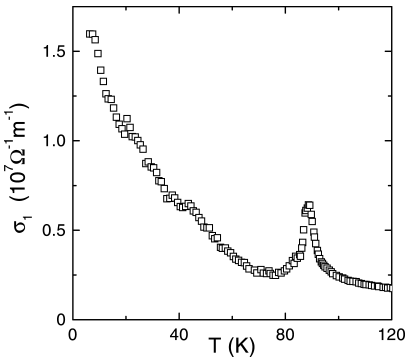

Figure 3.22 Conductivity $\sigma_1(T)$ of BSCCO single crystal extracted from the surface impedance measurements of Figure 3.11. A low temperature broad peak is absent.

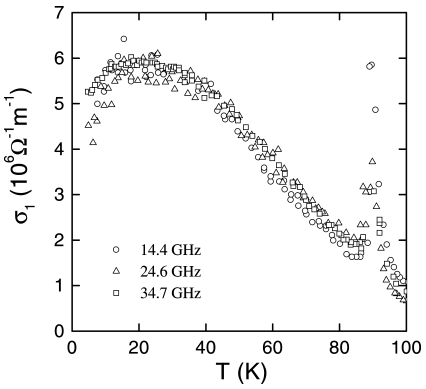

Figure 3.23 Real part of conductivity $\sigma_1(T)$ in BSCCO single crystal at different frequencies exhibits a broad peak at low temperature [122].

shows the dependence $\sigma_1(T)$ for BSCCO derived from the surface impedance measurements given in Figure 3.11; Figure 3.23 plots the real parts of the conductivity in BSCCO single crystal at different frequencies taken from [122].

Figures 3.22 and 3.23 show two possible shapes of $\sigma_1(T)$ curves in BSCCO single crystals, namely, the presence of the peak in Figure 3.23 ($R_{\rm res} \approx 300\ \mu\Omega$ at 14.4 GHz from Figure 3.17; see also Figure 3.28 below) and its absence in Figure 3.22 ($R_{\rm res} \approx 500\ \mu\Omega$ at 9.4 GHz from Figure 3.11). The higher the crystal quality, the more clearly the peak in the conductivity at $T < T_c$ can be seen. Two upper curves in Figure 3.20 correspond to the characteristic $R_s(T)$ of the YBCO crystal with $R_{\rm res} \sim 1\ \mu\Omega$ at a frequency ~ 1 GHz (Figure 3.16). Near $T = 0$, $\sigma_1(T)$

increases linearly with T and reaches its peak value at $T_{\max}$, $\sigma_1(T_{\max})$, which is higher than the normal state conductivity $\sigma(T_c)$.

It is clear from Figures 3.19 and 3.21 that the features of the YBCO surface impedance $Z_s(T)$ in the intermediate temperature range also manifest in the conductivity $\sigma_1(T)$ of these samples. In particular, a new conductivity peak (labeled *B* in Figure 3.21) around 80 K in YBCO crystal grown in $BaZrO_3$ crucible is correlated with the features of the impedance $Z_s(T)$ at $T > T_c/2$ (Figure 3.18).

Let us also discuss the behaviour of $\sigma_s(T)$ near T_c, where (3.44) and (3.45) do not apply. In this temperature range, it is necessary to use the general local relations (3.11–3.14) or their analogues for normalized quantities (3.15) and (3.16).

The conductivity $\sigma_2(T)$ in the ab-plane of HTS crystals abruptly drops to very small values in the normal state. The derivative $(T_c/\sigma_2(0))\,\mathrm{d}\sigma_2(T)/\,\mathrm{d}T$ at $T = T_c$, defining the slope of $\lambda(0)^2/\lambda(T)^2$ curves at $T = T_c$, varies between -2 and -4 in different crystals.

The real part of the conductivity, $\sigma_1(T)$, does not show a coherence peak (Figures 3.2, 3.3) about $0.85T_c$ predicted by BCS. Usually the curve of $\sigma_1(T)$ of HTS single crystals in the neighbourhood of T_c has the shape of a narrow peak (see Figures 3.4, 3.20–3.23) which becomes higher with decreasing frequency (Figure 3.23). The peak width virtually coincides with the width of the phase transition from the normal to superconducting state on the curve $R_s(T)$, and transforms to a broad maximum peaking at $T < T_c/2$. A possible explanation of the sharp peak just below T_c is fluctuation effects [209, 16, 93] or inhomogeneous broadening of the superconducting transition [71, 67, 153, 197].

3.5 MODIFIED TWO-FLUID MODEL

As was noted in the first two sections of this review, none of the models briefly described there (GC, BCS, and SC) can account for the impedance $Z_s(T)$ and conductivity $\sigma_s(T)$ as functions of temperature in the ranges of low and intermediate temperatures. At the same time, as was shown in [66, 131], high T_c values ($T_c \sim 100$ K), the temperature dependence of the resistivity, the frequency dependence of the momentum relaxation time, and other properties of the normal state in optimally doped HTS's are well described within the framework of the Fermi-liquid approach involving strong electron–phonon coupling [50]. In particular, the curves of $\lambda^2(0)/\lambda^2(T)$ numerically calculated by the SC model [144, 40, 167, 14] proved to be fairly close to the function $n_s(t)/n = 1 - n_n(t)/n = 1 - t^4$ in the GC model. The slopes of these curves at $T = T_c$ are in agreement with those measured in different YBCO single crystals and equal to -3 [32] or -4 [134, 193, 217]. In combination with the experimental fact that there is no BCS coherent peak in the conductivity of HTS crystals, this indicates the necessity of taking into account effects of strong coupling near T_c and the feasibility of interpreting of HTS properties at microwave frequencies in terms of a two-fluid model.

A modified two-fluid model has been proposed independently in [194, 56] and then further developed in [193, 217, 195, 196, 190, 191, 197, 58, 57, 59]. This phe-

nomenological model has two essential features that make it different from the GC model [73]. The first is the introduction of the temperature dependence of the quasiparticle relaxation time $\tau(t)$ (with $t \equiv T/T_c$), and the second feature is the unique density of superconducting electrons $n_s(t)$, which gives rise to a linear temperature dependence of the penetration depth in the ab-plane at low temperatures,

$$\frac{\lambda^2(0)}{\lambda^2(t)} = \frac{n_s(t)}{n} \simeq (1 - \alpha t), \tag{3.47}$$

where α is a numerical parameter.

3.5.1 Scattering and Surface Resistance of HTS Single Crystals

The first attempts to determine the temperature dependence $\tau(T)$ by comparing measurements of $\sigma_1(T)$ and $\sigma_2(T)$ with calculations by (3.8) were undertaken in studying HTS crystals in which the real part of conductivity had a peak at $T \sim T_c/2$ [30, 182, 33]. The conclusion from this comparison was that τ should increase with decreasing temperature in the range $T < T_c$, but for various reasons (poor quality of crystals, utilization of curves measured in different experiments etc.) the resulting functions $\tau(T)$ were rather peculiar: $1/\tau \propto \exp(T/T_0)$, $T_0 \sim 10$ K [33] or $1/\tau \propto (AT^6 + B)$ [182]. A more detailed analysis was required taking into account both common properties and specific features of the impedance and conductivity of high-quality HTS crystals.

For $\omega\tau(T_c) \ll 1$, which is normally satisfied at microwave frequencies in HTS's, the parameter $\omega\tau(T_c)$ is obtained from measurements of $R_s(T_c)$ and $X_s(0)$,

$$\omega\tau(T_c) = \frac{X_s^2(0)}{2R_s^2(T_c)} = \frac{\sigma_1(T_c)}{\sigma_2(0)}. \tag{3.48}$$

At frequencies ~ 10 GHz, the value of $\omega\tau$ for the best HTS crystals is of the order of 10^{-3} at $T = T_c$ and remains less than unity at all temperatures $T < T_c$, as is discussed in what follows. In the two-fluid model, therefore, the expressions of the conductivity components in (3.8) turn into the simple form (3.9). At fixed $n_s(t)/n$, hence $n_n(t)/n = 1 - n_s(t)/n$, the only function we lack for determination of conductivity $\sigma_1(t)$ in (3.9) and impedance $Z_s(t)$ in (3.11) is $\tau(t)$.

3.5.1.1 Temperature Dependence of the Relaxation Time

First let us try to describe measurements of $R_s(T)/R_s(T_c)$ in YBCO single crystals using (3.15) by substituting values of $\sigma_2(T)/\sigma_2(0) = \lambda^2(0)/\lambda^2(T) = n_s(T)/n$ measured in the same experiments and $\sigma_1(T)/\sigma_1(T_c)$ obtained using (3.9); the latter function, in its turn, being derived from $n_n(T)/n = 1 - \sigma_2(T)/\sigma_2(0)$, which is obtained using experimental data and properly selected $\tau(T)$.

In selecting the form of function $\tau(T)$, let us rely on the analogy between the 'normal fluid' component in the superconducting state and charge carriers in a normal metal. According to Mathissen's rule, the reciprocal relaxation time at temperatures below the Debye temperature Θ is

$$\frac{1}{\tau} = \frac{1}{\tau_{\rm imp}} + \frac{1}{\tau_{\rm e-ph}}. \tag{3.49}$$

The first term on the right-hand side is due to impurity scattering and is independent of temperature, and the second is due to the electron–phonon scattering and is proportional to T^5.

From (3.49), we express $\tau(T)$ as

$$\frac{1}{\tau(t)} = \frac{1}{\tau(0)}\left[1 + \frac{t^5}{\beta}\right], \tag{3.50}$$

where β is a numerical parameter, which equals, as it follows from (3.50),

$$\beta = \frac{\tau(T_c)}{\tau(0) - \tau(T_c)}. \tag{3.51}$$

Following the formal analogy with metals, one can say that the parameter β is characteristic of the 'HTS purity': $\beta \approx \tau(T_c)/\tau(0) \ll 1$ if $\tau(0) \gg \tau(T_c)$. The value of $\tau(0)$ is found from the slopes $\mathrm{d}R_s/\,\mathrm{d}T$ and $\mathrm{d}X_s/\,\mathrm{d}T$ of the experimental data of $R_s(T)$ and $X_s(T)$ as $T \to 0$ ($\omega\tau(0) < 1$),

$$\omega\tau(0) = \left.\frac{\mathrm{d}R_s}{dX_s}\right|_{T\to 0}. \tag{3.52}$$

With (3.48) and (3.52), the parameter β is determined from the surface impedance data [197].

Expression (3.50) corresponds to the low-temperature limit of the Bloch–Grüneisen formula, which includes the impurity scattering and can be presented in a wide temperature range in the form

$$\frac{1}{\tau} = \frac{1}{\tau(0)}\left[1 + \frac{t^5\mathcal{J}_5(\kappa/t)/\mathcal{J}_5(\kappa)}{\beta}\right], \quad \mathcal{J}_5(\kappa/t) = \int\limits_0^{\kappa/t} \frac{z^5 e^z\,\mathrm{d}z}{(e^z-1)^2}, \tag{3.53}$$

where $\kappa = \Theta/T_c$. The parameter of HTS corresponding to Θ can be estimated as several hundreds of degrees. At $T < \Theta/10$ ($\kappa > 10t$) the second summand in the brackets on the right of (3.53) is proportional to T^5; in the region $T > \Theta/5$ ($\kappa < 5t$) it is proportional to T. Thus, if $\beta < 1$ the reciprocal relaxation time (the electron relaxation rate) is constant and equal to $1/\tau(0)$ over the interval $0 < T < T_c/3$, and at higher temperatures it increases gradually, starting as the power function $\propto T^5$ in the region $T < T_c/2$ and switching to $\propto T$ around T_c, and at $T > T_c$ we have a linear dependence $\Delta\rho_{ab}(T) \propto 1/\tau(T) \propto T$. Examples of $1/\tau(t)$ for different parameters of β, κ, and $\tau(T_c)$ are shown in Figure 3.24.

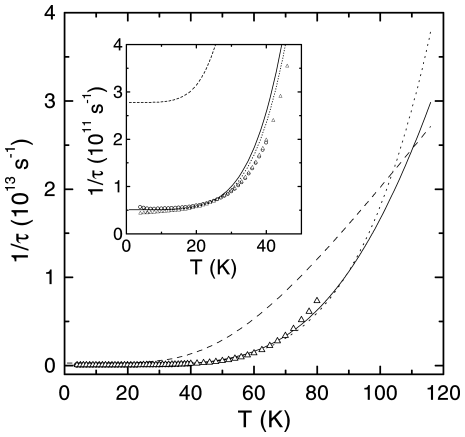

Figure 3.24 Scattering rate of quasi-particles calculated from (3.50), dotted line: $\beta = 0.005$, and (3.53), solid line: $\beta = 0.005$, $\kappa = 9$; dashed line: $\beta = 0.02$, $\kappa = 4$. The triangles are calculated from $1/\tau = [1-\lambda^2(0)/\lambda^2(T)]/[\mu_o\sigma_1(T)\lambda^2(0)]$, with $\sigma_1(T)$ and $\lambda(T)$ at 1.14 GHz and $\lambda(0) = 1600$ Å in the ab-plane, with the currents parallel to the a-direction of the YBCO crystal [91]. The inset shows the low-temperature parts of the curves. The circles are from Figure 3.8 of [91].

Even though the chosen form of the function $\tau(T)$ for HTS materials with complex electronic spectra was over-simplified, it turned out that all experimental curves of $R_s(T)$ in high-quality YBCO single crystals for both $T < T_c$ and $T > T_c$ can be described by the modified two-fluid model with $\tau(T)$ given by (3.50) without any fitting parameters or by (3.53) with only one parameter κ. This is demonstrated by Figure 3.25, which contains measurements labeled by A, B, and C taken from [32, 193, 185] and transformed to a single frequency of 10 GHz. Graph B corresponds to the curve of $R_s(T)$ in Figure 3.10 and graph C to curve 1 in the inset to Figure 3.18. At this frequency, according to (3.48), $\omega\tau(T_c) \approx 4 \times 10^{-3}$, i.e., in these experiments [32, 193, 185] $1/\tau(T_c) \approx 2 \times 10^{13}$ s^{-1}. The solid lines in Figure 3.25 show calculations of $R_s(T)/R_s(T_c)$ by (3.9) and (3.15) with $\sigma_2(T)/\sigma_2(0)$ derived from the same experimental data [32, 193, 185] and plotted in Figure 3.33 (curves A–C) represented below. Curve A in Figure 3.25 was plotted using (3.50) with $\beta = 0.01$ in (3.51), estimated from (3.48) and (3.52). For curve B $\beta = 0.1$ in (3.50), and for curve C $\beta = 0.02$ and $\kappa = 4$ in (3.53).

Setting $\beta = 0.005$ and $\kappa = 9$ in (3.53) and taking the experimental values $\sigma_2(T)/\sigma_2(0)$ from Figure 3.31 (see below) and $\omega\tau(T_c) = 7.5 \times 10^{-4}$ at 1.14 GHz, we find from (3.9) and (3.12) the T-dependence of $R_s(T)$, shown by the solid lines in Figure 3.26. These curves match the data of [91] over the entire temperature range. The same result is obtained using (3.50) instead of (3.53), with $\beta = 0.005$. For $\kappa \gg 1$ and $T \lesssim T_c$, (3.50) and (3.53) are identical.

It follows from (3.17) and (3.9) that for $\alpha t \ll 1$ (see (3.47)), a rough estimate of the temperature t_m at which $R_s(T)$ is maximum is obtained from the relation

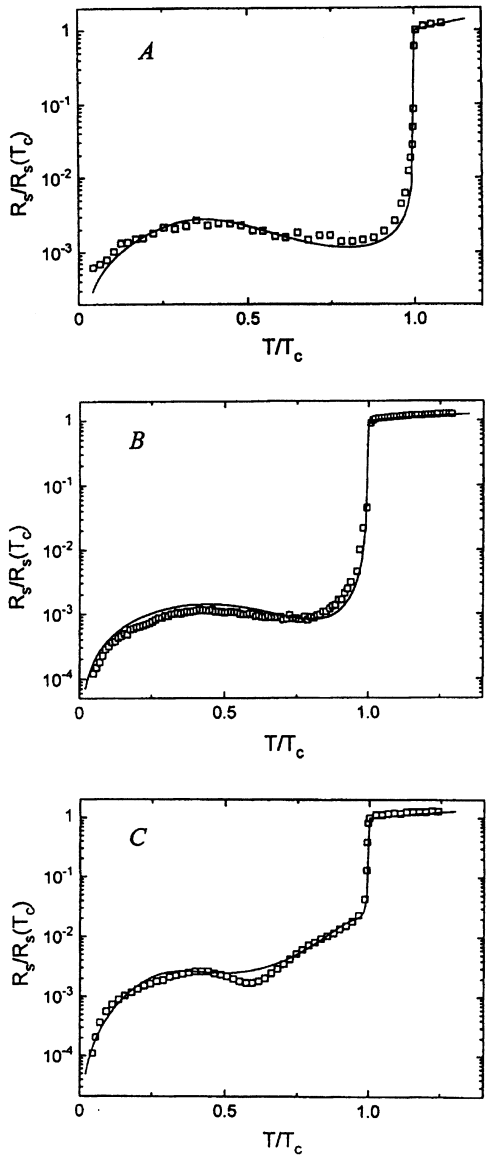

Figure 3.25 Comparison between calculations (solid lines) and measurements (open squares) of surface resistance versus temperature, $R_s(T)/R_s(T_c)$, in YBCO single crystals. Experimental data are taken from [32] (A, 4.13 GHz), [193] (B, 9.42 GHz), [185] (C, 10 GHz) and transformed ($\propto \omega^{3/2}$) to one frequency 10 GHz.

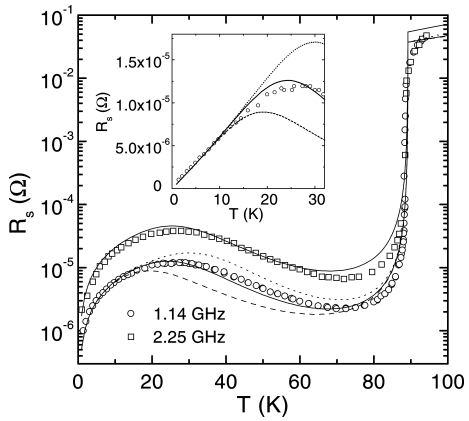

Figure 3.26 Experimental $R_s(T)$ data of YBCO single crystal [91] at 1.14 GHz (circles) and 2.25 GHz (squares). Solid curves are calculations using (3.12), (3.9), and (3.50). The dashed curves are calculated at 1.14 GHz with the term t^5 replaced by t^4 in the numerator of (3.50), the dotted curves with t^6. The inset shows a linear plot of $R_s(T)$ at low temperatures at 1.14 GHz.

$\beta \simeq 4t_m^5$ [197]. As β increases, the maximum and minimum of $R_s(T)$ change into an inflection point with a horizontal tangent; for larger β, the maximum of $R_s(T)$ disappears completely [56].

The linear growth of $R_s(T)$ with T at low temperatures (inset in Figure 3.26) is a direct consequence of the linear change of $\lambda(T)$ near $T = 0$, which is proportional to the coefficient α in (3.47), and is the result of a constant scattering rate at low temperatures, as shown in Figure 3.24.

The dashed and dotted curves shown in Figure 3.26 are the calculated $R_s(T)$ values at 1.14 GHz, with t^5 replaced by t^4 (dashed curve) and by t^6 (dotted curve) in (3.50). The best fit of the experimental data is $1/\tau(t) \propto t^5$.

The calculated curves in Figures 3.25 and 3.26 are very close to the experimental data and display the common and unique features of $R_s(T)$ for $T < T_c$ and $\omega\tau < 1$ of high-quality YBCO single crystals fabricated by different methods, namely: (i) the linear temperature dependence of the surface resistance, $\Delta R_s(T) \propto T$, caused by the linear variation of $\Delta X_s(T) \propto \Delta\lambda_{ab}(T) \propto T$ at temperatures $T \ll T_c$, and by the limit $\tau(T) \to \text{const}$ at low temperatures; (ii) the broad peak of $R_s(T)$ in the intermediate temperature range due to the rapid decrease of the relaxation time $\tau(T) \propto T^{-5}$ with increasing temperature; and (iii) the increase in $R_s(T)$ in the range $T_c/2 < T < T_c$ (Figure 3.25, curve C) caused by the crossover from T^{-5} to T^{-1} of $\tau(T)$ in (3.53), which occurs in this sample (C) at a lower temperature than in samples A and B (Figure 3.25). The behaviour of $1/\tau(T)$ for two YBCO crystals corresponding to curve C in Figure 3.25 and to plots in Figure 3.26 is shown in Figure 3.24.

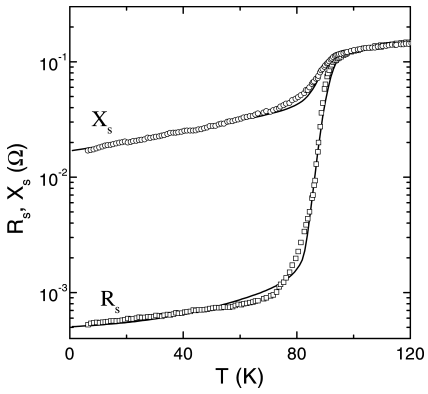

Figure 3.27 Comparison between the calculated (solid lines) and measured surface impedance (symbols) of BSCCO single crystal (see Figure 3.11). A constant $R_{\rm res} = 0.5$ mΩ is added to the values of $R_s(T)$ obtained from (3.12).

3.5.1.2 Inclusion of Residual Surface Resistance

Up to this point, our analysis has not taken the residual surface resistance $R_{\rm res}$ of the samples into account. At frequencies about 10 GHz, in the ab-plane of YBCO single crystals the resistance $R_{\rm res} \sim 100\ \mu\Omega$. The ratio $R_{\rm res}/R(T_c) < 10^{-3}$ in the samples whose data are plotted in Figures 3.25, 3.26 is so small that $R_{\rm res}$ can be neglected even at $T \ll T_c$. In most HTS crystals that were investigated, however, $R_{\rm res}/R(T_c) > 10^{-3}$ and the contribution $R_{\rm res}$ to the calculated function $R_s(T)$ is essential. Figure 3.27 compares measurements of $X_s(T)$ and $R_s(T)$ plotted in Figure 3.11 with calculations by (3.12) and (3.13). In this case, we have added to $R_s(T)$ from (3.12) the constant $R_{\rm res} = 0.5$ mΩ. The calculation using $\omega\tau(T_{\rm c}) = 0.9 \cdot 10^{-2}$, $\beta = 2$ and $\kappa = 3$ in (3.53) is based on measurements of $\sigma_2(T)$ obtained in the same experiment and plotted in Figure 3.34 (see below). It is clear that the agreement between the calculated and experimental curves is fairly good throughout the temperature interval $5 \le T \le 120$ K.

Another reason for including $R_{\rm res}$ is the increase in the ratio $R_{\rm res}/R(T_{\rm c}) \propto \omega^{3/2}$ with the frequency ω. The plots in Figure 3.28 are based on the experimental data of BSCCO single crystal measured in [122] at three frequencies: 14.4 GHz ($\omega\tau(T_c) = 0.7 \times 10^{-2}$), 24.6 GHz, and 34.7 GHz. The solid curves are the calculations at these frequencies obtained from (3.9) and (3.12) using $\tau(T)$ from (3.53) with $\beta = 0.1$ and $\kappa = 4$. The comparison procedure is different from that discussed above for YBCO crystals because $R_{\rm res} \propto \omega^2$ is added to the calculated $R_s(T)$ values. The inset of Figure 3.28 shows a linear plot of the measured and calculated surface resistance at low temperatures. We emphasize that at temperatures below $T_c/2$, the value of $\Delta R_s(T)$ is proportional to T.

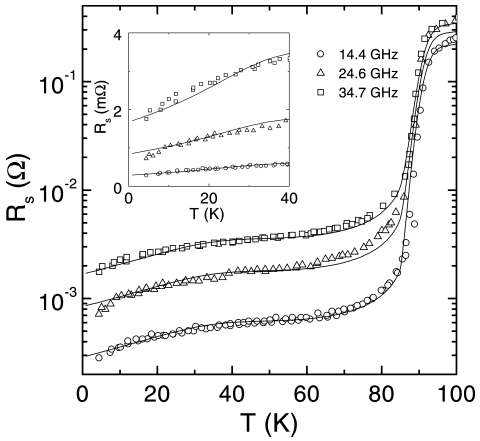

Figure 3.28 Experimental data of the BSCCO single crystal [122] at various frequencies: 14.4 GHz (circles), 24.6 GHz (triangles), and 34.7 GHz (squares). The solid curves are the calculated $[R_s(T) + R_{\rm res}]$–functions, with the respective $R_{\rm res}$ values of 0.29, 0.85 and 1.7 mΩ. The inset shows the linear temperature dependences of the surface resistance at low temperatures.

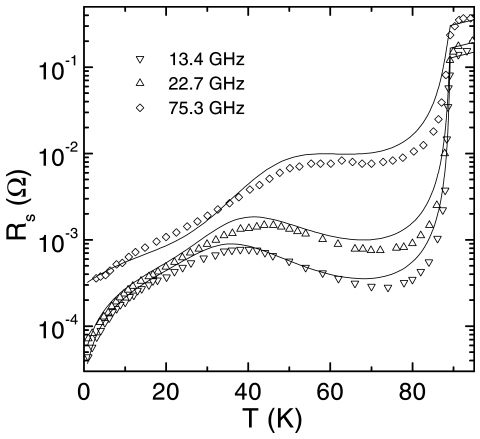

Figure 3.29 Comparison between the calculated (lines) and measured [91] (symbols) surface resistance $R_s(T)$ of the YBCO single crystal at 13.4, 22.7, and 75.3 GHz (see Figure 3.16). We assumed $R_{\rm res} = 0.3$ mΩ for 75.3 GHz, zero for the other frequencies.

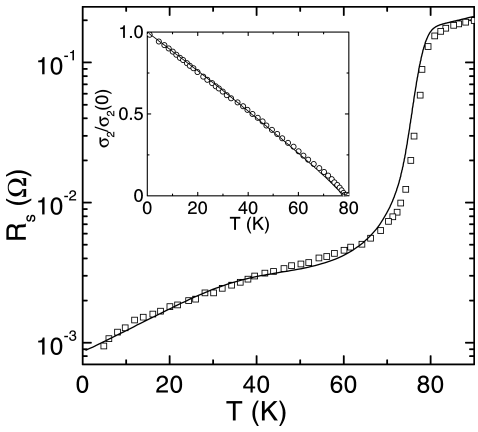

Figure 3.30 Surface resistance $R_s(T)$ of a TBCO single crystal at 24.8 GHz taken from [35] Solid curve is the calculated $(R_s(T) + R_{\rm res})$-function with $R_{\rm res} = 0.8$ mΩ. The inset shows the measured [35] (circles) and calculated results of $\sigma_2(T)/\sigma_2(0)$ (solid line), using (3.54) with $\alpha = 0.9$.

In the millimeter and shorter wavelength bands, the condition $\omega\tau < 1$ may not be satisfied in the superconducting state of the purest HTS single crystals because of the fast growth of $\tau(T)$ with decreasing $T < T_{\rm c}$. In this case, it is natural not only to take $R_{\rm res}$ into account but also use more general (3.8) of the two-fluid model to replace (3.9). The $R_s(T)$ data of [91] plotted in Figure 3.16 at the frequencies of 13.4, 22.7, and 75.3 GHz are compared to calculations of $R_s(T)$ in Figure 3.29. We used $\tau(T_c)/\tau(0) \approx \beta = 5 \times 10^{-3}$ in (3.50, 3.51) for all curves shown in Figure 3.29 (the same as previously used in Figure 3.26) and added $R_{\rm res} = 0.3$ mΩ to $R_s(T)$ (3.12) at 75.3 GHz only. The conductivity components $\sigma_1(T)$ and $\sigma_2(T)$ involved in (3.12) are obtained from the experimental data of $\sigma_2(T)/\sigma_2(0)$ at 1.14 GHz [91] (shown in Figure 3.31) and from (3.8).

Figure 3.30 shows another example. The experimental $R_s(T)$ data (squares) of a TBCO single crystal ($T_c = 78.5$ K) [35] are compared with the results of calculations based on (3.12), (3.8), and (3.53). The curve representing the theoretical values $R_s(T) + R_{\rm res}$ is plotted using $\beta = 0.1$, $\kappa = 5.5$, $\omega\tau(T_{\rm c}) = 1.7 \times 10^{-2}$, $R_{\rm res} = 0.8$ mΩ, and with $\sigma_2(T)/\sigma_2(0)$ shown in the inset (circles) of Figure 3.30.

3.5.2 Temperature Dependence of the Superconducting Electron Density

In the previous section, we emphasised that the modified two-fluid model describes well all features of the surface resistance $R_s(T)$ of different HTS's over a wide frequency range with only one parameter, κ. This was done using the measured (known from the same experiment) T-dependences of the superconducting electron density

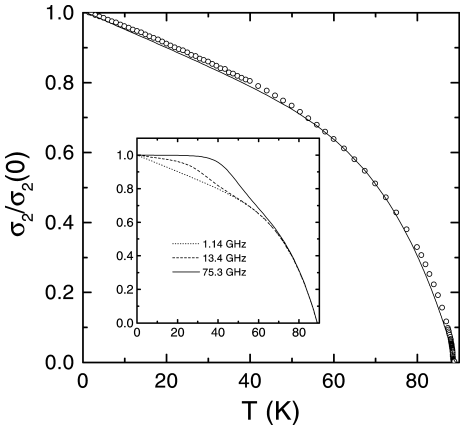

Figure 3.31 Plots of (3.54) (dashed line, $\alpha = 0.42$) and (3.55) (solid line, $\alpha = 0.47$), showing the fit to the empirical $\sigma_2(T)/\sigma_2(0)$. The experimental data (circles) are from [91] at 1.14 GHz. The inset shows the temperature dependences of $\sigma_2(T)/\sigma_2(0)$ at various frequencies, calculated from (3.8), (3.55) and (3.50).

$\lambda_{ab}^{-2}(T)$. However, we think that this phenomenological model would be incomplete unless simple formulas are available that correctly describe the measurements of $\Delta\lambda_{ab}(T)$. Figures 3.30 (the inset), 3.31, 3.32, and 3.33A show $\sigma_2(T)/\sigma_2(0) = \lambda^2(0)/\lambda^2(T) = n_s(T)/n$ in the ab-plane of different HTS single crystals from [35, 91, 122] and [32], respectively. All of these quantities change linearly with temperature at low temperatures and can be approximated by the function [194]

$$\frac{n_s}{n} = (1-t)^{\alpha}, \tag{3.54}$$

where α is a numerical parameter. For $t \ll 1$, (3.47) follows from (3.54). For the cited experiments, the values of α fall into the range $0.4 < \alpha \leq 0.9$. Near T_c, we obtain $\lambda(t) \propto n_s(t)^{-1/2} \propto (1-t)^{-\alpha/2}$, which is also in reasonably good agreement with the experimental data. However, (3.54) yields an infinite value of the derivative $\mathrm{d}\sigma_2(t)/\,\mathrm{d}t \propto (1-t)^{\alpha-1}$ at $t = 1$ for $\alpha < 1$.

An approximation for $n_s(t)/n$ proposed in [58] is close to (3.54),

$$\frac{n_s}{n} = 1 - \alpha t - (1-\alpha)t^6, \tag{3.55}$$

and is shown by solid lines in Figures 3.31 and 3.32. Equation (3.55) ensures that the slope of $\lambda^2(0)/\lambda^2(t)|_{T_c} = (5\alpha - 6)$ at T_c is finite and negative for $\alpha < 1.2$.

However, taking the above functions for $n_s(t)$ in their simplest forms (3.54) and (3.55) does not account for all features in $\lambda^2(0)/\lambda^2(T)$ detected recently in YBCO crystals (see Table 3.1) in the intermediate temperature range [193, 185, 217, 186]. Moreover, the slope of these curves at $T \ll T_c$ requires that $\alpha > 1$ in (3.54), which would lead to zero slope of the $\sigma_2(T)/\sigma_2(0)$ curve at $T = T_c$. Therefore,

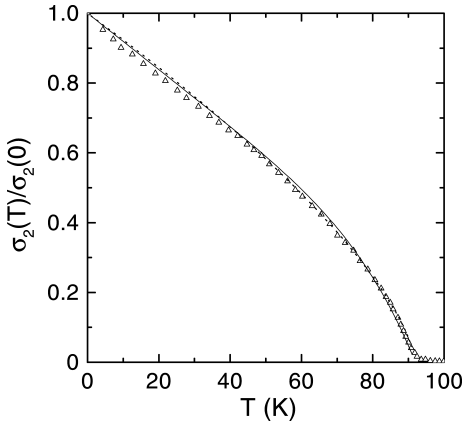

Figure 3.32 Comparison between the calculated (solid curve: (3.55), $\alpha = 0.74$; dotted line: (3.54), $\alpha = 0.7$) and measured [122] (symbols) of the $\sigma_2(T)/\sigma_2(0)$ values of BSCCO single crystal [58].

we have added an additional empirical term to the right-hand side of (3.54) without violating the particle conservation condition $n_s + n_n = n$,

$$\frac{n_s}{n} = (1-t)^{\alpha}(1-\delta) + \delta(1-t^{4/\delta}), \tag{3.56}$$

where $0 < \delta < 1$ is the weight factor. For $\delta \ll 1$ and $\alpha > 1$, the dominant contribution to $\sigma_2(T)$ throughout the relevant temperature range is still due to the first term on the right-hand side of (3.56), while the second is responsible for the finite slope of $\sigma_2(T)/\sigma_2(0)$ at $T = T_c$, which is equal to -4 in accordance with the GC model. As δ increases, the second term on the right-hand side of (3.56) becomes more essential. The experimental curve of $\sigma_2(T)/\sigma_2(0)$ in Figure 3.33B derived from the $R_s(T)$ and $X_s(T)$ measurements plotted in Figure 3.10 is properly described by (3.56) with $\delta = 0.5$ and $\alpha = 5.5$. This calculation reflects the characteristic features of the experimental data, namely, the linear section of n_s and the positive second derivative ($\alpha > 1$) in the low-temperature range, the plateau in the intermediate temperature range, and the correct value of the slope near T_c. The whole set of $\sigma_2(T)$ curves measured in the ab-plane of YBCO crystals grown at ISSP using the same technique is described by (3.56), where α was almost constant, $\alpha \approx 5.5$, and δ was varied between 0.1 and 0.5 [190].

Using the same relationship (3.56) at $\alpha = 2$ and $\delta = 0.2$, we can describe the dependence $\sigma_2(T)$ in the BSCCO crystal (Figure 3.22), plotted in Figure 3.34.

The third curve in Figure 3.33C [185], which corresponds to the curve of $\lambda(T)$ in Figure 3.18(1), is different from typical curves of Figures 3.18(2, 3) and 3.30–3.32, since a linear section of $\sigma_2(T)$ is observed only in a narrow range of temperatures, $0 < T \ll T_c$, and it switches to a quadratic dependence as the temperature increases. This crossover can be described [193] by introducing additional factor

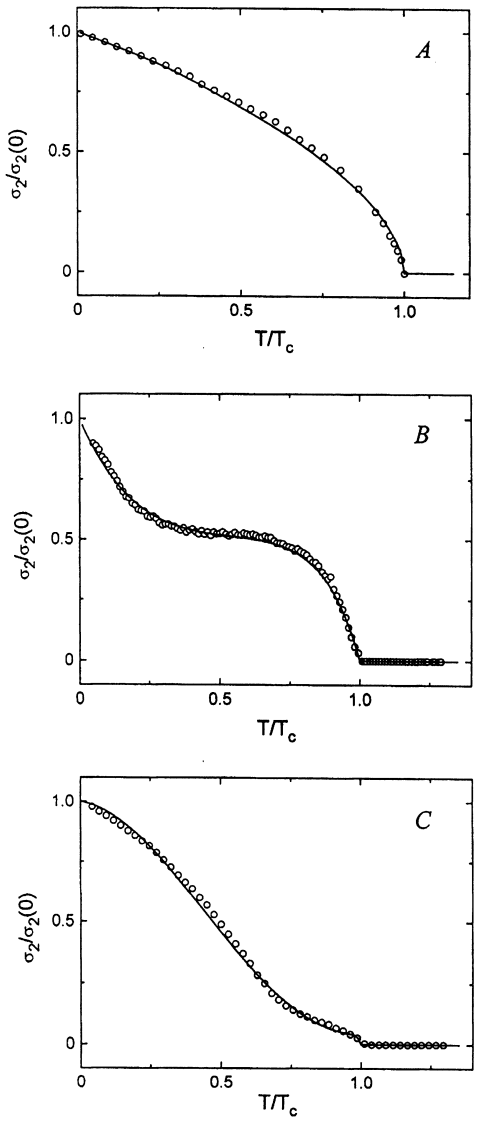

Figure 3.33 Comparison between calculations (solid lines) and measurements (circles) of $\sigma_2(T)/\sigma_2(0) = \lambda^2(0)/\lambda^2(T)$ of YBCO single crystals. Experimental data are taken from Refs. [32] (A), [193] (B), and [185] (C).

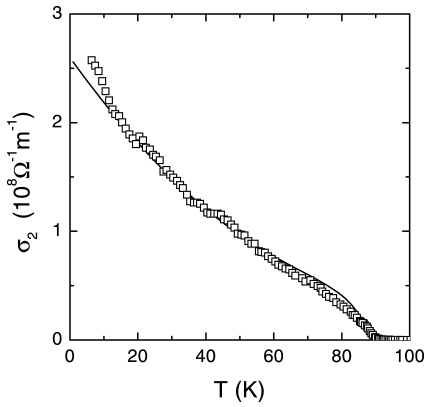

Figure 3.34 Imaginary part of conductivity in BSCCO single crystal (open squares) derived from the surface impedance measurements of Figure 3.11. Solid line corresponds to (3.56).

$(1 + \eta t)$ to the first summand on the right of (3.56) for $n_s(t)$; thus we can obtain the solid curve of Figure 3.33C at $\alpha = 2.2$, $\eta = 2$, and $\delta = 0.04$.

3.5.3 Real Part of Conductivity

It naturally follows from the fact that the measurements and calculations of $R_s(T)$, $X_s(T)$, and $\sigma_2(T)$ are in good agreement that the curves of $\sigma_1(T)$ in the range $T < T_c$ can be described in terms of the modified two-fluid model by using the first formula of (3.14). Here we have to consider two points that are important in calculations of $\sigma_1(T)$.

Firstly, in comparing the calculations based on the modified two-fluid model to the measurements of the surface resistance we added to the function $R_s(T)$ determined by the general formula (12) the value $R_{\rm res}$, which was determined in the same experiment and is independent of the temperature. For this reason, the curves of $\sigma_1(T)$ in Figures 3.35–3.37, which were calculated by (3.14) and (3.57) represented below, do not tend to zero as $T \to 0$, even though the normal carrier density $n_n = 0$ at $T = 0$, according to the two-fluid model, and, as it follows from (3.8) or (3.9), the conductivity should tend to $\sigma(0) = 0$. The parameter $R_{\rm res}$ was not included in (3.14) when we compared the data of Figure 3.38 with calculations because in that case the ratio $R_{\rm res}/R_s(T_c)$ was very small, less than 10^{-3} (see the lower curve in Figure 3.16).

The second point that has not been discussed as yet is the behaviour of $R_s(T)$ and $\sigma_1(T)$ in the temperature range about T_c. The most spectacular manifestation of this behaviour is the peak in the real part of the conductivity (see Figures 3.4, 3.19–3.23). This peak can be described by an effective medium model [192, 71, 197] that takes the inhomogeneous broadening of the superconducting transition into

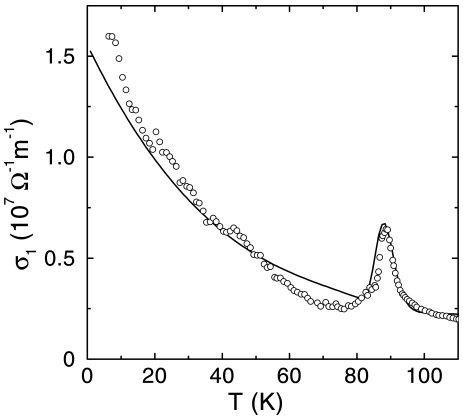

Figure 3.35 Comparison of the plot in Figure 3.22 and calculation based on the modified two-fluid model taking into account the inhomogeneous broadening of the superconducting transition ($\delta T_c = 4.5$ K).

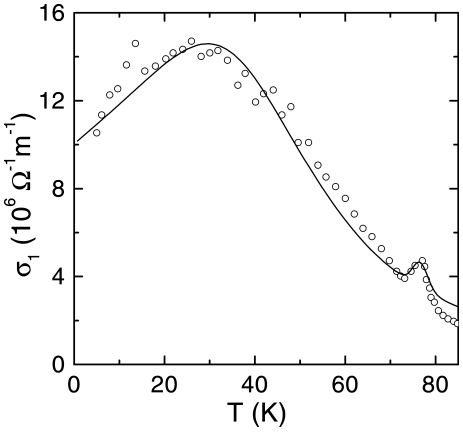

Figure 3.36 Comparison of the experimental T-dependence of $\sigma_1(T)$ (open circles) of the TBCO single crystal at 24.8 GHz [35] with the one calculated using the modified two-fluid model (solid line) and taking the inhomogeneous broadening of the superconducting transition into account ($\delta T_c = 2.5$ K in (3.57)).

account. We assume that different regions of a given specimen experience transitions to the superconducting state at different temperatures within the T-range δT_c. If the dimension of each of these regions is smaller than the magnetic field penetration depth (microscopic-scale disorder), the distribution of the microwave currents over the sample is uniform and the calculation of the effective impedance $Z_{\rm eff}$ of the sample reduces to two operations: first, adding the impedances Z_s of all regions in the specimen (with different T_c) that are connected in series along a current path,

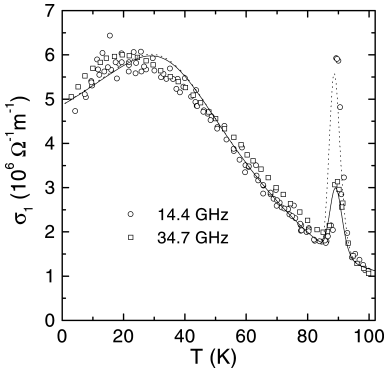

Figure 3.37 Comparison of $\sigma_1(T)$ calculated with help of (3.50), (3.12), (3.57, $\delta T_c = 2$ K), and (3.8) with the data at 14.4 and 34.7 GHz (Figure 3.23) from [122].

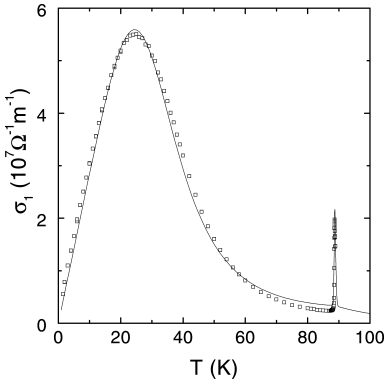

Figure 3.38 Comparison of the experimental dependence $\sigma_1(T)$ (open squares in Figure 3.20) of YBCO single crystal at 1.14 GHz [91] and that calculated with modified two-fluid model (solid line) taking into account the inhomogeneous broadening of the superconducting transition ($\delta T_c = 0.4$ K in (3.57)).

and second, averaging over the sample volume. As a result, we obtain

$$Z_s^{\rm eff}(T) = R_s^{\rm eff}(T) + iX_s^{\rm eff}(T) = \int\limits_{\delta T_c} Z_s(T, T_c) f(T_c)\ {\rm d}T_c\ , \tag{3.57}$$

where the distribution function $f(T_c)$ is such that the fraction of the sample volume with critical temperatures in the range $T_c < T < T_c + {\rm d}T_c$ equals $f(T_c)\,{\rm d}T_c$. In the simplest case, $f(T_c)$ is a Gaussian function. For instance, in the experiments of [91], the width of the superconducting transition on the lower curve of $R_s(T)$ in Figure 3.16 was approximately 0.4 K, which we equate to the width of the Gaussian

distribution $f(T_c)$. Using general relations (3.14) with the effective impedance components obtained from (3.57), we calculate $\sigma_1^{\rm eff}(T)$ near T_c at 1.14 GHz and plot it together with the experimental data in Figure 3.38.

In the framework of the discussed approach, $\sigma_1^{\rm eff}(T)$ displays a narrow peak at $T^* = T_c - \delta T_c$. It is easy to check that the relative peak amplitude is approximately equal to

$$\frac{\sigma_1(T^*) - \sigma(T_c)}{\sigma(T_c)} \approx \begin{cases} \gamma & \text{if } \gamma > 1, \\ \gamma^2 & \text{if } \gamma < 0.1, \end{cases} \tag{3.58}$$

where $\gamma = \delta T_c/[T_c\omega\tau(T_c)]$, implying that the peak decreases with the decrease of the superconducting resistive transition width. Usually, experiments yield $\gamma > 1$ (e.g., the data of [91] give $\gamma \simeq 7$ at 1.14 GHz) and, therefore, the peak amplitude should be inversely proportional to the frequency. This assertion is supported by the comparison between the curves of $\sigma_1(T)$ (the lines in Figure 3.37) from [122] obtained at two different frequencies on the same BSCCO crystal as was used in Figures 3.28 and 3.32.

In calculating the $\sigma_1(T)$ curves for other specimens, we also applied the above procedure to incorporate corrections caused by the inhomogeneous broadening of the superconducting transition. We adjusted the calculations of $R_s(T)$ (Figures 3.27, 3.30) and $\sigma_2(T)$ (Figure 3.34 and the inset to Figure 3.30) by substituting the resulting $Z_s^{\rm eff}(T)$ into the general equation (3.14) for the conductivity σ_1. The resulting curves for BSCCO and TBCO are shown in Figures 3.35, 3.36.

3.5.4 Summary

To sum up, one can describe characteristic features of $Z_s(T)$ and $\sigma_s(T) = \sigma_1(T) - i\sigma_2(T) = i\omega\mu_0/Z_s^2(T)$ in the ab-plane of high-quality HTS crystals by generalizing the well-known GC two-fluid model as follows.

(i) We introduce a temperature dependence of the relaxation time of the quasiparticles in accordance with the Bloch–Grüneisen law. We find that the $R_s(T)$ curves in different HTS crystals are well described using (3.50) or (3.53) for $1/\tau(T)$. In the latter equation, there is only one fitting parameter, $\kappa = \Theta/T_c$, while the other parameter β from (3.51) can be estimated directly from the experimental data with the help of (3.48) and (3.52). The absence of the broad peak of $R_s(T)$ in tetragonal HTS single crystals is due to a less rapid increase of $\tau(T)$ with decreasing the temperature. In other words, the value of β is smaller for YBCO crystals than for BSCCO, TBCO, or TBCCO. For the latter crystals, the residual losses $R_{\rm res}$ are usually large and they have to be taken into account.

(ii) We replace the well-known temperature dependence of the density of superconducting carriers in the GC model, $n_s = n(1 - t^4)$, by one of the functions in (3.54), (3.55) or (3.56). All of these functions change linearly with the temperature for $t \ll 1$ (see (3.47)). This permits one to extract the common and distinctive features of $X_s(T)$ and $\sigma_2(T)$ from different HTS crystals.

It also follows from the equations of the modified two-fluid model that at low temperatures ($t \ll 1$) and low frequencies ($\omega\tau(0) < 1$), all curves of $Z_s(T)$ and $\sigma_s(T)$ have linear regions: $\sigma_1 \propto \alpha t/\beta$, since $n_n/n \approx \alpha t$ and $\tau \approx \tau(0) \approx \tau(T_c)/\beta$. Furthermore, $\Delta\sigma_2 \propto -\alpha t$. In accordance with (3.17), we then have $R_s \propto \alpha t/\beta$ and $\Delta X_s \propto \Delta\lambda \propto \alpha t/2$. As the temperature increases, the curve of $\sigma_1(t)$ passes through a maximum at $t \lesssim 0.5$ if the inequality (3.46) is valid. This peak is due to the superposition of two competing effects, namely, the decrease in the number of normal carriers as the temperature decreases, for $t < 1$, and the increase in the relaxation time, which saturates at $t \sim \beta^{1/5}$, where the impurity scattering starts to dominate. If inequality (3.46) fails, the function $\sigma_1(t)$ changes monotonically with the temperature. The model also accounts for the peculiarities of the surface impedance and complex conductivity at higher temperatures in HTS single crystals manufactured using different techniques. In particular, the features in the $X_s(T)$ and $\sigma_2(T)$ curves for YBCO single crystals in the intermediate temperature range (plateau [193] or bump [185]) can be described within the framework of the modified two-fluid model if we take into account the modification of $n_s(t)$ described by (3.56) with $0 < \delta \leq 0.5$.

In HTS single crystals, the narrow peak in the real part of the conductivity $\sigma_1(T)$ occurring near T_c can be explained in terms of an effective medium model, where the strong electron–phonon coupling of the quasiparticles and the inhomogeneous broadening of the superconducting transition are taken into account.

3.6 ON THE WAY TO A MICROSCOPIC THEORY

In spite of progress on the materials aspects of the phenomenon of high temperature superconductivity, there are widely different views as to the pairing mechanism responsible for this effect. In addition to conventional electron–phonon interaction, many other explanations were proposed some of them being of quite exotic nature.

The normal state properties of HTS's are quite unusual as well. Strong anisotropies are observed mainly caused by the nearly two-dimensional nature of electronic properties of these materials. Besides the normal-superconducting phase transition, the new copper oxides show an unusually complex phase diagram. For example, the YBCO compounds display a wide range of behaviour, including the metallic superconductor-to-magnetic insulator change due to variation of the oxygen content. Single crystal measurements of resistivity as a function of temperature in the CuO_2 planes carried out for several different compounds have shown a linear behaviour over the measured temperature range, in some cases from 7 K to 700 K. This behaviour takes place only near the optimal chemical doping, i.e. that corresponding to highest critical temperatures.

Other anomalous normal state properties have been observed: optical conductivity and Raman scattering data suggest a peculiar temperature dependent charge carrier scattering rate, the Hall coefficient in YBCO exhibits a strong temperature dependence, in contrast to that of ordinary Fermi liquid metals. It is widely believed

that understanding the normal state properties of HTS's will also shed light on the superconducting mechanism.

Another important property of these superconductors is that they are related to antiferromagnetic insulators. A typical T–x (temperature–carrier concentration) phase diagram of the electronic properties of HTS's consists of several regions [23]. Near half filling (no holes in CuO_2 layers) the materials are antiferromagnetic insulators. With the increase of hole doping, the long range magnetic order fades away and superconductivity begins to prevail at low temperature at appropriate doping levels. The superconducting transition temperature increases with doping until it reaches a maximum and then decreases with further doping and the material eventually becomes a paramagnetic metal. Short range antiferromagnetic order still persists into the doping region where the superconducting ground state prevails.

The Fermi liquid picture is the underlying foundation of the traditional BCS theory. The unusual normal state properties raise the question about applicability of the Fermi liquid description to HTS's. The basic concept of the Landau theory of the Fermi liquid is that the properties of a system of fermion particles are not dramatically modified by the particle interactions, no matter how strong the interaction may be. This concept assumes a one-to-one mapping between 'quasi-particles' of an interacting fermion system and free particles of a non-interacting fermion system. Almost all metals are typically regarded as Fermi liquids. In the HTS's the conducting carriers are composed of oxygen *2p* electrons (holes) and strongly interacting copper *3d* electrons (holes), the on-site Coulomb repulsion between the *3d* electrons being very strong (strong correlation effects).

Given the controversy over the applicability of the Landau Fermi liquid model, much experimental and theoretical work has been carried out to test the validity of the Fermi liquid concept in the HTS's. Very important tool to study the electronic structure is high-resolution angle-resolved photoemission spectroscopy (ARPES) [177]. Despite the evidence of correlation effects, angle-resolved photoemission clearly demonstrated the existence of Fermi surfaces. Furthermore, the measured Fermi surfaces have similarities to those calculated theoretically by band theory [99, 15, 158, 39]. The key features in the electronic structure are very flat bands in CuO_2 band structure which have saddle point behaviour and significant Fermi surface nesting. These features will have a significant impact on the physical properties, including the temperature dependence of the resistivity, the isotope effect, the Hall effect and the symmetry of the superconducting gap.

The superconducting properties of cuprates are in many ways similar to those of conventional BCS superconductors. First, electron pairs in the superconducting state of the high T_c-oxides have been firmly established by flux quantization and Josephson tunneling experiments. The Cooper pairs in HTS's are spin singlet. The cuprates are strongly type II superconductors and magnetic field penetrates them in the form of vortices like in conventional superconductors. The existence of the energy gap has been established by a number of advanced experimental techniques like ARPES, electron tunneling and infrared reflectivity. It was shown that the maximum value of the gap exceeds the BCS value of $3.5k_BT_c$.

At the same time, the ARPES measurements on the highest quality samples showed significant gap anisotropy with the gap minimum close to zero near some points of the Brillouin zone [177]. The nature of orbital structure of the Cooper pairs in HTS's remains one of the central questions in the field. The issue of symmetry of the order parameter is discussed by Scalapino [172]. Many different types of experiments have been carried out aimed at probing the symmetry of the gap function, including tunneling, absorption of microwaves, Raman spectroscopy and Josephson junction measurements (see reviews by Dynes [48], Van Harlingen [79], and Goss Levi [74]). Most of them are consistent with the d-wave pairing. In order to distinguish between a very anisotropic s-wave gap function and a d-wave gap function the *phase-sensitive* measurements are necessary which is the case only for the Josephson junction experiments directly probing a phase difference. The outcome of the Josephson measurements in YBCO is that the gap function indeed changes its sign within a Brillouin zone (the so-called π-shift in a Josephson effect) which is consistent with the d-wave pairing (see review [172] and references therein).

In general, the fact of the sign reversal of the gap function does not necessarily prove a pure d-wave symmetry and may be a manifestation of a more complicated anisotropy related to repulsive interactions at some regions of a Fermi surface [5]. That means that the electron–electron interactions in the cuprates within the Brillouin zone are of alternative sign and have the symmetry of the lattice, but the key question about an origin of these interactions is not answered yet. The most important ingredients of the BCS theory are the superconducting electron pair formation (Cooper pairs) and the interaction responsible for the electron pairing. Whereas the existence of spin-singlet Cooper pairs in HTS's is firmly established, the question concerning the interaction is still open at present. The lack of consensus is due to inability of any simple theory, like the conventional BCS theory, to explain simultaneously many unusual properties of cuprates.

A variety of physical mechanisms of high temperature superconductivity have been discussed in literature, ranging from a purely phonon mechanism to a pairing due to repulsive interactions. As far as none of these mechanisms have been firmly identified yet, we just give a number of selected references, where a more specific information can be found. The phonon mechanism of pairing in application to cuprates with account of complicated band structure has been discussed by many authors. An early review was given by Pickett [157]. Application of the many-band generalization of the phonon pairing mechanism to cuprates was first done by Kresin and Wolf [119]. An important signature of the phonon mechanism of pairing in conventional superconductors is the existence of the isotope effect with the isotope exponent $\alpha = 1/2$. This exponent was found to be quite small in most of the cuprates, but this fact does not exclude the phonon mechanism since it can be attributed to anharmonic effects. There are several reasons why electron-phonon interaction in the cuprates may be strong enough to cause high T_c values (see reviews [66, 131] and references therein). First, strong hybridization of *d*-electron states of copper and *p*-electron states of oxygen leads to strong contribution of high-frequency oxygen phonon modes to the electron-phonon interaction. Second, the low dimensionally tends to increase the electronic density of states in the Cu–O planes. Both

these effects are favourable for high T_c values as given by the BCS theory. Finally, the layered structure favours an enhancement of electron–phonon interaction due to weaker screening of Coulomb potentials.

It is generally argued that the phonon mechanism itself is not fully responsible for high T_c values, and additional nonphonon attractive interactions contribute to the Cooper pairing. Among nonphonon mechanisms, the pairing due to exchange by acoustic plasmons and excitons was considered. Soft acoustic plasmons are present in the cuprates due to their layered structure, whereas exciton modes may originate from nonmetallic interlayers existing between the Cu–O planes. The exciton pairing mechanisms was first proposed by Littl [126] and Ginzburg [65] (see also the reviews by Carbotte [37], Ginzburg and Maksimov [66], and references therein). The model based on the extended saddle point singularities in the electron spectrum of the cuprates, weak screening of the Coulomb interaction and phonon-mediated interaction between electrons was proposed by Abrikosov [5]. The pairing mechanism based on the bipolaron formation due to strong phonon or spin interactions was discussed by Micnas *et al.* [146] and Alexandrov *et al.* [10]. A number of unconventional pairing mechanisms not involving electron–phonon interaction were proposed for the cuprates. Most of them employ the idea that the magnetic correlations which manifest themselves in the aforementioned T–x phase diagrams play the key role in the Cooper pairing. Several phenomenological and microscopic approaches have been developed quite recently in the context of purely electronic Hubbard type models which focus on the role of antiferromagnetic spin fluctuations. The minimal model describing hole motion in Cu–O plane is the t–J model [13]. The spin fluctuation exchange is then considered as a pairing mechanism. The physical assumptions and the outcomes of the spin-fluctuation model are described in [172, 42, 105].

To summarize, at present there is no general consensus on the proper theory of HTS, which must account for the results of the phase sensitive experiments [79, 198, 74] indicating a dominating d-wave order parameter component and possibly a non phonon mechanism. Further theoretical and experimental work is needed to identify the mechanism of superconductivity in HTS's. For the most recent update on the present status of HTS theory see the review of Maksimov [131].

Let us set aside feasible mechanisms of superconducting pairing in HTS and briefly analyze the existing microscopic theories of the high-frequency response of HTS materials. Given the phenomenological model formulated in the previous section, which is in fairly good agreement with measurements of $Z_s(T)$ in HTS crystals, it is natural to compare the tenets of this model with results of the microscopic theory. In this way, some progress to clear understanding of a universal microscopic approach to microwave properties of HTS may be possible.

3.6.1 Isotropic SC Model and Relaxation Time in the Superconducting State

Eliashberg's equations, which take into account effects of delay and damping of quasiparticles, apply to superconductors with an arbitrarily strong interaction in the

Fermi liquid. In the case of electron–phonon interaction in an isotropic one-band superconductor with singlet s-wave paring and Debye spectrum of phonons, the electron relaxation rate $\Gamma(T) = 1/2\tau(T)$ is proportional to T^3 for $T < T_c$ [66, 131, 116] if Eliashberg's equations are solved by neglecting the phonon corrections to the electromagnetic vertex. If these corrections are taken into account [52], then $\Gamma(T) \propto T^5$, which is in agreement with (3.50). Using this result, the authors of [45] proved that peaks on curves of $R_s(T)$ and $\sigma_1(T)$, which are characteristic features of YBCO, can be obtained on the base of the conventional isotropic SC model, although quantitative agreement between this model and experimental data is out of question. The theory suggested by Eliashberg *et al.* [52] is the first model applied to the HTS microwave response taking into account vertex corrections. However, it is not clear whether these results would apply to microscopic models more adequate for description of HTS.

Roddink and Stroud [169] have described a simple model to estimate the effect of order parameter phase fluctuations on the penetration depth of HTS's, without taking into account the line nodes of the order parameter on the Fermi surface (d-wave symmetry). They have shown that, when treated classically, such fluctuations are found to produce a linear temperature dependence of the penetration depth, which may be comparable to the experimentally observed magnitude.

Very recently the role of vertex corrections and Fermi liquid corrections in a low temperature electrical conductivity of a d-wave superconductor with impurities was discussed by Durst and Lee [47]. The weak coupling regime was considered. It was shown that the universal scattering-independent behaviour of conductivity at low frequency $\omega \to 0$ and low temperature $T \to 0$ (see (3.59) below) breaks down. It might be interesting to find out how these results modify the temperature dependence of conductivity at finite T and ω, in particular when a realistic electron–electron interaction is taken into account.

3.6.2 Model of Almost Antiferromagnetic Fermi Liquid

In this model [145, 147, 148], low-frequency excitations in the medium are not phonons, but weakly damped spin waves, and superconducting pairing is mediated by spin fluctuations. The paramagnon mechanism leads to a d-wave symmetry of the order parameter, when the Fermi surface contains lines on which the gap width turns to zero. This means that there are quasiparticles in the superconductor even at $T = 0$, hence the finite conductivity [121]

$$\sigma_{\min} = \frac{ne^2}{m\pi\Delta_0} = \frac{2\Gamma(T_c)\sigma(T_c)}{\pi\Delta_0}. \tag{3.59}$$

Here $2\Gamma(T_c) = 1/\tau(T_c)$, and Δ_0 is the maximum gap width on the Fermi surface, $\Delta_0 = 2.14T_c$ (hereafter $\hbar = k_B = 1$) if strong coupling effects are neglected. Recall that $2\Gamma(T_c) = 2 \times 10^{13}$ s^{-1} $\simeq 0.8T_c$ for YBCO single crystals [32, 193, 185], then

we derive from (3.59) $\sigma_{\min} \simeq 0.1\sigma(T_c)$, and substitution of this parameter in (3.17) yields the minimum surface resistance $R_{\mathrm{s}\,\min}$ of a d-wave superconductor. At a frequency of 10 GHz in YBCO $R_{\mathrm{s}\,\min} \sim 1\ \mu\Omega$, i.e., one-two order of magnitude lower than the best experimental data reported to date.

These manifestations of the d-wave symmetry, which are unusual from the viewpoint of the conventional approach, stimulated theoretical studies of various HTS properties on the base of the model of almost antiferromagnetic Fermi liquid.

Hirschfeld *et al.* [88, 89] calculated the conductivity $\sigma_s(T)$ and surface resistance $R_s(T)$ as functions of temperature and compared them to experimental data by Bonn *et al.* [32]. Let us discuss these results in detail.

First let us consider the case of relatively low temperatures $T < 0.4T_c$, when the quasiparticle damping is due to their impurity scattering. In this range, as was indicated in [88, 89],

1. the integral expressions for the superconductor microwave response allow one to present the conductivity in the form of (3.8) with $\tau(T) \approx \tau(0) \equiv 1/2\Gamma$, where Γ is the rate of elastic relaxation; Γ is always smaller than $\Gamma(T_c)$, for example, in the experiment by Bonn *et al.* [32], $\Gamma/\Gamma(T_c) \simeq \tau(T_c)/\tau(5\ \mathrm{K}) \simeq \beta \approx 0.01$;
2. versions with weak (Born approximation) and strong (unitary limit) scattering characterized by phase shifts $\delta = 0$ and $\delta = \pi/2$, respectively, are considered.
3. there is a crossover temperature T^* defining the boundary between the 'gapless' ($T < T^* \ll T_c$) and 'pure' ($T^* < T \ll T_c$) regimes of superconductivity; in the unitary limit, whose conditions are closer to those of real experiments, $T^* \approx 0.8(\Gamma\Delta_0)^{1/2} \approx 0.1T_c \simeq 9$ K in the best YBCO crystals with optimal doping level; introduction of impurities (such as Zn [32]) leads to higher Γ and crossover temperature T^*.

In the 'pure' regime of superconductivity the field penetration depth is a linear function of reduced temperature $t = T/T_c$:

$$\frac{\lambda(t)}{\lambda(0)} = 1 + c_1 t, \quad c_1 = \frac{T_c \ln 2}{\Delta_0}. \tag{3.60}$$

This formula is in agreement with (3.47), (3.54–3.56), from which follows

$$\frac{\lambda(t)}{\lambda(0)} = 1 + \frac{\alpha t}{2}, \quad t \ll 1. \tag{3.61}$$

By taking $\alpha = 0.5$ (for the curve in Figure 3.33A) and $2c_1$ given in (3.60), we obtain $\Delta_0 \simeq 2.7T_c$ in the experiment reported by Bonn *et al.* [32]. At frequencies of 4 GHz ($\omega/T_c \simeq 0.002$) and 35 GHz ($\omega/T_c \simeq 0.019$) the parameter ω/Γ in [32] equals $0.2T_c$ and $1.9T_c$, respectively, which corresponds to an intermediate region between the hydrodynamic ($\omega/\Gamma \ll 1$) and collisionless ($\omega/\Gamma \gg 1$) limits. According to numerical calculations [88, 89] for this intermediate region (measurements

at 35 GHz in [32] are well within this region), the conductivity $\sigma_1(T)$ is a linear function of T. Figure 9 in [89] clearly shows that the slope of the line describing $\sigma_1(T)/\sigma(T_c)$ at $T \ll T_c$ is close to α/β, which is given by the phenomenological model.

As the concentration of impurities increases, the 'pure' regime at low temperatures is replaced by the 'gapless' one, and from the intermediate region the system is shifted to the hydrodynamic one, as a result, we have $\Delta\lambda(T) \propto T^2$ and $\sigma_1(T) \propto T^2$. This conclusion was confirmed by measurements [32] of samples with Cu atoms substituted by Zn impurities.

In the temperature range $T > 0.4T_c$ processes of inelastic scattering are essential. The quasiparticle damping factor due to scattering by spin fluctuations versus temperature was calculated neglecting vertex corrections [165], and the result was proportional to T^3: $1/\tau(T) \propto T^3$. With due account of this formula, calculations in the range of intermediate temperatures and in the neighbourhood of T_c produced maxima on curves of $\sigma_1(T)$ and $R_s(T)$ [88, 89]. Unfortunately, the parameter $\Gamma/T_c = 0.0008$ used in those calculations was undervalued, therefore it was useless to compare these calculations with accurate experimental data. One remarkable fact revealed by this comparison was that the peak in the calculated $R_s(T)$ was shifted to lower temperatures with respect to the measured position, which might be caused by the insufficiently strong temperature dependence of $1/\tau$ in the calculations (compare with Figure 3.26).

Thus, the d-wave model of the microwave response [88, 89] is in qualitative agreement with measurements of surface impedance in YBCO at low temperatures [32] and is consistent from the formal viewpoint with the phenomenological model considered above at $T \ll T_c$. A significant advantage of these calculations [88, 89] is the visual demonstration of nontrivial consequences of the d-wave order parameter applied to investigations of microwave response of high-quality YBCO single crystals using the minimal number of fitting parameters. It seems that curves of $\sigma_2(T)$ measured in tetragonal HTS crystals, like those shown in Figure 3.33A, can be also described by this model. On the other hand, this model cannot account for the linear section of the $R_s(T)$ curves extending to $T_c/2$ (at a frequency of 10 GHz), observation of radically different values of the $\sigma_2(T)$ slope for $T \ll T_c$ (which corresponds to $\alpha > 1$ in (3.56) and, in accordance with (3.60), to $\Delta_0 < T_c$) in experiments with YBCO crystals [180, 193, 185, 217, 186], not to mention features in the range of intermediate temperatures, and, finally, the large slopes of $R_s(T)$ and $\sigma_2(T)$ curves as $T \to T_c$.

This approach was further developed in the work by Hensen *et al.* [84], who compared in detail calculations and measurements of $Z_s(T)$ at a frequency of 87 GHz in two different YBCO films. They investigated theoretically the evolution of functions $\sigma_s(T)$ and $R_s(T)$ as a result of a transition from the unitary to Born limit and demonstrated that the minimal conductivity in (3.59) is not a universal parameter, and the experimental curves are best described at an intermediate scattering phase shift $\delta \approx 0.4\pi$. They matched their calculations to the experimental data using a combination of six (or even nine) fitting parameters. Three parameters were contained in a phenomenologically introduced temperature depen-

dence of the inelastic relaxation time $\tau(1)/\tau(t) = at^3 + (1-a)\mathrm{e}^{b_1(t-1)[1+b_2(t-1)^2]}$, where $t = T/T_c$. In the case of film B with higher characteristics [84], the parameter $a = 0$, and the remaining terms are well approximated by the function $1/\tau(T) \propto T^5$. It is desirable to apply this calculation technique [84] and its version generalized to the case of strong coupling [29] to measurements of HTS crystals in the centimetre wavelength band. The analysis of optical conductivity within the spin-fluctuation model was also performed recently, see [176] and references therein.

The issue of the low-temperature behaviour of surface resistance was discussed recently in [85, 27]. The authors of [85, 27] argue that the experimental observation of $\sigma_1 \propto T$ could be explained by the generalized Drude formula $\sigma_1 \propto n_{qp}(T)\tau(T)$ if the quasiparticle density varies as $n_{qp}(T) \propto T$ (as indeed happens for d-wave pairing) and if the *effective quasiparticle scattering time $\tau(T)$ saturates at low T*. However, the pair correlations in the usual impurity scattering models lead to strong T-dependence of the scattering time (neglecting vertex corrections), namely $\tau(T) \propto T$ in unitary limit or $\tau(T) \propto 1/T$ in the Born limit. As claimed in [85, 27], the attempts to resolve this problem in [84] by choosing intermediate scattering rate have not yet provided satisfactory results. Therefore various possible physical mechanisms of the temperature and energy dependence of τ are discussed in [85, 27]: scattering from the 'holes' of the order parameter at impurity cites and scattering from extended defects. These mechanisms may provide the required saturation of $\tau(T)$ at low T. As in [47] the vertex corrections can also modify the low temperature conductivity (3.59), however the temperature dependence has not yet been established. The temperature-dependent quasiparticle–quasiparticle scattering in d-wave superconductors was discussed recently by Walker and Smith [208]. It was claimed that this process gives an explanation of the rapid variation with temperature of the electrical transport relaxation rate in YBCO.

To conclude our discussion of the consequences of the d-wave order parameter symmetry, which is due to the interaction intensity described by an alternating function in the reciprocal space, consider two important points. Firstly, the presence of quasi-one-dimensional sections of the electronic spectrum in HTS and the resulting square-root van-Hove singularities in the density of states [3] lead to d-wave pairing caused by anisotropic electron–phonon coupling. Alternative models of the d-wave order parameter based on the electron–phonon coupling were discussed in [171, 100]. Secondly, the third principle of thermodynamics rules out the linear dependence $\Delta\lambda(T) \propto T$ in the region of very low temperatures, $T \to 0$ [173]. In the case of a superconductor with a d-wave order parameter, this means that there always exists a physical mechanism that gives rise to a crossover temperature $T^* \ll T_c$ below which $\Delta\lambda(T)$ must deviate from a linear function. Up to now, two such mechanisms have been identified, namely impurity scattering [87] and, in pure d-wave superconductors, nonlocal effects [118]. Really, in some microwave experiments the onset of the linear section of the $\Delta\lambda(T)$ curve in the range $T \ll T_c$ was not at 4.2 K, but at slightly higher temperatures (see, for example, curves of $\lambda(T)$ in TBCCO shown by Figure 3.13), but no systematic measurements of $\Delta\lambda(T)$ for $T < 5$ K are presently available.

3.6.3 Two-Band Model and Mixed Symmetry of the Order Parameter

An interpretation of the features in $Z_s(T)$ and $\sigma_s(T)$ curves observed recently in YBCO single crystals [193, 185, 217, 186] can be based on the two-band model and/or the assumption about the mixed symmetry of the order parameter. Even the shapes of experimental curves in Figure 3.33B and C, and function (3.56), which describes these curves and contains two summands, provide evidence in favour of this interpretation. Moreover, the mixed $(s + d)$-wave order parameter has the symmetry of the orthorhombic lattice and seems to be more natural for YBCO than a pure d-wave order parameter, which has the symmetry of the tetragonal lattice.

A description of HTS properties based on the two-band model was suggested by Kresin and Wolf [119]. This model is a generalization of the SC model to the case of layered HTS, in particular YBCO, which has two subsystems, namely the band of CuO_2 planes (S-band) and the band of CuO chains (N-band). The density of states in such a system as a function of temperature and impurity concentration was analyzed by Adrian *et al.* [8].

Calculations of the microwave response [69, 9, 70] assumed strong electron–phonon coupling in the S-band and weak superconductivity in the N-band induced by the proximity effect. A system of coupled Eliashberg equations for the s-wave order parameter and renormalization functions in each band was solved. The parameters in these equations were coupling constants λ_{ij} and coefficients γ_{ij} and γ_{ij}^{M} of scattering from the i-th to j-th band due to nonmagnetic and magnetic impurities, respectively.

In [69, 70] the number and values of parameters were selected using experimental data on YBCO single crystals. For the S-band $\lambda_{11} = 3$, in the N-band $\lambda_{22} = 0$, and the nonvanishing gap in CuO chains is induced by the interband coupling characterized by the parameters $\lambda_{12} = \lambda_{21} = 0.2$. This set of coupling constants yields $T_c \simeq 92$ K. Effects of interband scattering were considered to be negligible: γ_{12}, $\gamma_{21} \ll T_c$. Impurity scattering within each band, γ_{11}, γ_{22}, was taken into account, alongside the scattering by magnetic impurities, $\gamma_{22}^{\mathrm{M}} \equiv \gamma^{\mathrm{M}}$, in the N-band only ($\gamma_{11}^{\mathrm{M}} = 0$), where oxygen atoms have a higher mobility and, leaving the chains, they generate magnetic moments in uncompensated copper ions Cu^{2+}. The parameter γ^{M} is proportional to the concentration of magnetic impurities, whose quantity increases with decreasing oxygen content in the sample. The constants of elastic relaxation were considered to be equal, $\gamma_{11} = \gamma_{22} \equiv \gamma^{\mathrm{imp}}$, and estimated taking the absolute value and anisotropy of YBCO conductivity in the normal state, namely, the estimate $2 \leq \gamma^{\mathrm{imp}}/T_c \leq 4$ derived from the measurement $50 \leq \rho(100\ \mathrm{K}) \leq 100\ \mu\Omega$ cm and the resistivity anisotropy factor in the ab-plane equal to 2. Note that γ^{imp} is not equal to $\Gamma = 1/2\tau(0)$ in the one-band models discussed above. The calculated constants of inelastic scattering were automatically proportional to T^3 [69, 70], since the Debye phonon spectrum was used and vertex corrections were neglected. Thus the large set of parameters initially included in the Eliashberg equations for the two-band model reduced to four numbers λ_{11}, λ_{12}, γ^{imp}, and γ^{M}, two of which ($\lambda_{11} = 3$ and $\lambda_{12} = 0.2$) were constant, whereas γ^{imp} and γ^{M} varied.

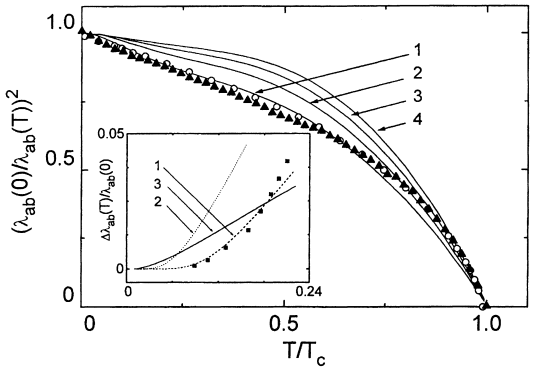

Figure 3.39 Comparison between calculated curves ($\gamma^{\rm M} = 0.2T_c$) of $\sigma_2(T)/\sigma_2(0)$ and experimental data from [134] (triangles) and [32] (circles): (1) $\gamma^{\rm imp} = 2T_c$; (2) $\gamma^{\rm imp} = 4T_c$; (3) $\gamma^{\rm imp} = 8T_c$, (4) $\gamma^{\rm imp} = 20T_c$. The inset ($\gamma^{\rm imp} = 2T_c$) demonstrates a cross-over from the exponential (curves 1, $\gamma^{\rm M} = 0$, and 2, $\gamma^{\rm M} = 0.1T_c$) to linear (curve 3, $\gamma^{\rm M} = 0.4T_c$) curve of $\Delta\lambda_{ab}(T)$ due to increasing concentration of magnetic impurities. Squares in the inset plot data from [112].

Figure 3.39 shows calculations and measurements given in [134] and [32] (Figure 3.33A) of the function $\sigma_2(T)/\sigma_2(0)$. For all curves (1–4) $\gamma^{\rm M} = 0.2T_c = {\rm const}$, and the only parameter varying from one curve to another is $\gamma^{\rm imp}$: $2T_c$ (1), $4T_c$ (2), $8T_c$ (3), and $20T_c$ (4). The effect of magnetic impurity scattering (depending on the content of oxygen in YBCO) is demonstrated by the inset to Figure 3.39 and can be described as follows. In a sample saturated with oxygen, there are no magnetic scatterers in the chains (N-band), $\gamma^{\rm M} = 0$. In this case, the calculation by the two-band model (curve 1 in the inset) and the experimental data (■) obtained using a YBCO thin film [112] yield an exponential temperature dependence $\Delta\lambda_{ab}(T)$ for $T \ll T_c$, owing to the small width of the energy gap induced in the N-band.

Note that an exponential dependence $\Delta\lambda(T)$ has been detected in the experiment [112] with well oxygenated epitaxial YBCO films, which degraded very rapidly [83], and in strained YBCO films on CeO_2-buffered sapphire substrates [81]. No such behaviour has been observed in the best HTS crystals. The thermally activated behaviour of $\sigma_s(T)$ and $R_s(T)$ is incompatible with a pure d-wave symmetry of the order parameter.

A light doping with magnetic impurities ($\gamma^{\rm M} = 0.1T_c$, curve 2 in the inset to Figure 3.39) leads to a large slope of $\Delta\lambda_{ab}(T)$, but does not radically change the curve shape. A further increase in $\gamma^{\rm M}$ (depletion of oxygen) makes the superconducting state in the chains gapless, and the function $\Delta\lambda_{ab}(T)$ becomes linear in the temperature range $T > 0.05T_c \approx 5$ K. A linear section of the $\Delta\lambda_{ab}(T)$ curve in the low temperature range is also shown in Figure 3.6, where the curve calculated on the base of the model under discussion ($\gamma^{\rm M} = 0.3T_c$, $\gamma^{\rm imp} = 4T_c$) is compared to measurements of a YBCO thin film at a frequency of 87 GHz [154]. At a sufficiently high $\gamma^{\rm imp}$, the contribution of the N-band to the field penetration depth vanishes, and

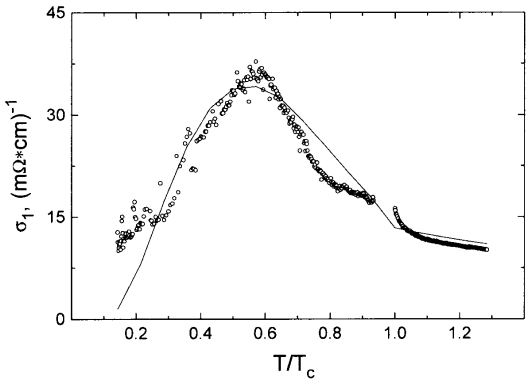

Figure 3.40 Solid line: temperature dependence of the real part of the conductivity σ_1/σ_n calculated by the two-band model with $\gamma_{22}^s = 0$, $\gamma_{11} = \gamma_{22} = 6$ meV. Open circles: experimental data from [154].

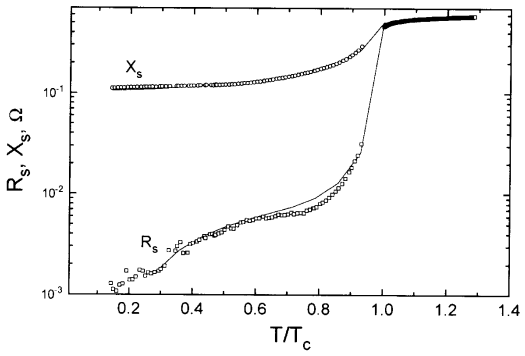

Figure 3.41 Comparison of the temperature dependence of the surface impedance (solid lines) calculated by the two-band model ($\gamma_{22}^s = 0$, $\gamma_{11} = \gamma_{22} = 6$ meV) with experimental data from [154]. Open squares are the real (R_s) and open circles are the imaginary (X_s) parts of the impedance.

the function $\Delta\lambda(T)$ becomes close to that predicted by the SC model: $\Delta\lambda(T) \propto T^n$ with the exponent $n > 2$ [116, 52]. A crossover from a linear $\Delta\lambda(T)$ to a power function with $n = 4$ with increasing impurity concentration was observed in [187] with YBCO crystals with some Y atoms replaced by Pr ions.

The complex conductivity $\sigma_s = \sigma_1 - i\sigma_2$ of a two-band superconductor is a combination of conductivities in the S-band ($\sigma_s^S = \sigma_1^S - i\sigma_2^S$) and N-band ($\sigma_s^N = \sigma_1^N - i\sigma_2^N$):

$$\sigma_s = \sigma_s^S + \zeta\sigma_s^N, \quad \zeta = \frac{\nu^S m^N}{\nu^N m^S}, \tag{3.62}$$

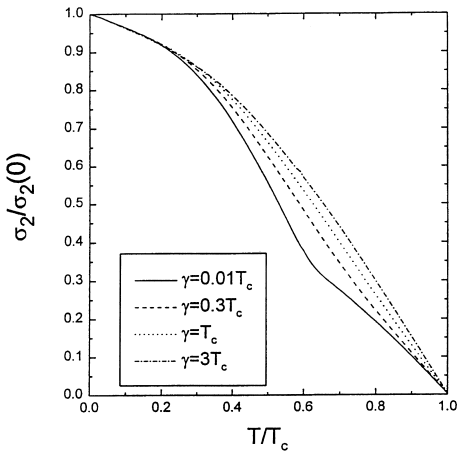

Figure 3.42 Evolution of $\sigma_2(T)/\sigma_2(0)$ curves due to changes in the interband scattering constant γ. Calculations are made by the two-band model with a d-wave order parameter in the S-band and an s-wave order parameter in the N-band [72].

where $\nu^{S,N}$ and $m^{S,N}$ are the densities of states and effective masses of carriers in the respective bands. Numerical calculations of $\sigma_1(T)$ and $Z_s(T)$ shown in Figures 3.40 and 3.41 were performed in [70] and are in satisfactory agreement with measurements of YBCO films [154], although these data have not been carefully analyzed as yet in the range of low temperatures and near T_c. Physically the emergence of the maximum in $\sigma_1(T)$ in the present model is due to interplay between strong T-dependent scattering and T-dependent quasiparticle number in the N-band. An additional physical mechanism, which contributes to the maximum of $\sigma_1(T)$, is the presence of the coherence factors in the N-band since the electron–phonon interaction in this band is weak.

Even though the two-band model has its uncontested advantages, attempts to apply it to the microwave response of tetragonal HTS single crystals is problematic since, unlike YBCO, they contain no chains and, therefore, no magnetic scatterers like Cu^{2+} ions in YBCO. Meanwhile, magnetic impurities play an essential role: scattering by these impurities reduces the gap in the N-band to zero and leads to the linear temperature dependence of $\Delta\lambda_{ab}$ for $T \ll T_c$. There is no such problem with d-wave superconductors. Moreover, it seems that the experimental curves of $Z_s(T)$ and $\sigma_s(T)$ in YBCO in the intermediate temperature range cannot be interpreted in terms of s-pairing in both bands. Therefore, an option with a d-wave order parameter in one of the bands turns up as a matter of course. An attempt to introduce such an order parameter was made in [72], and the results of calculations of $\sigma_2(T)/\sigma_2(0)$ are plotted in Figure 3.42. The curves were calculated using a two-band model with a d-wave superconducting gap in the S-band and s-wave symmetry in the N-band. The model parameters were $\lambda_{11} = 3$, $\lambda_{22} = 0.5$, $\zeta = 0.5$ in (3.62), and only

the constants of interband scattering $\gamma_{12} = \gamma_{21} \equiv \gamma$ were included. The solid line in Figure 3.42 shows a feature at $T \approx 0.6T_c$, which vanishes as the disorder increases. A similar approach was employed by Srikanth *et al*. [186] in interpreting their experimental data, in particular, for the phenomenological description of the curve in Figure 3.33C.

Recently microwave properties of HTS materials have been attracting more attention of researchers [41, 46, 108, 24, 160, 149, 49, 152] because of intriguing effects that are tentatively attributed to the mixed $(s + d)$-wave symmetry of the order parameter. Most studies were concentrated on the low temperature variation of the London penetration depth in superconductors having a mixed symmetry order parameter. In particular, it was shown in [149] that the low temperature properties of $\lambda(T)$ can be used to distinguish between a pure d-wave order parameter or a $(s+id)$-one having a small subdominant s-wave contribution in systems with a tetragonal lattice. Moreover, an addition of impurities suppresses the d-wave symmetric part to the benefit of the s-wave one. As a result, a variety of low-temperature dependences is possible for various impurity concentration, which allows in principle to determine whether the order parameter of a superconductor with an orthorhombic lattice is $(s+id)$ symmetric or $(s+d)$ symmetric [25]. In [24] the $(d+s)$-model was generalized in order to take into account the normal state anisotropy. This is the realistic approach to the high-T_c cuprates with an orthorhombic distortion since recent microwave conductivity data suggest that substantial portion of the ab-anisotropy of $\lambda(T)$ is a normal state effect. It was shown that such an anisotropy reacts not only on the ab-anisotropy in the transport coefficients but also on the density of states and other thermodynamic quantities. The possible temperature variation of the penetration depth $\lambda(T)$ was analyzed recently in [152] in the framework of the $(d+s)$-model of hybrid pairing. The slope of the $\Delta\lambda(T) \propto T$ for $T \ll T_c$ and its dependence on the Δ_s/Δ_d admixture in the gap function was analyzed quantitatively taken into account the impurity scattering, while the quantitative comparison of the model with the experimental data was not yet performed. More interesting discoveries in this field of research can be expected in the immediate future.

3.7 CONCLUSION

We have presented a summary of measurements of the surface impedance $Z_s(T) = R_s(T) + iX_s(T)$ in the ab-plane of high-quality YBCO, BSCCO, TBCCO, and TBCO single crystals in the temperature range $4.2 \leq T \leq 150$ K and of their present theoretical interpretations. For the frequencies $\lesssim 10$ GHz, the common features of all these materials are the linear temperature dependence of the surface resistance $(\Delta R_s(T) \propto T)$ and of the surface reactance $(\Delta X_s(T) \propto \Delta\lambda_{ab}(T) \propto T)$ at temperatures $T \ll T_c$, their rapid growth as $T \to T_c$, and their behaviour in the normal state corresponding to a linear T-dependence of $\Delta\rho_{ab}(T)$, with $R_s(T) = X_s(T) = \sqrt{\omega\mu_0\rho(T)/2}$ (with possible exception of TBCO crystals). There are differences between the T–dependence of $Z_s(T)$ in BSCCO, TBCCO, or TBCO single crystals with tetragonal lattices and in YBCO crystals with an orthorhombic lattice. The lin-

ear resistivity region extends to near $T_c/2$ for the tetragonal materials and terminates near or below $T < T_c/3$ for YBCO. At higher temperature, $R_s(T)$ of YBCO has a broad peak. In addition, the $\lambda_{ab}(T)$ curves of some YBCO single crystals have unusual features in the intermediate temperature range.

We have also presented an analysis of the existing microscopic theories of the high-frequency response of HTS materials. We argue that there is no microscopic theory explaining the temperature dependence of $Z_s(T)$ for different HTS's, whereas these data are well described by a phenomenological modified two-fluid model, which takes into account scattering of quasiparticles and characteristic changes in the density of superconducting carriers at low temperatures and in the vicinity of the critical temperature. The underlying ideas of this model may be essential for a future microscopic model of the microwave response of HTS materials.

Only microwave properties of HTS crystals of the highest quality and with optimal doping levels have been discussed, because large amount experimental data concerning these materials has been accumulated by this time. For this reason, we have set aside three issues, which are, in our opinion, quite important and worth mentioning at the end of this review.

Firstly, the explanation of the nature of the residual microwave losses, which determine the behaviour of the real part of conductivity $\sigma_1(T)$ at $T < T_c$, has remained a topical problem in the HTS physics.

Some researchers (e.g., Hein *et al.* [81]) attributed these losses to the presence of a fraction n_0 of carriers that remain unpaired at $T = 0$. The magnitude of $R_{\rm res}$ was estimated by the first formula of (3.17) with the nonzero conductivity $\sigma'(0) = n_0 e^2 \tau(0)/m$ from (3.9). One can easily prove, however, that this approach requires that the calculations of $R_{\rm res}$ should satisfy inequality (3.46). If the latter condition is not met, which may occur in HTS crystals, as was shown previously (see, e.g., Figure 3.35), the number n_0 should be larger than the entire concentration n of the carriers.

The effect of the sample surface conditions on the $Z_s(T)$ signal has not been studied experimentally, although there are several phenomenological [77, 163, 207, 138, 140, 96, 204, 82] and microscopic [136, 189, 20, 21, 61, 68] models indicating the importance of such studies. For example, the theory [68] predicts that in the case of diffuse scattering on the surface, an s-wave component can be added to the bulk d-wave order parameter in the region near the sample surface. A comprehensive review of various manifestations of the surface bound states in unconventional superconductors is given recently by Kashivaya and Tanaka [106]. In developing the traditional approach to the problem, which attributed the residual surface resistance to various imperfections of the surface, the researchers took account of the losses due to weak links [86, 162, 76], twinning planes [76, 205], clusters with normal conductivity [206], etc. Numerical estimates, however, indicate that the contributions of these mechanisms to the residual surface resistance are much smaller than the measured $R_{\rm res}$ in HTS materials. Moreover, a very remarkable fact is that the residual surface resistance measured at a frequency of 10 GHz was approximately the same, $R_{\rm res} \sim 100\ \mu\Omega$, in all high-quality copper-oxide HTS crystals of different chemical compositions and fabricated by different methods, irrespective of

whether they contained twinning planes or not, and whether measurements were performed on freshly cleaved or as-grown surfaces. This fact, apparently, indicates that the residual losses are inherent in all high-quality HTS crystals, and their origin is in the features of their structure, namely, in its conspicuously layered nature [191].

Secondly, the evolution of the temperature dependence $Z_s(T)$ with changes in the doping level from the optimal value has not been studied sufficiently. No microwave measurements of one and the same crystal but with a variable and controlled carrier concentration are available. At the same time, such data are essential for theoretical studies aimed at creating a microscopic theory of HTS, because they would shed light on such problems as possible changes in the order parameter symmetry [156, 129], evolution of the pseudogap [95, 155, 211], superconductor-dielectric transition [63], etc.

Thirdly, measurements of the surface impedance anisotropy, which have been scarce by now, have not been discussed, although several experiments have provided evidence in favour of different temperature dependences of the surface impedance in the ab-plane and along the c-axis [134, 97, 179, 175, 30, 110, 181, 110, 31, 188, 92, 191, 109, 62]. The theory [115, 69, 70, 19, 4, 166, 213, 90] predicts different scenarios for processes in HTS in the microwave band, depending on the mechanism responsible for the anisotropy, and therefore a comparison between theoretical data and accurate microwave measurements would, undoubtedly, be very helpful.

The solutions to the problems listed above will probably determine the development of experimental and theoretical research of the microwave response of HTS materials in the immediate future and that will result in a universal approach to microwave properties of HTS.

ACKNOWLEDGMENTS

We are grateful to our co-authors O. V. Dolgov, H. J. Fink, Yu. A. Nefyodov, D. V. Shovkun, S. V. Shul'ga, A. T. Sokolov, G. E. Tsydynzhapov, A. A. Zhukov, L. A. Klinkova, N. V. Barkovskii, G. A. Emel'chenko, I. G. Naumenko, and N. N. Kolesnikov for their help and contribution to this work on different stages. Helpful discussions with V. F. Gantmakher, E. G. Maksimov, G. M. Eliashberg, A. Agliolo-Gallitto, N. Bontemps, M. T. Beal-Monod, A. Buzdin, R. Combescot, J. Halbritter, M. Li Vigni, K. Scharnberg, and S. Sridhar are also acknowledged. This research has been supported by the Russian Foundation for Basic Research (grants 00-02-17053 and 00-02-04021) and Scientific Council on Superconductivity (project 96060), and in part by the Program for Russian–Dutch Research Cooperation (NWO), Collaborative Linkage Grant NATO, and by the Centre National de la Recherche Scientifique — Russian Academy of Sciences co-operation program 4985.

REFERENCES

1. E. Abrahams, 1996, *J. Phys. I France*, **6**, 2191.
2. A. A. Abrikosov, 1988, *Fundamentals of the Theory of Metals*, (Elsevier Science Ltd).
3. A. A. Abrikosov, 1993, *Physica C*, **214**, 107; 1994, **222**, 191; 1995, **244**, 243.
4. A. A. Abrikosov, 1996, *Physica C*, **258**, 53.
5. A. A. Abrikosov, 1995, *Phys. Rev. B*, **51,** 11 955.
6. A. A. Abrikosov, L. P. Gor'kov and I. M. Khalatnikov, 1958, *Zh. Exp. Teor. Fiz.*, **35**, 265 (1959, *JETP*, **8**, 182).
7. D. Achir, M. Poirier, D. A. Bonn, R. Liang and W. N. Hardy, 1993, *Phys. Rev. B*, **48**, 13184.
8. S. D. Adrian, S. A. Wolf, O. Dolgov, S. Shulga and V. Z. Kresin, 1997, *Phys. Rev. B*, **56**, 7878.
9. S. D. Adrian, M. E. Reeves, S. A. Wolf and V. Z. Kresin, 1995, *Phys. Rev. B*, **51**, 6800.
10. A. S. Alexandrov and N. F. Mott, 1994, *Rep. Prog. Phys.*, **57**, 1197.
11. J. L. Altman, 1964, *Microwave Circuits*, (D. van Nostrand Company, Princeton).
12. P. W. Anderson, 1991, *Physica C*, **185–189**, 11.
13. P. W. Anderson, 1987, *Science*, **235,** 1196.
14. A. Andreone, C. Cantoni, A. Cassinese, A. Di Chiara, and R. Vaglio, 1997, *Phys. Rev. B*, **56**, 7874.
15. O. K. Andersen, A. I. Lichtenstein, O. Rodriquez, *et al.*, 1991, *Physica C*, **185-189,** 147.
16. S. M. Anlage, J. Mao, J. C. Booth, D. H. Wu and J. L. Peng, 1996, *Phys. Rev. B*, **53**, 2792.
17. J. Annett, N. Goldenfeld, and A. Leggett, 1996, In *Physical Properties of High Temperature Superconductors V*, edited by D. M. Ginsberg, (World Scientific, Singapore), p. 83.
18. J. F. Annett, N. D. Goldenfeld and S. R. Renn, 1991, *Phys. Rev. B*, **43**, 2778.
19. W. A. Atkinson and J. P. Carbotte, 1995, *Phys. Rev. B*, **52**, 10601; 1997, **55**, 12748.
20. S. R. Bahkal, 1996, *Phys. Rev. Lett.*, **76**, 3634.
21. Yu. S. Barash, A. A. Svidzinsky and H. Burkhardt, 1997, *Phys. Rev. B*, **55**, 15282.
22. J. Bardeen, L. N. Cooper and J. R. Schrieffer, 1957, *Phys. Rev.*, **108**, 1175.
23. B. Battlog, 1991, *Phys. Today*, **44**, 44.
24. M. T. Beal-Monod and K. Maki, 1995, *Phys. Rev. B*, **52**, 13576; 1996, **53**, 5775; 1997, **55**, 1194.
25. M. T. Beal-Monod, 1998, *Phys. Rev. B*, **58**, 8830; 1998, *Physica C*, **298**, 59.
26. M. Benkraouda and J. R. Clem, 1996, *Phys. Rev. B*, **53**, 5716.
27. A. J. Berlinsky, D. A. Bonn, R. Harris and C. Kallin, 2000, *Phys. Rev. B*, **61**, 9088.
28. J. Betouras and R. Joynt, 1995, *Europhys. Lett.*, **31**, 119.

29. A. Bille and K. Scharnberg, 1998, *J. Phys. Chem. Solids*, **59**, 2110.
30. D. A. Bonn, P. Dosanjh, R. Liang and W. N. Hardy, 1992, *Phys. Rev. Lett.*, **68**, 2390.
31. D. A. Bonn, S. Kamal, K. Zhang, R. Liang and W. N. Hardy, 1995, *J. Phys. Chem. Solids*, **56**, 1941.
32. D. A. Bonn, S. Kamal, K. Zhang, R. Liang, D. J. Baar, E. Klein and W. N. Hardy, 1994, *Phys. Rev. B*, **50**, 4051.
33. D. A. Bonn, R. Liang, T. M. Riseman, D. J. Baar, D. C. Morgan, K. Zhang, P. Dosanjh, T. L. Duty, A. MacFarlane, G. D. Morris, J. H. Brewer, W. N. Hardy, C. Kallin and A. J. Berlinsky, 1993, *Phys. Rev. B*, **47**, 11314.
34. D. A. Bonn and W. N. Hardy, In *Physical Properties of High Temperature Superconductors V*, edited by D. M. Ginsberg, (World Scientific, Singapore, 1995), pp. 7–97.
35. D. M. Broun, D. C. Morgan, R. J. Ormeno, S. F. Lee, A. W. Tyler, A. P. Mackenzie and J. R. Waldram, 1997, *Phys. Rev. B*, **56**, R11443.
36. J. P. Carbotte and C. Jiang, 1993, *Phys. Rev. B*, **48**, 4231.
37. J. C. Carbotte, 1990, *Rev. Mod. Phys.*, **62**, 1027.
38. J. Chang and D. J. Scalapino, 1989, *Phys. Rev. B*, **40**, 4299.
39. E. P. Cohen, 1994, *Computers in Physics*, **8**, 34.
40. R. T. Collins, Z. Schlesinger, F. Holtzberg, C. Field, U. Welp, G. W. Crabtree, J. Z. Liu and Y. Fang, 1991, *Phys. Rev. B*, **43**, 3701.
41. R. Combescot and X. Leyronas, 1995, *Phys. Rev. Lett.*, **75**, 3732.
42. E. Dagotto, 1994, *Rev. Mod. Phys.*, **66**, 763.
43. S. Djordjevich, L. A. de Vaulchier, N. Bontemps, J. P. Vieren, Y. Guldner, S. Moffat, J. Preston, X. Castel, M. Guilloux-Viry and A. Perrin, 1998, *Eur. Phys. J. B*, **5**, 847.
44. O. V. Dolgov and S. V. Shulga, 1995, *J. Supercond.*, **8**, 611.
45. O. V. Dolgov, E. G. Maksimov, A. E. Karakozov and A. A. Mikhailovsky, 1994, *Solid State Comm.*, **89**, 827.
46. C. O' Donovan and J. P. Carbotte, 1995, *Phys. Rev. B*, **52**, 4568; 1997 **55**, 8520.
47. A. C. Durst and P. A. Lee, 2000, *Phys. Rev. B*, **62**, 1270.
48. R. C. Dynes, *Sol. St. Comm.*, 1994, **92**, 53.
49. D. Einzel and I. Schürrer, 1999, *J. Low Temp. Phys.* **117**, 15.
50. G. M. Eliashberg, 1960, *Zh. Exp. Teor. Fiz.*, **38**, 966 (1960, *JETP*, **11**, 696).
51. G. M. Eliashberg, 1960, *Zh. Exp. Teor. Fiz.* **39**, 1437 (1961, *JETP*, **12**, 1000).
52. G. M. Eliashberg, G. V. Klimovich and A. V. Rylyakov, 1991, *J. Supercond.*, **4**, 393.
53. V. J. Emery, 1994, *Nature*, **370**, 593.
54. A. Erb, E. Walker and R. Flükiger, 1996, *Physica C*, **258**, 9.
55. E. Farber, G. Deutscher, J. P. Contour and E. Jerby, 1998, *Eur. Phys. J. B*, **5**, 159.
56. H. J. Fink, 1998, *Phys. Rev. B*, **58**, 9415.
57. H. J. Fink, 2000, *Phys. Rev. B*, **61**, 6346.
58. H. J. Fink and M. R. Trunin, 2000, *Physica B*, **284–288**, 923.
59. H. J. Fink and M. R. Trunin, 2000, *Phys. Rev. B*, **62**, 3046.

60. D. S. Fisher, M. P. A. Fisher and D. A. Huse, 1991, *Phys. Rev. B*, **43**, 130.
61. M. Fogelström, D. Rainer and J. A. Sauls, 1997, *Phys. Rev. Lett.*, **79**, 281.
62. M. B. Gaifullin, Y. Matsuda, N. Chikumoto, J. Shimoyama, K Kishio and R. Yoshizaki, 1999, *Phys. Rev. Lett.*, **83**, 3928.
63. V. F. Gantmakher, L. P. Kozeeva, A. N. Lavrov, D. A. Pushin, D. V. Shovkun and G. E. Tsydynzhapov, 1997, *Pis'ma Zh. Exp. Teor. Fiz.*, **65**, 834, (*JETP Lett.*, **65**, 870).
64. V. L. Ginzburg and L. D. Landau, 1950, *Zh. Exp. Teor. Fiz.*, **20**, 1064.
65. V. L. Ginzburg, 1964, *Phys. Lett.*, **13**, 101.
66. V. L. Ginzburg and E. G. Maksimov, 1992, *Sverkhprovodimost': Fiz., Khim., Tekh.*, **5**, 1543.
67. N. E. Glass and W. F. Hall, 1991, *Phys. Rev. B*, **44**, 4495.
68. A. A. Golubov and M. Yu. Kupriyanov, 1999, *Pis'ma Zh. Exp. Teor. Fiz.*, **69**, 242, (1999, *JETP Lett.* **69**, 262).
69. A. A. Golubov, M. R. Trunin, A. A. Zhukov, O. V. Dolgov and S. V. Shulga, 1995, *Pis'ma Zh. Exp. Teor. Fiz.*, **62**, 477, (1995, *JETP Lett.*, **62**, 496).
70. A. A. Golubov, M. R. Trunin, A. A. Zhukov, O. V. Dolgov and S. V. Shulga, 1996, *J. Phys. I France*, **6**, 2275.
71. A. A. Golubov, M. R. Trunin, S. V. Shulga, D. Wehler, J. Dreibholz, G. Müller and H. Piel, 1993, *Physica C*, **213**, 139.
72. A. A. Golubov and M. R. Trunin, unpublished.
73. C. S. Gorter and H. Casimir, 1934, *Phys. Z.*, **35**, 963.
74. B. Goss Levi, 1996, *Physics Today*, **49,** 19.
75. N. Hakim, Yu. A. Nefyodov, S. Sridhar and M. R. Trunin, unpublished.
76. J. Halbritter, 1990, *J. Appl. Phys.*, **68**, 6315; 1992, **71**, 339.
77. J. Halbritter, 1992, *J. Supercond.*, **5**, 171; 1992, **5**, 331; 1995, **8**, 691.
78. W. N. Hardy, D. A. Bonn, D. C. Morgan, R. Liang and K. Zhang, 1993, *Phys. Rev. Lett.*, **70**, 3999.
79. D. J. van Harlingen, 1995, *Rev. Mod. Phys.*, **67,** 515.
80. M. Hasegawa, Y. Matsushita and H. Takei, 1996, *Physica C*, **267**, 31.
81. M. Hein, T. Kaiser and G. Müller, 2000, *Phys. Rev. B*, **61**, 640.
82. M. Hein, 1999, In *High-Temperature-Superconductor Thin Films at Microwave Frequencies*, Vol. 155, *Springer Tracts of Modern Physics* (Springer, Heidelberg, 1999).
83. M. Hein, 1996, In *Studies of High Temperature Superconductors*, edited by A. Narlikar, Vol. 18, (Nova Sciences, New York, 1996), pp. 141–216.
84. S. Hensen, G. Müller, C. T. Rieck and K. Scharnberg, 1997, *Phys. Rev. B*, **56**, 6237.
85. M. H. Hettler and P. J. Hirschfeld, 2000, *Phys. Rev. B*, **62**, 9054.
86. T. L. Hilton and M. R. Beasly, 1989, *Phys. Rev. B*, **39**, 9042.
87. P. J. Hirschfeld and N. Goldenfeld, 1993, *Phys. Rev. B*, **48**, 4219.
88. P. J. Hirschfeld, W. O. Putikka and D. J. Scalapino, 1993, *Phys. Rev. Lett.*, **71**, 3705.
89. P. J. Hirschfeld, W. O. Putikka and D. J. Scalapino, 1994, *Phys. Rev. B*, **50**, 4051.

90. P. J. Hirschfeld, S. M. Quinlan and D. J. Scalapino, 1997, *Phys. Rev. B*, **55**, 12742.
91. A. Hosseini, R. Harris, S. Kamal, P. Dosanjh, J. Preston, R. Liang, W. N. Hardy and D. A. Bonn, 1999, *Phys. Rev. B*, **60**, 1349.
92. A. Hosseini, S. Kamal, D.A. Bonn, R. Liang and W. N. Hardy, 1998, *Phys. Rev. Lett.*, **81**, 1298.
93. M. L. Horbach, W. van Saarlos and D. A. Huse, 1991, *Phys. Rev. Lett.*, **67**, 3464.
94. M. V. Indenbom and E. H. Brandt, 1994, *Phys. Rev. Lett.*, **73**, 1731.
95. Yu. A. Izyumov, 1997, *Uspekhi Fiz. Nauk*, **167**, 465; 1999, **169**, 225.
96. T. Jacobs, K. Numssen, R. Schwab, R. Heidinger and J. Halbritter, 1997, *IEEE Trans. Appl. Supercond.*, **7**, 1917.
97. T. Jacobs, S. Sridhar, Q. Li, G. D. Gu and N. Koshizuka, 1995, *Phys. Rev. Lett.*, **75**, 4516.
98. T. Jacobs, S. Sridhar, C. T. Rieck, K. Scharnberg, T. Wolf and J. Halbritter, 1995, *J. Phys. Chem. Solids*, **56**, 1945.
99. R. O. Jones and O. Gunnarson, 1989, *Rev. Mod. Phys.* **61,** 689.
100. H. Kamimura, S. Matsuno, Y. Suwa and H. Ushio, 1996, *Phys. Rev. Lett.*, **77**, 723.
101. A. E. Karakozov, E. G. Maksimov and S. A. Mashkov, 1975, *Zh. Exp. Teor. Fiz.* **68**, 1937 (1976, *JETP*, **41**, 971).
102. A. E. Karakozov, E. G. Maksimov and A. A. Mikhailovskii, 1992, *Zh. Exp. Teor. Fiz.* **102**, 132 (1992, *JETP*, **75** (1), 70).
103. S. Kamal, R. Liang, A. Hosseini, D. A. Bonn and W. N. Hardy, 1998, *Phys. Rev. B*, **58**, 8933.
104. S. Kamal, D. A. Bonn, N. Goldenfeld, P. J. Hirschfeld, R. Liang and W. N. Hardy, 1994, *Phys. Rev. Lett.*, **73**, 1845.
105. A. P. Kampf, 1994, *Phys. Reports*, **249**, 219.
106. S. Kashiwaya and Y. Tanaka, 2000, *Rep. Prog. Phys.* **63**, 1641.
107. H. Kierspel, H. Winkelmann, T. Auweiler, W. Schlabitz, B. Büchner, V. H. M. Duijn, N. T. Hein, A. A. Menovsky and J. J. M. Franse, 1996, *Physica C*, **262**, 177.
108. H. Kim and E. J. Nicol, 1995, *Phys. Rev. B*, **52**, 13576.
109. H. Kitano, T. Hanaguri and A. Maeda, 1998, *Phys. Rev. B*, **57**, 10946.
110. H. Kitano, T. Shibauchi, K. Uchinokura, A. Maeda, H. Asaoka and H. Takei, 1995, *Phys. Rev. B*, **51**, 1401.
111. O. Klein, E. J. Nicol, K. Holczer and G. Grüner, 1994, *Phys. Rev. B*, **50**, 6307.
112. N. Klein, N. Tellmann, H. Schulz, K. Urban, S. A. Wolf and V. Z. Kresin, 1993, *Phys. Rev. Lett.*, **71**, 3355.
113. O. Klein, S. Donovan, M. Dressel and G. Grüner, 1993, *Int. J. Infrared Millimeter Waves*, **14**, 2423, 2459, 2489.
114. R. A. Klemm, 1994, *Phys. Rev. Lett.*, **73**, 1871.
115. R. A. Klemm and S. H. Liu, 1995, *Phys. Rev. Lett.*, **74**, 2343.
116. G. V. Klimovich, A. V. Rylyakov and G. M. Eliashberg, 1991, *Pis'ma Zh. Exp. Teor. Fiz.* **53**, 381 (1991, *JETP Lett.*, **53**, 399).

117. N. N. Kolesnikov, M. P. Kulakov, Yu. A. Osipyan and S. A. Shevchenko, 1991, *Sverkhprovodimost': Fiz., Khim., Tekh.*, **4**, 957.
118. I. Kosztin and A. J. Leggett, 1997, *Phys. Rev. Lett.*, **79**, 135.
119. V. Z. Kresin and S. A. Wolf, 1990, *Phys. Rev. B*, **41**, 4278; 1992, **46**, 6458; 1995, **51**, 1229.
120. L. D. Landau and E. M. Lifshitz, 1984, *Electrodynamics of Continuous Media* (Pergamon, Oxford).
121. P. A. Lee, 1993, *Phys. Rev. Lett.*, **71**, 1887.
122. S-F. Lee, D. C. Morgan, R. J. Ormeno, D. M. Broun, R. A. Doyle and J. R. Waldram, 1996, *Phys. Rev. Lett.*, **77**, 735.
123. Q. P. Li, E. C. Koltenbah and R. Joynt, 1993, *Phys. Rev. B*, **48**, 437.
124. R. Liang, D. A. Bonn and W. N. Hardy, 1998, *Physica C*, **304**, 105.
125. R. Liang, P. Dosanjh, D. A. Bonn, D. J. Baar, J. F. Carolan and W. N. Hardy, 1992, *Physica C*, **195**, 51.
126. W. A. Littl, 1964, *Phys. Rev.*, **134**, A1516.
127. M. Liu, D. Y. Xing and Z. D. Wang, 1997, *Phys. Rev. B*, **55**, 3181.
128. C. J. Lobb, 1987, *Phys. Rev. B*, **36**, 3930.
129. V. M. Loktev, 1996, *Fizika Nizkikh Temperatur*, **22**, 3.
130. F. London and H. London, 1935, *Proc. Roy. Soc.*, **A149**, 71; 1935, **A152**, 24.
131. E. G. Maksimov, 2000, *Uspekhi Fiz. Nauk*, **170**, 1033.
132. K. Maki and H. Won, 1996, *J. Phys. I France*, **6**, 2317.
133. J. Mao and S. Anlage, *Theory of Surface Impedance of Superconductors in a Resonant Cavity*, unpublished.
134. J. Mao, D. H. Wu, J. L. Peng, R. L. Greene and S. M. Anlage, 1995, *Phys. Rev. B*, **51**, 3316.
135. F. Marsiglio, 1991, *Phys. Rev. B*, **44,** 5373.
136. M. Matsumoto and H. Shiba, 1995, *J. Phys. Soc. of Japan*, **64**, 3384.
137. D. C. Mattis and J. Bardeen, 1958, *Phys. Rev.*, **111**, 412.
138. M. Mahel, 1996, *Solid State Comm.*, **97**, 209.
139. Z. Ma, R. C. Taber, L. W. Lombardo, A. Kapitulnik, M. R. Beasley, P. Merchant, C. B. Eom, S. Y. Hou and J. M. Phillips, 1993, *Phys. Rev. Lett.*, **71**, 781.
140. J. McDonald and J. R. Clem, 1997, *Phys. Rev. B*, **56**, 14723.
141. C. Meingast, B. Blank, H. Bürkle, B. Obst, T. Wolf, H. Wühl, V. Selvamanickam and K. Salama, 1990, *Phys. Rev. B*, **41**, 11299.
142. C. Meingast, O. Kraut, T. Wolf, H. Wühl, A. Erb and G. Müller-Vogt, 1991, *Phys. Rev. Lett.*, **67**, 1634.
143. C. Meingast, A. Junod and E. Walker, 1996, *Physica C*, **272**, 106.
144. A. A. Mikhailovsky, S. V. Shulga, A. E. Karakozov, O. V. Dolgov and E. G. Maksimov, 1991, *Solid State Comm.*, **80**, 511.
145. A. Millis, H. Monien and D. Pines, 1990, *Phys. Rev. B*, **42**, 167.
146. R. Micnas, 1990, *Rev. Mod. Phys.* **62**, 113.
147. H. Monien, P. Monthoux and D. Pines, 1991, *Phys. Rev. B*, **43**, 275.
148. P. Monthoux, A. Balatsky and D. Pines, 1992, *Phys. Rev. B*, **46**, 14803.
149. R. Modre, I. Schürrer and E. Schachinger, 1998, *Phys. Rev. B*, **57**, 5496.

150. K. A. Musaelian, J. Betouras, A. V. Chubukov and R. Joynt, 1996, *Phys. Rev. B*, **53**, 3598.
151. S. B. Nam, 1967, *Phys. Rev.*, **156**, 470, 487.
152. Yu. A. Nefyodov, A. A. Golubov, M. R. Trunin and M. T. Beal-Monod, 2000, *Physica B*, **284–288**, 919.
153. H. K. Olsson and R. H. Koch, 1992, *Phys. Rev. Lett.*, **68**, 2406.
154. S. Orbach-Werbig, A. A. Golubov, S. Hensen, G. Müller and H. Piel, 1994, *Physica C*, **235–240**, 2383.
155. S. G. Ovchinnikov, 1997, *Uspekhi Fiz. Nauk*, **167**, 1043.
156. E. A. Pashitskii and V. I. Pentegov, 1997, *Zh. Exp. Teor. Fiz.*, **111**, 298 (1997, *JETP*, **84**, 164).
157. W. E. Pickett, 1989, *Rev. Mod. Phys.*, **61,** 433.
158. W. E. Pickett, H. Krakauer, R. E. Cohen and D. J. Singh, 1992, *Science*, **255**, 46.
159. A. B. Pippard, 1953, *Proc. Roy. Soc.*, **A216**, 547.
160. S. V. Pokrovsky and V. L. Pokrovsky, 1996, *Phys. Rev. B*, **54**, 13275.
161. A. Porch, M. J. Lancaster and R. G. Humphreus, 1995, *IEEE Trans. MTT*, **43**, 306.
162. A. M. Portis and D. W. Cooke, 1992, *Supercond. Sci. Technol.*, **5**, S395,.
163. A. M. Portis, 1993, In *Electrodynamics of High Temperature Superconductors*, *Lecture Notes in Physics*, Vol. 48, (World Scientific, Singapore).
164. C. P. Poole, Jr., *Electron Spin Resonance: A Comprehensive Treatise on Experimental Techniques* (Interscience, New York, 1967).
165. S. M. Quinlan, D. J. Scalapino and N. Bulut, 1994, *Phys. Rev. B*, **49**, 1470.
166. R. J. Radtke, V. N. Kostur and K. Levin, 1996, *Phys. Rev. B*, **53**, R522.
167. J. Rammer, 1991, *Europhys. Lett.*, **5**, 77.
168. Y. Ren, J. Xu and C. S. Ting, 1996, *Phys. Rev. B*, **53**, 2249.
169. E. Roddink and D. Stroud, 1995, *Phys. Rev. Lett.*, **74**, 1430.
170. M. B. Salamon, J. Shi, N. Overend and M. A. Howson, 1993, *Phys. Rev. B*, **47**, 5520.
171. G. Santi, T. Jarlborg, M. Peter and M. Weger, 1996, *Physica C*, **259**, 253.
172. D. J. Scalapino, 1995, *Phys. Rep.*, **250**, 329.
173. N. Schopohl and O. V. Dolgov, 1998, *Phys. Rev. Lett.*, **80**, 4761.
174. I. Schürrer, E. Schachinger and J.P. Carbotte, 1998, *Physica C*, **303**, 287.
175. D. V. Shovkun, M. R. Trunin, A. A. Zhukov, Yu. A. Nefyodov, H. Enriquez, N. Bontemps, A. Buzdin, M. Daumens and T. Tamegai, 2000, *Pis'ma Zh. Exp. Teor. Fiz.* **71**, 132 (2000, *JETP. Lett.*, **71**, 92).
176. E. Schachinger and J. P. Carbotte, 2000, *Phys. Rev. B*, **61**, 9088.
177. X. Z. Schen and D. S. Dessau, 1995, *Phys. Reports*, **253,** 1.
178. A. A. Shapoval, 1996, *Pis'ma Zh. Exp. Teor. Fiz.* **64**, 570.
179. T. Shibauchi, N. Katase, T. Tamegai and K. Uchinokura, 1996, *Physica C*, **264**, 227.
180. T. Shibauchi, H. Kitano, A. Maeda, H. Asaoka, H. Takei, I. Shigaki, T. Kimura, K. Kishio, K. Izumi, T. Suzuki and K. Uchinokura, 1996, *J. Phys. Soc. of Japan*, **65**, 3266.

181. T. Shibauchi, H. Kitano, K. Uchinokura, A. Maeda, T. Kimura and K. Kishio, 1994, *Phys. Rev. Lett.*, **72**, 2263.
182. T. Shibauchi, A. Maeda, H. Kitano, T. Honda and K. Uchinokura, 1992, *Physica C*, **203**, 315.
183. V. S. Simonov and V. N. Molchanov, 1996, *Kristallografia*, **41**, 31.
184. S. Sridhar and W. L. Kennedy, 1988, *Rev. Sci. Instrum.*, **54**, 531.
185. H. Srikanth, B. A. Willemsen, T. Jacobs, S. Sridhar, A. Erb, E. Walker and R. Flükiger, 1997, *Phys. Rev. B*, **55**, R14733.
186. H. Srikanth, Z. Zhai, S. Sridhar, A. Erb and E. Walker, 1998, *Phys. Rev. B*, **57**, 7986.
187. H. Srikanth, S. Sridhar, D. A. Gajewski and M. B. Maple, 1997, *Physica C*, **291**, 235.
188. H. Srikanth, Z. Zhai, S. Sridhar and A. Erb, 1998, *J. Phys. Chem. Solids*, **59**, 2105.
189. Y. Tanaka and S. Kashiwaya, 1996, *Phys. Rev. Lett.*, **74**, 3451; 1996, *Phys. Rev. B*, **53**, 11957.
190. M. R. Trunin, 1998, *J. Supercond.*, **11**, 381.
191. M. R. Trunin, 2000, *Pis'ma Zh. Exp. Teor. Fiz.*, **72**, 845 (2000, *JETP Lett.*, **72**, 845).
192. M. R. Trunin, A. A. Zhukov and A. T. Sokolov, 1997, *Zh. Exp. Teor. Fiz.*, **111**, 696 (1997, *JETP*, **84**, 383).
193. M. R. Trunin, A. A. Zhukov, G. A. Emel'chenko and I. G. Naumenko, 1997, *Pis'ma Zh. Exp. Teor. Fiz.* **65**, 893 (1997, *JETP Lett.*, **65**, 938).
194. M. R. Trunin, A. A. Zhukov, G. E. Tsydynzhapov, A. T. Sokolov, L. A. Klinkova and N. V. Barkovskii, 1996, *Pis'ma Zh. Exp. Teor. Fiz.*, **64**, 783 (1996, *JETP Lett.*, **64**, 832).
195. M. R. Trunin, A. A. Zhukov and A. T. Sokolov, 1998, *J. Phys. Chem. Solids*, **59**, 2125.
196. M. R. Trunin, 1998, *Uspekhi Fiz. Nauk*, **168**, 931 (1998, *Physics–Uspekhi*, **41**, 843).
197. M. R. Trunin, Yu. A. Nefyodov and H. J. Fink, 2000, *Zh. Exp. Teor. Fiz.*, **118**, 923 (2000, *JETP*, **91**, 801).
198. C. C. Tsuei, J. R. Kirtley, M. Rupp, J. Z. Sun, A. Gupta, M. B. Ketchen, C. A. Wang, Z. F. Ren, J. H. Wang and M. Bhushan, 1996, *Science*, **271**, 329.
199. J. P. Turneaure, J. Halbritter and H. A. Schwettman, 1991, *J. Supercond.*, **4**, 341.
200. C. M. Varma, P. B. Littlewood, S. Schmitt-Rink, E. Abrahams and A. E. Ruskenshtein, 1989, *Phys. Rev. Lett.*, **63**, 1996.
201. C. Varmazis, J. R. Hook, D. J. Sandiford and M. Strongin, 1975, *Phys. Rev. B*, **11**, 3354.
202. C. Varmazis, Y. Imry and M. Strongin, 1976, *Phys. Rev. B*, **13**, 2880.
203. L. A. de Vaulchier, J. P. Vieren, Y. Guldner, N. Bontemps, R. Combescot, Y. Lemaitre and J. C. Mage, 1996, *Europhys. Lett.*, **33**, 153.
204. A. V. Velichko and N. T. Cherpak, 1998, *Fizika Nizkikh Temperatur*, **24**, 395.
205. O. G. Vendik, A. B. Kozyrev and A. Yu. Popov, 1990, *Rev. Phys. Appl.*, **25**,

255.
206. O. G. Vendik, L. Kowalevicz, A. P. Mitrofanov, O. V. Pakhomov, A. Yu. Popov and T. B. Samoilova, 1990, *Sverkhprovodimost': Fiz., Khim., Tekh.*, **3**, 1573.
207. O. G. Vendik and A. Yu. Popov, 1992, *Phil. Mag. Lett.*, **65**, 219.
208. M. B. Walker and M. F. Smith, 2000, *Phys. Rev. B*, **61**, 11285.
209. J. R. Waldram, D. M. Broun, D. C. Morgan, R. Ormeno and A. Porch, 1999, *Phys. Rev. B*, **59**, 1528.
210. D. Walker and K. Schanberg, 1990, *Phys. Rev. B*, **42**, 2211.
211. X-G. Wen and P. A. Lee, 1998, *Phys. Rev. Lett.*, **80**, 2193.
212. H. Won and K. Maki, 1994, *Phys. Rev. B*, **49**, 1397.
213. T. Xiang and J. M. Wheatley, 1996, *Phys. Rev. Lett.*, **76**, 134; **77**, 4632.
214. H. You, J. D. Axe, X. B. Kan, S. Hashimoto, S. C. Moss, J. Z. Liu, G. W. Crabtree and D. J. Lam, 1988, *Phys. Rev. B*, **38**, 9213.
215. E. Zeldov, A. I. Larkin, V. B. Geshkenbein, M. Konczykowsky, D. Majer, B. Khaykovich, V. M. Vinokur and H. Shtrikman, 1994, *Phys. Rev. Lett.*, **73**, 1428.
216. K. Zhang, D. A. Bonn, R. Liang, D. J. Baar and W. N. Hardy, 1993, *Appl. Phys. Lett.*, **62**, 3019.
217. A. A. Zhukov, M. R. Trunin, A. T. Sokolov and N. N. Kolesnikov, 1997, *Zh. Exp. Teor. Fiz.*, **112**, 2210 (1997, JETP **85**, 1211).